Chen, Shuling (2013). Hydrodynamic behaviour of gliding hydrofoil crafts. (Unpublished Doctoral thesis, City University London)

Original citation: Chen, Shuling (2013). Hydrodynamic behaviour of gliding hydrofoil crafts. (Unpublished Doctoral thesis, City University London)

Permanent City Research Online URL: http://openaccess.city.ac.uk/2455/

HYDRODYNAMIC BEHAVIOUR OF GLIDING HYDROFOIL CRAFTS

By

Shuling Chen

MSc, B.Eng.

Supervisor

Prof. Qingwei Ma

A thesis submitted in fulfilment of

requirement of degree of

Doctor of Philosophy

School of Engineering and Mathematical Sciences

City University, London

January, 2013

CONTENTS

LIST OF FIGURES

LIST OF TABLES

ACKNOWLEDGEMENTS

This study is sponsored through the project ‘Hydrodynamic Behaviour of Gliding-Hydrofoil Crafts ‘funded by the UK Royal Society, for which the author is most grateful.

I would like to express my sincere gratitude to my supervisor Professor Q.W. Ma for the guidance, inspiration, assistance and supervision he has shown in helping to me complete this work. The patience and encouragement when various problems occurred are much appreciated. I would also like to thank him for his comments on the draft of this thesis.

I also thank Professor S.L.Yang, Jiangsu University of Science and Technology, PRC, for him to guide the ship model test.

During my study in City University, many of my friends and colleague in our research group provided their generous help to me. I would like to express my appreciation to Dr. S.Q. Yan, Dr. Juntao Zhou and Mr. S. Chidavaenzi. I would also offer my thanks to my colleagues in the school, for their suggestions and discussion on my work.

I also acknowledge the faculty and staff of the School of Naval Architecture and Ocean Engineering from Jiangsu University of Science and Technology for their support in the many years. Special thanks to Mr. Zhiyong Jiang, Mr. Yulong Zhou, Mr. Renqing Zhu and Mr. Zhidong Wang for their help and assistances.

Finally I also thank my husband, Ruifeng Li for his unconditional support and endless patience. And my cute daughter, Nanxue Li, which is the best gift I have ever had. I also give my deep appreciation to my parents. Without them, this work would not have been completed.

DECLARATION

No portion of the work referred to in the thesis has been submitted in support of an application for other degree or qualification of this or any other university or other institute of learning.

I grant powers of discretion to the City University Library to allow this thesis to be copied in whole or in part without any reference to me. This permission covers only single copies made for study purpose subject to normal condition of acknowledgement.

ABSTRACT

A new type of high-speed craft, called a Gliding-Hydrofoil Craft (GHC), has recently been developed in Jiangsu University of Science and Technology, China. This craft is similar to a planing hull but with a hydrofoil in the front part of its body. The fixed hydrofoil improves the seakeeping properties and stability of the craft compared with a conventional planing hull. In addition, the GHC has a more simple structure and higher stability when compared to a hydrofoil craft. Unlike conventional planing hulls and hydrofoil crafts, the study of hydrodynamics of GHC has been overlooked. The present work aims to advance our understanding on hydrodynamics of GHC, both model tests and numerical investigations are presented.

To study its hydrodynamic characteristics, model tests are carried out in a towing tank, and the total resistance, trim angle and wetted area of the craft in the cases with different Froude numbers are measured. For the purpose of comparison, model tests have also been carried out for the hull without the hydrofoil. This thesis presents analysis on the experimental data and discusses the effects of the submerged depth and initial attack angle of the hydrofoil on the hydrodynamic features of the GHC.

On this basis, the FLUENT software is then adopted to numerically investigate the hydrodynamics of the GHC. The accuracy of the FLUENT addressing this problem is validated by comparing the numerical solutions with the experimental data. The validation cases include 2D hydrofoil in current, Wigley hull with steady forward speed. Good agreement between numerical results and experimental data was obtained. Considering the significance of the turbulence involved in the problem, especially near the hydrofoil, a numerical investigation aiming to find a suitable turbulence model has been carried out. After being validated, 3D numerical simulations on both the planing craft and the GHC in steady flow are considered. The resistance coefficient, pressure coefficient and wave pattern with different Froude number are investigated. Some results are compared with experiment data obtained in the model tests. The wave pattern, velocity field and pressure distribution near the hulls are discussed in detail as well as the influence of the hydrofoil. Finally, the hydrodynamic performance of GHC in unsteady flow is investigated. Three cases were considered: ship berthing, leaving the harbour and turning navigation direction; which are very commonly seen unsteady examples in reality.

The preliminary results presented in this thesis have confirmed the significant effects due to the unsteady procedure and imply the need of carrying out unsteady simulations in the future.

LIST OF SYMBOLS

a_0	initial reading of aft sensor
a_t	steady reading of aft sensor
$A^{'}$	dimensionless coefficient
A_M	immersed area of midship section
A_{WP}	area of the waterplane
B	breadth
c	chord length
$\overline{c}$	relative thickness of hydrofoil
C_B	block coefficient
C_d	dimensionless resistance coefficient
C_f	frictional resistance coefficient
C_L	lift coefficient
C_{L0}	lift coefficient for zero deadrise angle (β=0°)
$C_{L\beta}$	lift coefficient
C_M	midship coefficient
C_P	prismatic coefficient
C_{WP}	waterplane coefficient
$C_{x\pi p}$	hydrofoil shape resistance coefficient
C_{xn}	induced resistance coefficient
C_{xB}	wave resistance coefficient
d_f	initial fore draft
d_a	initial aft draft,
d	draft
D	depth
D_a	load carried by hydrofoil
f	resistance of hydrofoil
f_{11}	hydrofoil shape resistance
f_{12}	induced resistance
f_{13}	wave resistance

f_{21}	friction resistance of planing hull
f_0	reading of the fore sensor in the initial condition
f_t	reading of the fore sensor in the steady status (referred to as steady reading)
F	resistance
F_c	chord length Froude number
F_i	external body forces
F_{L0}	lift force for zero deadrise angle (β=0°)
$F_{L\beta}$	hydrodynamic lift of planing surface
Fn_B	breadth Froude number
Fr	Froude number
Fr_s	wet length Froude number
g	acceleration of gravity
h	submergence depth
$\overline{h}$	relative immergence
k	
k_φ	dimensionless coefficient
l	distance between two sensors (the span length)
l_{cg}	longitudinal centre of gravity
l_p	longitudinal position of the center of pressure
L	overall submerged length of the ship
L_f	lift of the hydrofoil
L_C	chine wetted lengths
L_K	keel wetted lengths.
L_S	initial wetted length
L_w	wetted length of the ship
N	force due to nonviscous hydrodynamic pressures acting on the wetted hull
P	pressure
P_D	dynamic pressure
p_{ref}	reference pressure

P_S	static pressure
R	total resistance of the craft with a speed
R_{AA}	air resistance
R_{AP}	appendages resistance
Re	Reynolds number
Re_s	wet length Reynolds number
R_f	friction resistance
R_p	pressure resistance
R_t	naked hull resistance
R_X	hydrodynamic resistance
R_v	viscous resistance
S	wetted area of ship model with a certain forward speed
S_h	area of the hydrofoil
S_S	initial wetted area
S_w	wetted area of the hull
t	weight
T	propeller thrust, time
u	velocity
$\overline{u_i}$	mean velocity components
u_i'	fluctuating velocity components
U	ship speed
U_0	initial velocity
U_C	towing speed
V_s	design speed
λ	span-to-chord ratio
λ_W	mean wetted length-to-beam ratio
α	angle of attack
β	deadrise angle
τ	corrected value
τ_{ij}	stress tensor

ρ	density of water
$-\rho\overline{u_i^{'}u_j^{'}}$	Reynolds stress
θ	trim angle
$\theta_{\deg}$	trim angle of planing area in degrees
$\Gamma(x)$	wetted perimeter of the submerged cross-sectional area at each body plan station
ν	kinematic viscosity coefficient of water
μ	molecular viscosity
∇	volume of displacement
$\triangle$	weight of the craft
$\Delta\alpha_0$	change of attack angle of zero lift caused by free surface
ΔC_f	roughness coefficient
$\frac{\partial C_L}{\partial \alpha}$	derivative of the lift coefficient to angle of attack
Δl	size of cells

1. INTRODUCTION

1.1 Background

With the development of marine transport, greater number of high-speed craft are being designed and operated widely. There are many applications for high-speed craft, such as maritime transport and offshore industry, mainly because of the high speed and low cost of these types of vessels. Particularly in deeper seas where large-scale helicopter operations become expensive, high speed craft are more advantageous. In addition, the military's requirement for high-speed craft is also increasing. In many cases, military crafts need to run at high speed to fulfil their mission even in adverse sea conditions. Therefore, development of a high-speed craft for a seaway is in high demand for the naval architects of today. This is however a challenging task that requires further research and investigation of various high-speed vessels.

A high-speed vessel is a craft with a maximum operating speed higher than 30 knots (Baird, 1998), or with a Froude number ($Fr = U / \sqrt{Lg}$, where, U is the ship speed, L is the overall submerged length of the ship, and g is acceleration of gravity.) larger than about 0.4 for a fast vessel supported by the submerged hull, e.g. monohulls and catamarans. There are the other variety of high-speed vessels in use, such as hydrofoil-supported vessels (e.g. hydrofoil craft, as shown in Fig.1.1.a) and planing craft as shown in Fig.1.1.b. A discussion of the performance of planing craft and hydrofoil craft is given below.

(a) Hydrofoil craft in waves
www.hydrofoils.org/Star/star.html

(b) Planing craft in waves
http://www.defenseindustrydaily.com/

Fig.1.1 High-speed craft in waves

1.1.1 Planing Hull Craft

A planing hull craft is a high powered water-craft and is typically a submerged hull-supported vessel (Fig. 1.2).

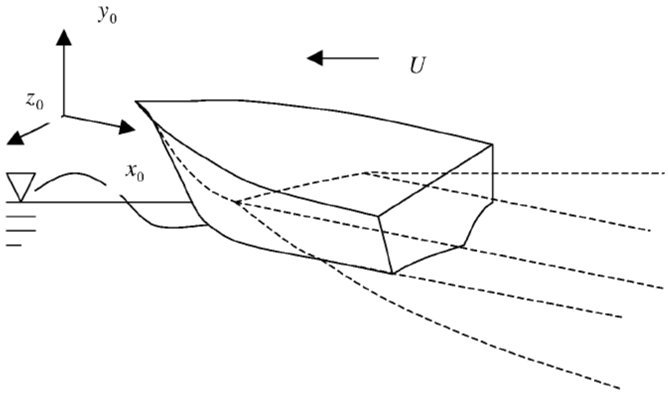

Fig.1.2 A planing monohull (Zhou, 2000)

The main differences between planing craft and traditional displacement type vessels can be summarised as follows:

(1) Lift force

For a planing craft, the wetted region at the back of the hull provides the necessary dynamic lift to support the vessel, while for a displacement type of vessel it is supported primarily by hydrostatic pressure.

(2) Navigation states

In order to develop the necessary dynamic lift, the craft must be operated at high speed. Therefore, the geometric shape of the wetted region of the planing craft must be properly configured, i.e. it must have a declining deadrise angle from bow to stern. In addition, the shape and attack angle affect the pressure distribution and hence the lift force. However, this attack angle is gradually produced as the speed increases; before the craft reaches the cruise speed, it works in a similar way to a conventional displacement-type vessel. The change in the planing craft's draft, attack angle and wetted length are directly related to the craft's forward velocity. The relationship between them is highly nonlinear.

(3) Flow near the craft

As the planing craft speed increases the hydrodynamic pressure on the bottom of the hull increases, forming a high-speed jet of water. Associated with this is a loss of energy, and hence an increase in resistance. The jet processes are in particular associated with planing crafts.

1.1.2 Hydrofoil Craft

Hydrofoil craft are hydrofoil-supported vessels with either fully submerged or free surface-piercing foils. The hydrofoils provide lift forces to support the weight of the craft. Hydrofoil craft with fully submerged foil systems (Fig. 1.3) provide the best comfort ride at high-speeds. The foils of the fully-submerged concept are designed to operate at all times under the water surface. The struts which connect the foils to the hull generally do not contribute to the total lifting force. The unique operational feature of hydrofoils is to minimize the coupling effects between ships and waves, and so reducing the dag. In the surface piercing concept, the struts are designed to extend through the air/sea interface which may provide some force to stabilize the craft.

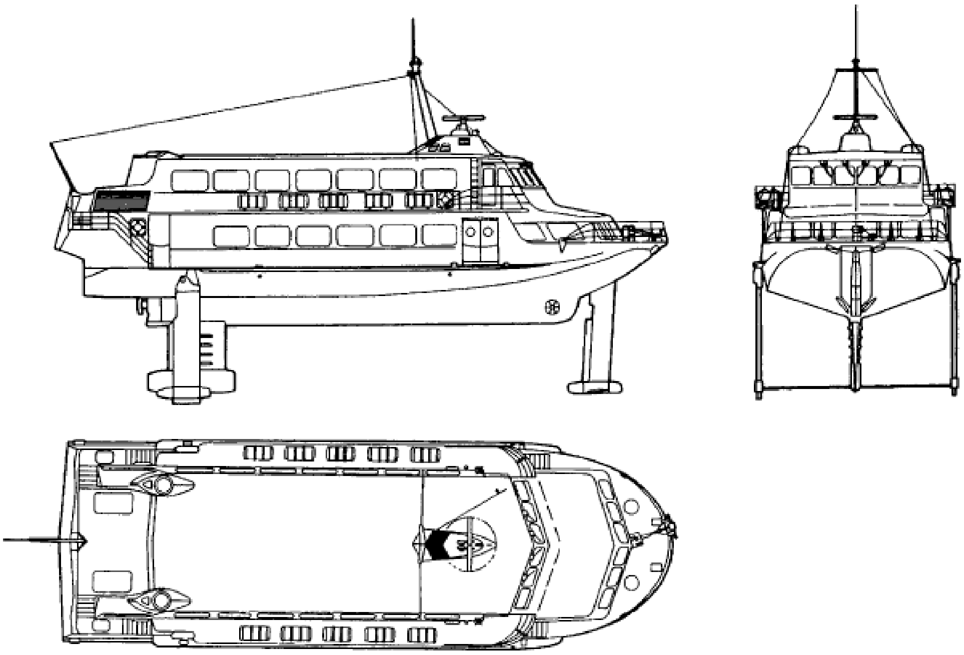

Fig.1.3 Fully submerged hydrofoil craft (Kim, 2004b)

The lifting force generated by the water flow over the submerged portion of the foils increases with the speed, causing the ship to rise and the submerged area of the foils to decrease. For a given speed the ship will rise up to the lifting force equals the weight of the ship.

Compared to a displacement-type vessel, a hydrofoil craft is also a high powered water-craft that develops the necessary lifting forces which support its weight primarily through hydrodynamic water pressure on hydrofoils. This is different from a planing craft, for which the dynamic lift is generated by a wetted region of the hull. The hydrofoil vessels have good seakeeping characteristics; small swash created and less speed loss due to incident waves.

For hydrofoil crafts, hydrofoils play an important role in the design and operation of the craft. Johnston (1985) pointed out the important aspects that should be considered when selecting foil and strut configuration for fully submerged hydrofoils as follow:

- Maintenance of directional and roll stability;
- Stable recovery when a foil comes out of the water (broaches);
- Graceful deterioration of performance in severe seas;
- Safety.

To summarize, the typical characteristics of planing craft and hydrofoil craft can be characterized as “small volume, small displacement and high speed”. However, each of them has its own disadvantages, which will be discussed in the following section.

1.1.3 Gliding-hydrofoil Craft

For a planing vessel, a large part of the hull is lifted out of the water at the cruise speed. This reduces the resistance compared with conventional displacement vessels. Vessels with this sort of hull travel smoothly in calm water. But in waves, these ships suffer from pounding or slamming. Thus, the disadvantages of a planing craft are its poor seakeeping properties and potentially significant speed loss due to serious pounding or slamming in waves. Hydrofoil vessels have also some disadvantages, such as a complicated structure and poor maneuverability because the whole hull is lifted out of the water. Consequently it is difficult to design and build hydrofoil craft with larger displacement.

In order to combine the advantages of planing and hydrofoil vessels and overcome their disadvantages, the GHC (Gliding-Hydrofoil Craft) was recently proposed in Jiangsu University of Science and Technology (Yang S.L., 2006). The structure of a GHC is shown in Fig.1.4.

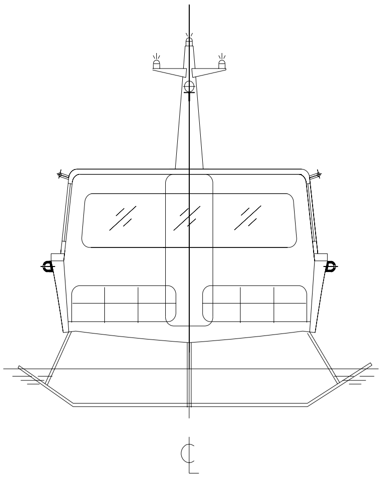

(a) Front view of the GHC

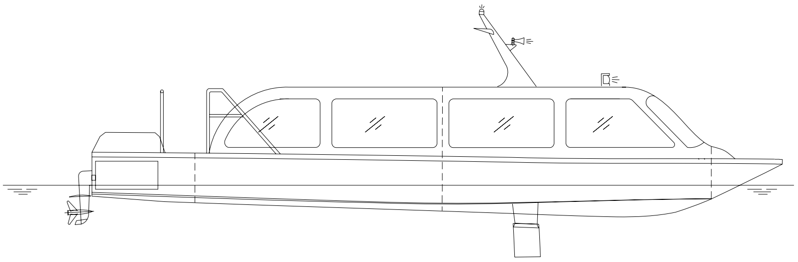

(b) Side view of the GHC

Fig.1.4 The structure of GHC

This craft differents from the planing craft as a hydrofoil is mounted on the front part of the hull, which provids lift forces and reducs the possibility of pounding or slamming. Compared with hydrofoil craft, it has only one hydrofoil. In addition, it has only on hydrofoil and because the stern part of the craft is still in the water at cruise speed, the maneuverability is better than a hydrofoil craft. Consequently, the GHC has better seakeeping properties and maneuverability and a simpler structure.

This craft is a new craft. Its hydrodynamics are different from a planing hull and a hydrofoil craft and has not been well studied.

1.2 The purpose and significance of the study

The aim of this project is to study the hydrodynamic behaviour of the gliding-hydrofoil craft using numerical analysis and physical model tests. The main tasks are summarised as follows:

1. To simulate the viscous flow field around the gliding-hydrofoil craft for different navigation states and different Froude numbers using the CFD software FLUENT in steady and unsteady cases.
2. To carry out experiments on the some ship models to measure some hydrodynamic coefficients.
3. To compare the results calculated by FLUENT with the results measured in the experiment.
4. To develop empirical formula for hydrodynamic coefficients for this type of craft.

1.3 The main contributions of the study

A GHC is a newly developed fast-speed vessel. It is similar to a planning hull but with a hydrofoil installed in the front part of the body, which overcomes some drawbacks associated with planning hulls and hydrofoil hulls, and therefore, has better seakeeping properties, stability and simpler structures. I anticipated the design of the GHC. The main contributions of this work are the experimental and numerical investigations carried out to investigate the hydrodynamic behaviour of the GHC, which is the first in the world.

The experiments were carried out in the towing tank at the JUST. For the purpose of comparison, both a planning hull model and a GHC model were used. I designed the whole experimental process was designed to measure the resistance coefficients and trim angles and to observe the wave pattern. The main contributions include:

1. Studying the pattern of the resistance against different Froude number representing various navigating speed. It confirms that the resistance coefficient of GHC reaches minimum at its design speed;
2. Identifying the roles of viscous drag and wave resistance; exploring the effects of the initial attack angle and submerged depth of the hydrofoil in the significance of the wave resistance and the overall performance of the GHC;
3. Evaluating the superiority of the GHC over the planning hull in terms of overall performance.

The outcomes from the present work will help the design and the optimization of the GHC.

The main purpose of the numerical work is to look at the pressure distributions around the hull and the hydrofoil and the wave pattern around the hull in order to extend our understanding of the hydrodynamics related to the GHC. FLUENT software was used for this purpose. The main contributions include:

1. Designing a framework enabling the FLUENT to run a GHC in waves, including the mesh size/structure, turbulence model and free surface treatment.
2. Evaluating the pressure, velocity distribution near the hull, the wave pattern. Based on this, a semi-empirical procedure to evaluating hydrodynamic coefficients was developed. This has been proved to be able to give reasonable evaluation of resistance for a GHC.
3. Studying the unsteady behaviour and identify directions for future investigation.

2. LITERATURE REVIEW AND DISCUSSION OF PREVIOUS WORK

Many types of high-speed crafts have been designed and operated. This chapter reviews previous studies associated with hydrodynamic characteristics of high-speed crafts in the fields of model tests and numerical computation. Only the reviews on the planing craft and the hydrofoil craft, which are closely related to the Gliding-Hydrofoil Craft (GHC), a new type high-speed craft proposed in this thesis, will be presented here. The GHC is partially similar to a planing craft but with a hydrofoil installed in the front part of the ship as indicated in Chapter 1. Both model tests and computational methods will be used to study its hydrodynamic characteristics.

2.1 Planing craft

A planing craft is a high powered water-craft that develops the necessary lifting forces that support its weight primarily through hydrodynamic pressure. The hydrodynamic lift of a planning craft is different from that of a conventional displacement vessel, which is supported primarily by the hydrostatic pressure. The planing craft has specially-designed bottom form, which produces hydrodynamic forces in vertical direction to lift the vessel during cruise at a high speed and, therefore, the resistance on the planing craft is relatively smaller compared with conventional displacement ships.

Theoretical research on steady planing craft dates back to the early of 1930’s; following the pioneering works of Th. Von Karman’s (1929) on impact analysis of seaplane landing, and Wagner’s (1932) on flat-plate model for the investigation of water-entry problems. Despite these early developments, solving hydrodynamics problems of planing crafts using theoretical and numerical methods remains a challenging task. For example, the significant nonlinearity in physical flow makes it difficult to model the hydrodynamic processes; the high-speed jet, or water spray, generated in planing is relevant but is difficult to be addressed; and the location of the jet-head in the chine-unwetted flow is not known in advance. Therefore, in the majority of research efforts in the past, planing problems have been approximately solved by applying the basic assumptions which ignore gravity, viscosity and compressibility. Examples of these approaches based on 2-D impact solution and slender body theory include Cointe (1987,1991), Zhao & Faltinsen (1993, 1996), Vorus (1996), Kim, Vorus, and Troesch (1996), Zhao et al

(1997), Savander (1997), Royce and Vorus (1998), Xu, Troesch, and Vorus (1998), Breslin (2000), Vorus & Royce (2000), Judge (2001), and Royce (2001). Lai& Troesch (1995, 1996), performed a 3-D lifting surface solution for planning which relied on 2-D/SBT predictions (Vorus ,1996) for the position of the jet-head boundary.

Savitsky (1964) presented a semi-empirical method for the hydrodynamic design of planing monohulls. Savitsky's method allows designers to estimate the hull resistance and the trim angle using two equations of equilibrium with coefficients regressed from empirical data obtained in towing tank tests of prismatic planing hulls. This method was very popular in planing boat designing over the years to provide the foundation for the majority of the preliminary resistance predictions of planing mono-hulls. However, it is derived based on the experiments using certain geometry of the hulls and thus not sufficiently sensitive to the geometric details. It may not be suitable for evaluating planing monohulls with modern configurations.

The 2.5D method is also called 2D+T theory, which is a kind of slender body theory to calculate planing craft motions. 2.5D method simplifies a 3-D hull into a series of 2-D sections. The overall force acting on the craft and is obtained by integrating the force on each section in the longitudinal direction of the hull. Hajime Kihara (2006) developed a method for the nonlinear free surface flow including a splash caused by a high-speed vessel, in which the 2.5D method is employed for the computation of the wave field of around the planing hull. Ma (2005) applied 2.5D potential theory to calculate the hydrodynamic coefficients of the motion and the wave-induced loads acting on the planing craft. Lewis *et al.* (2006) used both a RANSE method and the 2-D strip theory to predict high-speed craft motion. Battistin *et al.* (2003) investigated the hydrodynamic properties of prismatic planing hulls using the 2D+T approach. Hui Sun et al. (1997) applied the 2D+T theory to solve for steady planing at a very high forward speed without considering the gravity effect. Zhao et al. (2007) followed and improved the approach to consider gravity effects in the steady planing of a prismatic hull. The comparison between craft at high planing speed and that at moderate planing speed has shown that the gravity not only affects the free-surface profile around the hull, but also influences the hydrodynamic force on the hull surface. Hui Sun *et al.* (2010) used 2D+T theory to perform nonlinear time domain simulations of a prismatic planing boat in incident waves. The added mass and damping coefficients were determined. The wave induced heave and pitch motions calculated in his paper are compared with experiments. Hui Sun *et al*. (2011) studied the dynamic response of planing vessels in regular head seas. Nonlinear time domain simulations were performed using a 2D+T theory and a 2D boundary element method to solve the initial boundary value problems in 2D cross planes, in which nonlinear free-surface conditions and exact body boundary conditions were satisfied. More details about the evolution and application of nonlinear 2D+T theory in the 1990's can be found in Fontaine and Tulin (1998).

Recently, with the development of computers, 3-D CFD methods became widely used to investigate the hydrodynamic properties of planing crafts. The advantage of CFD lies in the possibility of analyzing and comparing "real" hull shapes. In 3-D CFD method, the Navier-Stokes equation is solved for the flow in a fluid domain. Cao (2008) and Wang et al. (2009) predicted the resistances of a planing vessel which were confirmed by experiments or the experience formula. This work, amongst others, has confirmed that CFD commerical software is suitable for evaluating the hydrodynamic performances of the planing crafts considering the large deformation of free surface flow. The steady flow computations efficiently creates a completed resistance curve in one time covering entire range of Froude number (*Fn*), from zero to maximum speed. The dynamic sinkage and trim may also be computed along with the resistance for the entire Fn range. Azcueta et al. (2003) numerically simulated the motions of planing boats in waves using three different methods, one method by Soding based on an extension of Wagner's theory, and the other two (one by Caponnetto, the other by Azcueta) based on the RANSE solver Comet. Caponnetto et al. (2001) used CFD commercial software to compute the large deformations of the free surface by fast boats. The agreement between the CFD results and the Savitsky method is acceptable. Qiu et al. (2008) used 2-D and 3-D methods to compute the slamming force on a planing hull which were computed using the strip theory, where the impact force on each 2-D section is calculated by using 2-D constrained interpolation profile (CIP) method and 3-D CIP method. Su et al. (2012) presented a new CFD method to calculate the hydrodynamic forces acting on planing vessels. In this method, the RANSE equation for fluid domain is solved and the forces/moments acting on the planing vessel can be obtained. Through solving six-degrees-of-freedom equation of motion using the force/moments obtained, the velocities and displacements (translations and rotations) of the vessels were obtained. The position of the vessel and the fluid domain were therefore updated. By repeating this procedure over time, the trajectory of the vessel can be obtained. This new method does not need to pre-determine the running attitude of the planing vessels which is essential in the traditional CFD approaches, model tests or empirical formulas.

In addition to the 2D slender body theory, 2D+T theory and 3D CFD method, there are some other methods to investigate the hydrodynamic characteristics of planing craft. Some examples are given in Ahamad (2010), Hassan (2008a, 2008b), Hassan (2009), Shen (2011) and Akkerman (2012).

On the experimental side, many studies can be found. Clement and Blount (1963) conducted an extensive model tests on a systematic series (Series 62). Savitsky (1964) developed regression formulas for estimating the hydrodynamic forces acting on planing craft. Payne P. R. (1994) studied the water rise in front of a model planing hull and a number of attempts have been made for the experimental measurements of this phenomenon. The ship motion of planing craft at super high-speed at Fr=2.0 to 5.0 in regular head waves were measured in a towing tank by Katayama T. et al. (2000), including linear motion, non-linear motion with and without jumping. Savitsky et al. (2007) investigated the characteristics of the wetted bottom area and the spray area.

The disadvantage of planing craft, however, lies in its poor seakeeping properties and potentially significant speed losses due to serious pounding or slamming in waves (Zhou, Z. Q., 2003).

2.2 Hydrofoil craft

This section presents a brief review of the development of experimental and numerical studies for the analysis of hydrofoil craft. Considering the fact that the hydrofoil flow builds the basis of the hydrodynamic properties of hydrofoil craft, the reviews on the studies of hydrofoil flow are also given before that for the hydrofoil craft.

2.2.1 2-D hydrofoil flows

In early studies of the flow around the hydrofoil, thin-foil approximation and Neumann type boundary condition were generally used. Hough and Moran (1969) and Plotkin (1975) used the thin-foil approximation with linearised free surface condition. The former examined the flow around flat-plate and cambered-arc hydrofoils while the latter included a thickness correction around the leading edge. Giesing and Smith (1967) and Yeung and Bouger (1979) dealt with thick-foils which provided a better representation of the flow near the hydrofoil surface. Giesing and Smith (1967) distributed the Kelvin wave source solution on the hydrofoil surface, satisfying the linearised free surface condition and obtained an integral equation for the source strength by applying the kinematic body boundary condition (Neumann condition). This integral equation was numerically solved. Yeung and Bouger (1979) used a hybrid integral equation method based on Green's theorem. Their solution satisfied linearised free surface condition and exact body condition.

In addition, Salvasen (1969); Kennell and Plotkin (1984); Forbes (1985); Bai and Han (1994) computed nonlinear free surface effects. Salvasen (1969) derived a consistent second-order perturbation theory for the same purpose. Kennell and Plotkin (1984) also computed the second-order effects of the free surface for thin-hydrofoils. They provided consistent approximation to the flow properties both at the hydrofoil surface and on the free surface. In Forbes (1985), fully nonlinear free surface condition was satisfied. Wu and Eatock Taylor (1995) compared the finite element method with the boundary element method for the nonlinear time stepping solution of 2-D hydrofoils.

Sakir Bal (1999) applied a constant potential based panel method (Dirichlet type boundary condition). Kerwin et al. (1987) considered 2-D hydrofoils moving with constant speed beneath the free surface. More recently, Kouh et al. (2002) analysed the performance of a 2D hydrofoil under free surface. They distribute sources on undisturbed free surface and doublets on the foil and wake surface. Dirichlet-type body boundary condition is used instead of Neumann-type boundary condition, the free surface condition is linearised by free stream potential.

Chung (2008) numerically studied the hydrodynamic performance of a 2-D flat-plate hydrofoil in rowing motion. Many design parameters including the reduced frequency of the rowing motion, the heave amplitude, the time lags of the feathered-to-broadside rotation and the broadside-to-feathered rotation, were studied. The steady and unsteady cavitations phenomena on a 2D NACA0015 hydrofoil predicted by the multiphase RANS code FLUENT were studied by Li (2010), which focused on two cavitations numbers, i.e. σ=1.6 (steady cavitating flow) and σ=1.0 (with dynamic shedding), together with a numerical sensitivity study of non-cavitating condition. Karim (2012) presented a numerical study of periodic cavitating flow around a

NACA0012 hydrofoil. In this study, the cavitations condition were modelled through a bubble dynamics cavitations model and the RNG k–e turbulence model with enhanced wall treatment was employed to capture the turbulent boundary layer along the hydrofoil surface. In addition, Karim (2012) also simulated the periodic formation of vortex near the trailing edge, jet of re-entrant flow and the pressure fluctuation on the foil surface due to the periodic nature of the vorticity dynamics. It was found that the lift and resistance coefficients oscillate with a time average value of C_L=0.697 and C_D=0.012 with the periodic cavity shedding. Chen (2012) developed a new vortex based panel method for the numerical simulation of 2-D potential flow around a submerged hydrofoil submerged with energy dissipation. In this method, dissipative Green functions are employed with the resulting solution determined from a vortex distribution on the hydrofoil. The author concluded that the energy dissipation over the free surface cancels the singularities of the frequency domain integration of the Green functions.

2.2.2 3-D hydrofoil flows

The flow around 3-D cavitating hydrofoils was first addressed in the strip theory by Nishiyama (1970), Furuya (1975), Uhlman (1978), Van Houten (1982). Analytical solutions were obtained by matching the inner solution with the solution from lifting line theory in the outer domain. However, this method is only applicable for hydrofoils with high aspect ratios.

Velocity-based and potential-based boundary element methods (BEMs) were also extended to treat 3D hydrofoils. Kinnas and Fine (1993) developed a potential based BEM to predict patterns on 3D hydrofoils with good convergence properties. Similar techniques were also developed by Lee et al. (1992) for steady inflows and by Kim et al. (1994) for unsteady inflows.

In the analysis of 3D lifting bodies with free surface, Lee and Joo (1996) used a method considering mixed source and doublet distribution on body surface and source distribution on free surface to calculate wave-making resistance of catamaran. Dirichlet body boundary conditions were imposed on the body surface. In their formulations, the source strength on body surface was set as the normal component of incoming flow velocity, but the induced velocity of source distribution on free surface was not included. Therefore, the body boundary conditions were not exactly satisfied. The authors strongly recommended checking normal velocity component on body surface.

Larsson and Janson (1999) developed a 3D potential flow based panel method for yacht simulations. In this method, sources and doublets are distributed on the lifting part of the yacht. The use of Neumann boundary condition (normal velocity equals to zero) leads to less equations than the unknown strengths of sources and doublets. In order to make the problem be closure, the lifting body surface is divided into strips, essentially, parallel with the undisturbed flow direction. At each strip, the doublet strength is assumed to be constant span-wise and vary linearly with the arc length from the trailing edge of the pressure side around the nose to the trailing edge on the suction side. Behind the trailing edge, several wake panels are added along which the doublet strength is constant. Kutta condition is satisfied by prescribing a direction of the flow immediately behind the trailing edge, where the velocity vector is assumed to be in the bisector plane. Numerically, this is accomplished by specifying the velocity component normal to the surface to be zero. This turns out to be exactly the same condition as the hull surface condition, and thus Kutta equations are of exactly the same form as the hull condition. By this way, the problem becomes closure. Considering the possible problem arising by calculating the induced velocity of the doublet on the lifting body surface and Kutta panels, some researchers distributed the doublet on the central plane of the lifting body, (e.g., Nakatake et al., 1990; Zou and Soding, 1994); while some distribute the doublet on a sub-surface inside the body (de-singularity method, e.g. Chen and Liu, 2005).

Xie (2007) developed another potential-based panel method for determining the steady potential flow around 3D submerged hydrofoil, considering free surface effects. The method uses constant-strength doublets and source density distribution over the foil body surface and imposes Dirichlet-type boundary conditions instead of Neumann-type conditions. The undisturbed free surface source density is used to satisfy the free surface condition. The source density is linearised in terms of double-body approach and is discretised by a one-side, upstream, four-point finite difference operator. After solving the doublets on the foil and sources on the free surface, the numerical results of pressure, lift and resistance coefficients as well as wave profiles can be obtained for different Froude numbers and submerged depth to demonstrate the influence of the free surface and the aspect ratio effects on the performance of the hydrofoil.

The cavitation on 3D hydrofoil is also studied by Liu (2010) and Li (2010).Yang (2012) developed a hydrofoil for helical vertical axis turbine to duplicate marine current energy. The hydrofoil was optimized by means of traditional genetic algorithms combined with hierarchical fair competition model. In this study, Bezier curve was used to parameterize the hydrofoils and numerical analysis was also carried out to evaluate hydrodynamic performance.

2.2.3 Hydrofoil craft

The hydrofoil craft is a hydrofoil vessels that has two hydrofoils installed in fore and aft parts. The foils can lift the main hull outside water and so the vessels have a very small wetted area during cruise at a high speed. Their performance in terms of speeds is better than the planing craft. However, a sophisticated control system may be required to stabilize the motion of the hydrofoil craft and to improve their manoeuvrability (Brown, 1984; Imamura, 1990; Weist, 1976). The current control system of a fully-submerged hydrofoil craft based on optimal feedback control has, however, several problems, for example, poor performance of contouring waves and limitation in reducing the effect of wave disturbance. Kim (2004b) applied the optimal preview servo system, composed of feedback controller and feed forward controller to the longitudinal control system of a fully-submerged hydrofoil craft in order to tackle the challenge of conventional control system. The validity of the proposed control system in his paper, based on pre-determined weighting functions in performance index, reference input and wave disturbance, is confirmed by numerical simulations. Kim (2005) pointed out that the current control system of a fully submerged hydrofoil craft improves its performance through manual input of the fore-foil submerged depth and the control mode. However, the manual input requires skilful human operations and observations of waves encountered in the control system to ensure a good performance under a wide range of wave conditions. Although the later may be achieved considering the estimation of wave elevation and disturbance caused by the orbital motion of the waves in random sea, as confirmed by Kim (2005). In addition, it has also been reported that a cresting and foil exposing may occur in following seas (e.g., Kim (2004a); Saito (1990) and Saito (1989)).

The studies listed above focused mainly on numerical work related to hydrofoil crafts. The corresponding experimental investigations or model tests have also been subject of various studies. From the numerous publication, only a few examples are mentioned here. As for the hydrofoil craft, Henry et al. (1959), Besch and Liu (1972) and Abramson (1974) studied the flutter of hydrofoil vessels. Inukai et al. (2001) tested a sailing catamaran with submerged foils. Kim et al. (2004a) carried out experiments to study the longitudinal motion of a fully submerged hydrofoil craft in following sea. More details about research on the hydrodynamics of the planing and hydrofoil craft may be found in Faltinsen (2005).

2.3 Gliding-hydrofoil craft

In order to take the advantages of these two types of craft and minimize their disadvantages, the gliding-hydrofoil craft (GHC) was proposed by Yang and Gao (2006).

Due to its distinctive structure, the hydrodynamic characteristics of the GHC are different from either the planing craft or hydrofoil craft and needs to be extensively studied. For this purpose, Yang and Gao (2006) carried out experiments on a 1.58 m GHC ship model in a river and measured the ratio of resistance to the weight of the craft at different speeds and gave a curve relating effective power to its speeds. Yang and Chen (2008) investigated the interaction between the navigation speed of the craft and the rotational speed of its main engine, again based on the model test in a river. Yang et al. (2008) started to experimentally study the hydrodynamics of the GHC, but only gave some preliminary analysis for some cases at several speeds. Chen et al. (2008) also carried out some experimental studies on the hydrodynamics of the GHC, but a very simple rectangular hydrofoil section was used. Chen et al. (2011) further considered the hydrodynamic characteristics of the GHC based on the model tests in a towing tank carried out recently. The resistance, trim angle and wetted area at different forward speeds will be analyzed and discussed in a more robust way.

2.4 EFD (Experimental Fluid Dynamic) on the high-speed craft

In order to validate an existing theory or to develop empirical formula, researchers have often used experimental methods to better understand the physics. In fact, much of the hydrodynamic understanding of ships has been obtained through model tests. Experimental Fluid Dynamics (EFD) plays an essential role in the ship hydrodynamics. It started by being used to measure only macroscopic forces, but has gradually been extended to detailed measurement of distributed quantities. This tendency has been enhanced by developments in CFD, which needs detailed data for validation, and EFD and CFD are becoming more closely linked for better hull form design.

This section reviews recent research aiming a better physical understanding of hydrodynamics and applying new techniques in the area of experimental fluid dynamics (EFD). The trends in EFD related to the field of naval architecture is summarized into five parts: 1) new development in measurement techniques, 2) development in experimental facilities, 3) full scale tests, 4) drag reduction, and 5) uncertainties in EFD.

2.4.1 New development in measurement techniques

There has been a remarkable progress in measurement techniques for experiments in towing tanks, water tunnels, wind tunnels and wave tanks. The progress has been possible by adopting newly developed hardware, software and ever-increasing computer power. Especially, the improvements of optical techniques are notable. The optical techniques involve Particle Image Velocimetry (PIV), Particle Tracking Velocimetry (PTV), Laser Doppler Velocimetry (LDV), Laser Induced Fluorescence (LIF) and so on. The advanced techniques for hydrodynamic experiments are introduced here together with a summary of recent research using these techniques.

PIV is an optical technique used to measure velocities and related properties in fluids. The fluid is seeded with particles which are generally assumed to faithfully follow the flow dynamics. The velocity field having 2 or 3 components is computed from the correlation between successive particle images using statistical methods.

The PIV technique is one of the most popular optical techniques to measure the velocity field. The practical application of this technique has however been limited in the naval hydrodynamic area because it requires a relatively large space for CCD cameras, illuminating laser, computers and other gear. Recently, the PIV technique has been utilized to obtain the velocity field near a model ship in towing tank overcoming this space limitation. Atsavapranee et al. (2004) measured the pressure, force and moments acting on a 5.27m submarine model, ONR Body-1 (bare hull, bare hull with sail and fully appended) and obtained the flow field including the vertical flow and flow separation near the model using PIV. Chen and Chang (2006) developed a flow velocity measurement system to observe velocity fields near ship models using a moving PIV system. These researchers discussed technical issues related to the application of PIV in towing tanks and suggested possible solutions for the problems caused in the moving PIV system. To remove the reflection of the laser light from cavitation, Foeth et al. (2006) utilized PIV measurement to investigate the cavitation developed on a hydrofoil surface with fluorescent tracer particles. Ryu et al. (2005) modified a PIV technique to obtain the flow field of the highly aerated area generated by wave breaking and greenwater; mainly due to the highly aerated bubbly flow caused traditional PIV techniques to fail due to the uncontrollable scattering of the laser light. This modified PIV method, called bubble image velocimetry (BIV), was introduced by directly using bubbles as the tracer and measuring the bubble velocity by correlating the "texture" of the bubble images.

PTV is another optical technique used to measure the fluid velocity including 2 or 3 components. While the PIV measurement computes one velocity vector from several particles in the interrogation area, PTV determines the velocity of each individual particle within the optical image. Hoyer et al. (2005) presented an experimental setup and data processing schemes for 3-D scanning PTV, which expands on the classical 3-D PTV through changes in the laser illumination and image acquisition and analysis. This technique allows for obtaining Lagrangian flow information directly from measured 3-D trajectories of individual particles. Lee et al. (2005) applied the adaptive hybrid two-frame PTV technique to measure the flow characteristics of a turbulent wake behind a marine propeller with five blades and compared the results to those obtained with PIV. This technique can be extended to investigate the nominal and effective wake distribution as well as the details of the flow field fore and aft of a rotating propeller behind a ship model.

The HTA JRP-1 research activities on "PIV operation in hydrodynamic facilities" conducted by a large group is reported by Fréchou et al. (2009) covering wave run-up, wake flows in powering/manoeuvring conditions, wake flows in cavitation tunnel or shallow water basin, nuclei sizing in cavitation tunnel, and a flat plate benchmarking program.

Measuring the turbulent kinetic energy dissipation rate in an enclosed turbulence chamber that produces zero-mean flow is an experimental challenge (de Jong et al., 2009). The capability of Interfacial PIV was validated against Particle Image Distortion using synthetic image pairs generated from a DNS velocity field over a sinusoidal bed (Nguyen et al., 2010). Wake measurement data provide physical insight into the factors to be considered for the propeller operation of VLCC in damaged conditions (Yang et al., 2009). Flow characteristics of the hull wake behind a container ship model were investigated under different loading conditions by PIV (Lee et al., 2009)

The LIF technique is a spectroscopic method used for studying structure of molecules, detection of selective species and flow visualizations and measurements. The species in the fluid to be examined is excited with the help of a laser. The wavelength selected for the species and the fluorescence light is obtained by a camera with an optical bandwidth filter. This optical technique is often used to investigate the concentration and molecular behaviour in a fluid in combination with PIV or PTV. Troy and Koseff (2005) presented the application of LIF for the generation and quantitative visualization of breaking progressive internal waves. LIF techniques can help in understanding the nature of turbulent and multi-phase flows due to wave breaking or cavitation phenomena.

The LDA technique utilizes laser beams to intersect at a focal point, where they interfere and generate a set of straight fringes. The optical sensor is then aligned with the flow direction. As particles pass through the fringes, they reflect light with a Doppler shift corresponding to the velocity of particles at the region of constructive interference into a photo detector. The ADV technique employs a similar principle as LDV, but uses an acoustic wave instead of an acoustic wave at a fixed frequency from a transmitter probe. These waves reflect off moving particulate matter in the water and three receiving probes obtain the change in frequency of the returned waves. These Doppler techniques are limited to measuring the fluid velocity at a point, but they can be employed to measure the fluid near a wall and in full scale model tests with relatively high time resolution and the convenience of no need for calibration. Cea et al. (2007) used ADV to measure the 3-D instantaneous velocity of a highly turbulent free surface flow and applied several filters including the minimum/maximum threshold, the acceleration threshold and the phase-space threshold in order to eliminate any corrupted velocity data. Millward and Brown (2005) proposed a new method of measuring the actual wetted surface area of a model ship tested in a towing tank, which is based on capacitance where the model hull has been given a metallic coating and then an insulating coating so that it effectively becomes one place of a capacitor with the water of a towing tank or a water channel becoming the other plate. Song et al. (2007) conducted the resistance test of an ice breaker “Terry Fox” in a towing tank with synthetic ice whose data are compared with those conducted in the ice tank at IOT (Institute of Ocean Technology) Canada, showing a good correlation between the two data sets.

A number of advanced techniques to measure the three-dimensional wave field generated by a moving ship are used: a scanning Light Detection and Ranging, (LiDAR) system, a laser sheet-optical quantitative visualization (QViz) system, a Nortek Acoustic Wave and Current (AWAC) profiler, ultrasonic range finders, finger probes, and capacitance wires. Fu and Fullerton (2009) and Drazen et al. (2010) describes recent efforts and compares results from the LiDAR, QViz, AWAC, and ultrasonic range finder systems for the measurement of waves generated by the tow tank wave makers and by a large generic transom stern model. A new generation of acoustic wave probes is developed to function well at high towing carriage speeds and high wave encounter frequencies with the support of the HTA project (Bouvy et al., 2009). Cobelli et al. (2009) introduced an optical profilometric technique that allows for single-shot global measurement of free-surface deformations.

The direct measurement of wave resistance from the measurement of ship-wave height on a patch of surface water near the hull with optical instrumentation was done by Çalişal et al. (2009).

Image measurement techniques have gained more attention as Sanada and Nagaya (2010a) summarized the recent status: e.g., Takayama et al. (2008), Sanada et al. (2010b), and Tanimoto et al. (2010) for ship wave measurements by using the RLD method; and Nagaya et al. (2010) for flow field measurements by using stereo PIV.

2.4.2 Full scale tests

Sur and Chevalier (2004) performed full scale measurements of bow spray droplets created by the breaking bow wave for R/V Roger Revelle at speeds ranging from 1.0 to 7.7 m/s and sea states of 0 to 3 using a high speed digital video camera. Starke et al. (2006) measured the full scale wake field using a ship-mounted LDV system during sea trials to validate computation results. Fu et al. (2006) carried out a sea trial test of the R/V Athena Ⅰ to characterize: 1) the free surface in the bow region and behind the transom, 2) the spray in the bow region, 3) the air entrainment mechanisms and the bubble field around the boat, 4) the bubble dissolution times, and 5) visually document the free surface and the subsurface bubble transport. In total, eleven separate instrumentation systems were deployed, as well as seven above water and three underwater camera systems. The sea trial test was performed with varying ship speeds of 6, 9, 10.5 and 12 knots, equivalent to Froude numbers based on length (47 m) of 0.14, 0.21, 0.24 and 0.29, respectively. The sea trial tests of a 294.6 tonne Catamaran, SEA FLYER, having a hydrofoil of 10 meter chord and 11 meter span, covered with polymer injection, showed that as much as 60% reduction in the viscous drag component could be achieved (e.g. Moore et al., 2006). Terrill and Taylor (2007) measured the full-scale wave field using LIDAR (Light Detection and Ranging) onboard a naval surface ship.

Herai, et al. (2010) verified the effectiveness of a newly developed energy saving appendage in full scale measurements. The full scale measurements are also focused on evaluation of ship propulsion performance in actual sea environments: e.g., Minoura et al. (2008a) and Minoura (2008b) for ship speed loss and other related phenomena by analyzing onboard measurement data; Sasaki et al. (2008) for speed loss of large container ships operating in a sea way; Shoji et al. (2008) for analysis method for ship performance by using an abstract logbook; Yamamoto et al. (2010) for full scale measurement data of large container ships on the effect of the hydroelastic response; and Kano et al. (2010) for measured wave spectra by coastal vessels and estimated added resistance in waves.

2.4.3 Drag reduction

The reduction of skin friction drag through turbulent boundary layer control has been of great interest from the viewpoint of energy efficiency since the late 90's. By the year 2005, the economic benefit of a 30% drag reduction in the ocean shipping industry was estimated to be 31Billion US Dollars per year (Meng, 2005), which was based on $50/barrel, half of today's oil price. There was a consensus to share the state-of-the-art research outcomes and a prospect toward the realization of drag reduction technologies between academia, research institutes and government agencies worldwide. Hence the 2nd International Symposium on Seawater Drag Reduction (ISSDR 2005) was held in Busan, Korea seven years after the 1st Symposium in Newport, Rhode Island, US. The Symposium, jointly organized by US ONR (Office of Naval Research) and ASERC (Advanced Ship Engineering Research Center), Korea, witnessed the applicability of drag reduction strategies combined with novel experimental as well as theoretical analysis techniques. The proceedings of ISSDR 2005, with 57 papers by the pre-eminent researchers worldwide, is a good example of cutting-edge technology of drag reduction . This section is based on the major research results reported in the proceedings and the subsequent journal publications from 2005 to 2007. The paper of Joslin et al. (2005) presents a good reviewon this topic, it encompasses nearly the whole aspect of flow control, and also a unique perspective on the synergism of flow and noise control technologies relevant to both air and undersea vehicles is suggested.

Microbubble Injection is currently regarded as the most promising in terms of realization. The applicability of this method has been demonstrated from a full-scale experiment on a 114 m training ship, SEIUN-MARU (Kodama et al., 2004a) and a 50m-long flat plate experiment (Kodama et al.,2004b).

In order to identify the drag reducing mechanism in more detail, a main issue of the research has been shifted to the deeper understanding of the drag-reducing mechanism by means of DNS (Direct Numerical Simulation) and PIV. Ferrante and Elgobashi (2005) investigated the effect of Reynolds number on the drag reducing efficacy of microbubbles in a turbulent boundary layer at Re=1430 and Re=2900 numerically. They showed that the percentage of drag reduction. Kitagawa et al. (2005) demonstrated a novel experimental technique to visualize the interaction between the flow field and the microbubbles by means of PIV combined with a shadow image technique (SIT). Shen et al. (2006) made an assessment on the effect of bubble diameter on the drag reduction efficiency in a turbulent channel flow. The results indicate that the measured drag reduction by microbubbles is essentially independent of the size of the microbubbles over the size range tested ($18 \le d+ \le 200$). The research by Kodama et al. (2006) showed that the drag reducing efficacy depends on the deformable character of bubbles, which is governed by Weber number. In case of less deformable (rigid) bubbles with We=50, the local skin friction could increase. The research by Sanders et al. (2006) is probably the most notable experimental endeavour to extend the Reynolds number, Rex, to as much as 210 million, which is only one order less than that in real ship flows. The authors found that there are many different phenomena leading to the decrease of drag reduction efficiency in the previous results in low-Reynolds number flows. Murai et al. (2007) suggested the possibility of drag reduction using relatively large air bubbles, which is the intermediate case between the microbubble and air film conditions. Kunz et al. (2007) showed a comprehensive summary on the validation status of a CFD tool development program for microbubble drag reduction predictions. An Eulerian two fluid model has been presented with specifics regarding physical models for interfacial dynamics, breakup and coalescence.

The second method of drag reduction is Polymer Injection. Baik et al. (2005) shows how PIV techniques can be used to study changes in the configuration of the injected polymer and in the structure of the velocity field with increasing drag reduction. In Jovanovic et al. (2006), turbulent drag reduction by dilute addition of high polymers is studied by considering local stretching of the molecular structure of a polymer by small scale turbulent motions in the region very close to the wall. The stretching process is assumed to restructure turbulence at small scales by forcing these to satisfy local axial symmetry with invariance under rotation about the axis aligned with the main flow. Deutsch et al. (2006) tested combined gas injection upstream of polymer injection. They reported higher levels of drag reduction than those obtained from the independent injection of polymer or microbubbles alone over a wide range of test conditions. These increased levels of drag reduction with combined injection were often greater than the product of the drag reductions obtained by the independent constituents, defined as synergy. Moore et al. (2006) performed a sea trial test using the ONR technology demonstrator vessel, SEA FLYER to characterize the performance of advanced polymer drag reduction.

Compliant Coatings are probably the most commonly used and yet the most controversial of all the drag reduction technologies. Bandyopadhyay et al. (2005) reported the experimental results from a collaborative effort between the USA, Russia and UK on the development of compliant coatings for undersea application to the reduction of drag; mainly focused on the "shelf-life" of the coatings. It has been showed that, with some exceptions, drag reduction generally deteriorates with the age of the coatings.

In the past three years in Japan, air lubrication to reduce ship frictional drag was reported in numerous publications. These studies were initially carried out as a domestic Japan research project, which involved into development of the devices, model scale experiments to evaluate the effectiveness of the devices and to investigate the related flow physics, development of numerical models for simulation, and finally full scale measurements. For example, Makino et al. (2008) reported the effect of surface curvature on skin friction reduction by air bubbles, Hinatsu et al. (2008) and Kodama et al. (2008) presented a full-scale air lubrication experiment using a large cement carrier whose overall length is 126.6m, Murakami et al. (2008) performed numerical simulation of flow around a full scale ship equipped with bubble generators, and Kawanami and Hinatsu (2010) performed bubble flow visualization around a ship equipped with an air lubrication system. The results of the full scale test can be summarised as follows: a maximum of 11% reduction in ship resistance, power savings of 4 % and 6% for full and ballast loads, respectively, and 40% reduction in local skin friction on the hull bottom.

The activity to develop an air lubrication system in Japan was taken over by a private shipyard. Recently, Mitsubishi Heavy Industries built a module carrier YAMATAI and YAMATO whose overall length is 162m, for which an air lubrication system was equipped. Some reports to describe the work were presented: e.g., Takano et al. (2010) presented the overall system and evaluation through the full scale ship test, Kawakita (2010) investigated a related study, i.e., prediction accuracy of full scale wake distribution required by propeller design, and Takano et al. (2010) presented the behaviour of injected air on the ship bottom and its influence on the propeller. In summary, the results from the full scale test are that a maximum of 12% power saving was achieved for 7mm thickness in air layer and more effective benefits can be achieved with more air flux.

The air layer/cavity drag reduction activities in Europe during the SMOOTH (Sustainable Methods for Optimal design and Operation of ships with air-lubricaTed Hulls) project have been compiled and reported in the international conference on ship drag reduction (SMOOTH-Ships) on May 20-21, 2010 in Istanbul, Turkey. The SMOOTH project, a sequel to the PELS projects, was carried out by many organizations including classification bodies, shipyards, coating and shipping industry, universities and research institutes in Europe from 2006 to 2010. In his keynote speech, Thill (2010) reported a contradicting view compared with the Japanese’s promising views, showing that the micro bubble lubricated test ship Till Deymann showed hardly any improvement in terms of power saving and even a negative net energy saving by considering the air compressor power input. Ceccio et al. (2010a) gave a cost-benefit analysis for air layer drag reduction, emphasizing the importance of persistence length of the air layer and the draft concerns in order to accomplish a net energy saving in consideration of air pumping cost.

In Russia, research activities on drag reduction by air lubrication and air cavity have been widely known with many full scale ship applications. The state of the art of the air lubrication technologies together with current research activities in Russia can be found in Sverchkov(2010).

Reduction of frictional drag and related subjects were also studied in various approaches. A notable compilation of the most recent experimental as well as numerical progress can be found in the proceedings of the EDRFCM 2010 (European Drag Reduction and Flow Control Meeting). Among various strategies are plasma control and using a plasma actuator caught the attention for aerodynamic applications (Whalley and Choi, 2010; Berendt et al., 2010). Total drag reduction capabilities of outer-layer vertical blades, a vertical LEBU (Largy-Eddy BreakUp device), was clarified by Lee et al. (2010).

Kulik et al. (2010) reported that a new type of “stiff” compliant coating with enough endurance for real application led to drag reduction in a fully turbulent boundary layer. Recent trends in journal publications in the field of frictional drag reduction are mainly focused upon the use of polymer/surfactant injection and surface morphology using superhydrophobic surfaces. For bubble and gas injection, Ceccio (2010b) gives an extensive review. Notable progress in the identification of drag reduction mechanisms in the case of polymer injection can be found in Somandepalli et al. (2010) with quantification of concentration flux using PIV/PLIF investigation and Cai et al. (2009) to combine POD (Proper Orthogonal Decomposition) with PIV measurements. The consideration of super-hydrophobic coating is associated with the recent developments of microfabrication technologies. There are frequently found controversies regarding the drag reduction efficiency of superhydrophobic surfaces in submerged condition; Daniello et al. (2009) stated effectiveness of such coatings for even the totally turbulent regime, whilst Su et al. (2009) demonstrated that the microbubbles at the superhydrophobic surface increased the friction. The assessment of frictional drag reduction could be affected significantly by the choice of a specific experimental method. It is worth mentioning that the comparative evaluation of skin friction reduction capability, which was performed by the Ceccio group at the University of Michigan, gave no evidence that any of the currently reported skin-friction reducing superhydrophobic coatings really leads to skin friction reduction.

2.4.4 Uncertainties in EFD

This section reviews uncertainty assessment in EFD and its utilization to improve accuracies of both raw data and derived quantities. The usefulness in quantifying uncertainty for a test is to aid in both designing the experiment and in formalizing the expected quality of the outcome so that the customer will know what can be expected from the test. The outcome of any test will be dependent on the entire experimental process. The process includes the design of the experiment, the techniques employed, the instrumentation selected, the flow quality of the facility and both the reduction and presentation of data and data adjustments or corrections to convert the data to the appropriate reference condition (AIAA, 1999). Identification and assessment of significant error sources contributing to uncertainty at each step of the process are thus essential, and will be highlighted in this section; since the definition pertaining to uncertainty and the mathematical tools for estimating uncertainty have been reported in various sources (Coleman and Steel, 1999; AIAA, 1999, 2003; ASME, 1998).

Errors occur at every link in the chain of measurements and the data reduction from the sensor to the final result and are sources of uncertainty. Paying close attention to the major error sources can dramatically simplify uncertainty analyses. In accordance with AIAA Standards (1999), the sources of error can be classified as test techniques, model, flow quality, instrumentation and mathematical model related. Gui et al. (2001) measured the mean velocity and Reynolds stresses at the nominal wake plane of DTMB Model 5512 in a towing tank with a towed PIV system. The mean velocity was compared with an existing 5-hole Pitot tube data. It has been found that PIV uncertainties are about 1% lower than those for 5-hole Pitot tube. Cowen et al. (2001) reported a single camera coupled PIV-LIF technique applied to measurements in a neutrally buoyant turbulent round jet. Validation measurements show that the uncertainty intervals for the means and turbulent intensities are excellent whilst those for the momentum and scalar flux terms were very good. A method for direct measurement of vorticity (DMV) from digital particle images taken by PIV/PTV is proposed by Ruan et al. (2001). Measurement uncertainty of the DMV method is found to originate directly from the particle image noise and insensitive to the velocity uncertainty. Lang et al. (1999) constructed out-of-plane velocity components from a set of parallel vector maps obtained by a two-dimensional PIV with application of continuity equation. The smallest uncertainty in cross flow component constructed found by comparing to a CFD results was a RMS error of 3.52%. Bias and precision errors of digital particle image velocimetry (DPIV) were quantified by Forliti et al. (2000). Bias errors are found to exist for all sub-pixel peak finding algorithms and the presence of the biases tend to affect the precision error. Zhang et al. (2002) estimated the uncertainties of stereoscopic particle image velocimetry (SPIV) measurement and found that the angular-displacement method can provide up to 40% higher out-of-plane accuracy than the translation method. Olivieri et al. (2003) investigated flow structures under bow breaking wave generated by a model of fast displacement ship. Wave heights were measured by a finger probe and mean velocity fields with a 5-hole Pitot tube. Uncertainties of the measured velocity components u, v and w were found to be 0.69%, 1.47% and 1.58%, respectively. Martin et al. (2000) measured the wake of a scaled helicopter rotor operating in hover. It was suggested that a quantitative estimate of source of LDV measurement bias, especially gradient bias, should be included and the ratio of effective length of the probe volume to the smallest expected vortex core radius should remain less than 5% to minimize gradient bias. Petrovic et al. (2003) analysed the measurement accuracy of a different hot-wire probes processing between two and 12 sensors. It was found that neglecting the instantaneous fluctuations of the velocity gradients for the measurement of the cross-stream velocity component has a crucial influence and results in large errors. Reis et al. (2002) described a method for the estimation of uncertainty in measurements of aerodynamic loads using an external balance and reported a recent assessment of the friction forces and corresponding uncertainties in order to better evaluate the contribution. (Reis et al., 2003).

2.5 Application of commercial CFD software

During the past few decades, computational fluid dynamics (CFD) were developed and implemented in modern software packages and widely used for numerical simulation of fluid flows. Some capabilities of modern CFD software packages for modelling of complex physical processes in fluid flows are described by Kochevsky (2004) and Nenya (2004).

Many software packages for solution of fluid flow problems are available. Many can be found at the site www.cfd-online.com. Among these CFD packages, the most recognized are the following packages: CFX (www-waterloo.ansys.com/cfx/), Fluent (USA, www.fluent.com), STAR-CD (England, www.cd-adapco.com, www.adapco-online.com), Numeca (Belgium, www.numeca.be), etc. The packages FlowER (Ukraine, www.flower3d.org) and FlowVision (Russia, www.tesis.com.ru, www.flowvision.ru) are also worth mentioning.

Initially, the CFD was developed for solving problems in the aerospace industry, such as processes in combustion chambers of rocket engines, physical-chemical processes in the flow around rocket airframe and supersonic aircrafts. Nowadays, the field of application of CFD has also been extended to civil engineering problems.

According to information presented at those sites, we list some examples of application of the CFD: (1) prediction of resistance caused by upstream air or water flow; (2) ventilation and fire safety of passenger compartments; (3) simulation of fuel combustion in combustion chambers; (4) prediction of performance curves and operation modes of pumps, compressors and turbines at different configuration of flow passage; (5) prediction of cavitation phenomena and (6) simulation of combustion flows in the burners and boilers of heat power plants.

In this project, FLUENT software is used to solve the hydrodynamics of the GHC. More details are given in Chapter 5.

3. EXPERIMENTAL STUDY OF HYDRODYNAIMCS OF PLANING CRAFTS

As indicated in Chapter 1, the GHC is close to a planing craft. The main difference is that there is a hydrofoil mounted in the front part of the hull. Before carrying out the experimental study on the GHC, it is essential to study the hydrodynamics of planing crafts. By comparing the hydrodynamics of the GHC and that of the planing crafts, the effect of the extra hydrofoil in the craft performance and hydrodynamic feature can be evaluated. This chapter presents the hydrodynamic test of a planing craft model. The main difference between the planing craft model and the model of the GHC is that the model of the GHC has a hydrofoil.

3.1 Ship model design

The exterior form of a ship's hull is a curved surface defined by the lines drawing, or simply "the lines". Ship forms must meet constraints of buoyancy, stability, speed and power, and seakeeping. This is a very important index to evaluate ship design. The main parameters of a ship form are:

(1) Principal dimensions, including length (*L*), breadth (*B*), draft (*d*), depth (*D*), etc;

(2) Coefficients of form, such as the Block Coefficient (C_B), the Prismatic Coefficient (C_P), the Waterplane Coefficient (C_{WP}) and the Midship Coefficient (C_M), etc;

$$C_B = \frac{\nabla}{L \times B \times d},\ C_P = \frac{\nabla}{L \times A_m},\ C_{WP} = \frac{A_{WP}}{L \times B},\ C_M = \frac{A_m}{B \times d}$$

where, ∇ is the volume of displacement; A_m is the immersed area of midship section; A_{WP} is the area of the waterplane;

(3) Local shape, such as types of stern, stem and midship section, deck line, etc.

3.1.1 Body plan of the planing craft model

The details of the model for our experiments will be firstly introduced. The model is based on a planing ship, which is 11.8m-long with "V"-type planing surface (Yang, 2006). The Fig.3.1 illustrates the lines drawing of the craft.

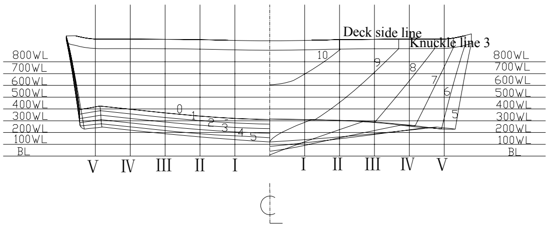

(a) Body plan

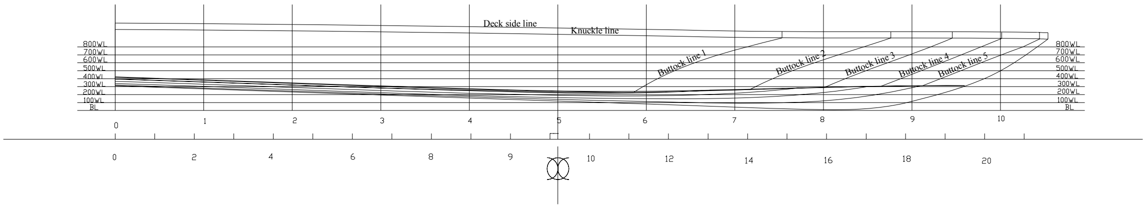

(b) Sheer profile plan

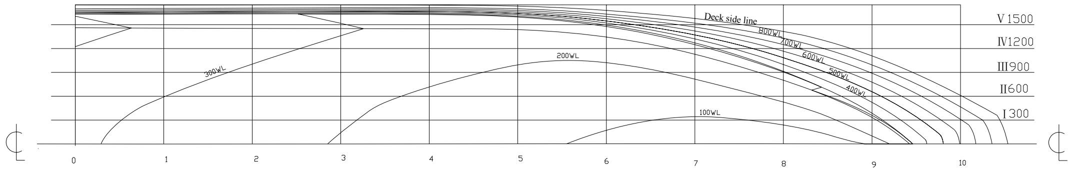

(c) Half-breath plan

Fig.3.1 Lines drawing of 11.8m-long planing craft

The planing craft displacement is 8.144t displacement and its designed speed is 50 km/h. The ship model for the present study is 1:10 scaled model of the vessel.

Table 3.1 Principal dimensions of planing craft

	Full-scale	Model-scale
Scale ratio	10	
Length (m)	11.8	1.18
Breadth (m)	3.5	0.35
Draft (m)	0.7	0.07
Initial wetted length L_S (m)	11.2	1.12
Initial wetted area S_S (m^2)	41.3	0.413
Weight (kg)	8144	8.144
Designed speed (m/s)	13.89	4.39
Froude number	1.3	1.3
Reynolds number	1.54×10^8	4.89×10^6

The model-scale Froude number ($Fr = U_C/(gL)^{0.5}$) is 1.3 and Reynolds number ($Re = U_C L/\nu$) is 4.89×10^6. The main parameters of the full-scale craft and the scaled model are summarized in Table 3.1.

3.1.2 Building ship model

The ship model is made of wood, fiberglass and plastic. The detailed procedure of how to build the ship model are listed as follows.

1) Building the hull frame.

The major structural elements of the ship model are the centreline vertical keel and the transverse ribbed slab. Fig.3.2 shows the centreline vertical keel of the ship model used in the experiment.

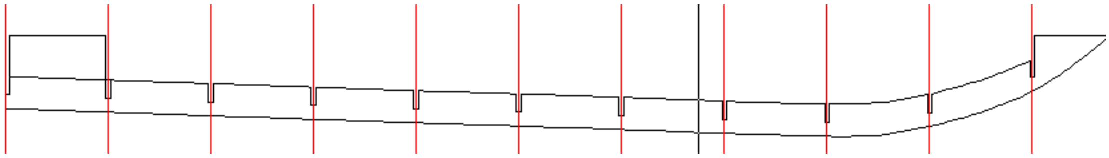

Fig.3.2 Centreline vertical keel of the ship model

Based on the body plan of the ship model, the cross section of each station can be obtained. They are then connected using the centreline vertical keel through the slots. The Fig.3.3 shows the hull frame of the ship model.

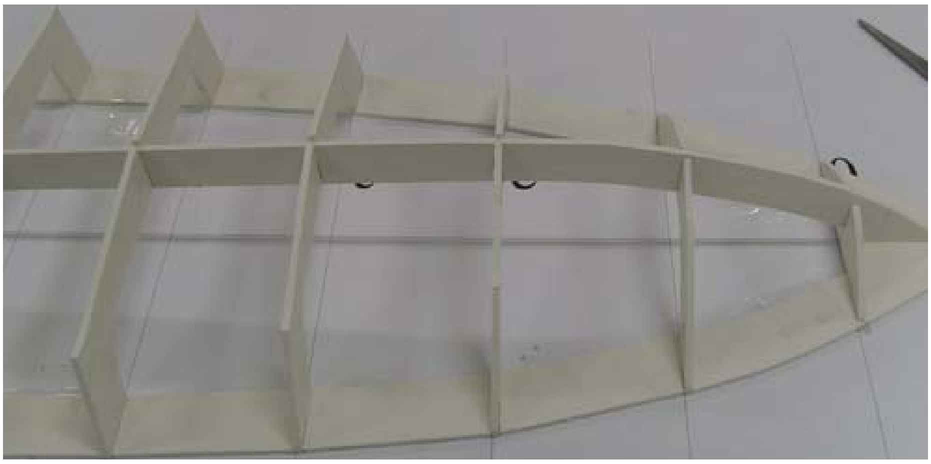

Fig.3.3 The hull frame of the ship model

2) Surface treatment of ship model

Fig.3.4 The surface of ship model

The 2 mm thickness plates, as shown in Fig.3.4, were chosen to build a ship model hull. The process of the hull surface treatment includes polishing, painting and waxing. The purposes of surface treatment are: (1) make the hull surface smooth and reduce the resistance; (2) water proof and (3) increase the model aesthetics.

3) Assembling the ship model

The installation of the towing hook is very important when assembling the ship model. The towing hook is installed on a wood board with 100mm(*B*)×15mm(*D*)×300mm(*L*) which is fixed on the deck of amidships. Then the navigation frames on the bow and stern are installed. The top and side views of the assembled ship model are illustrated in Fig.3.5.

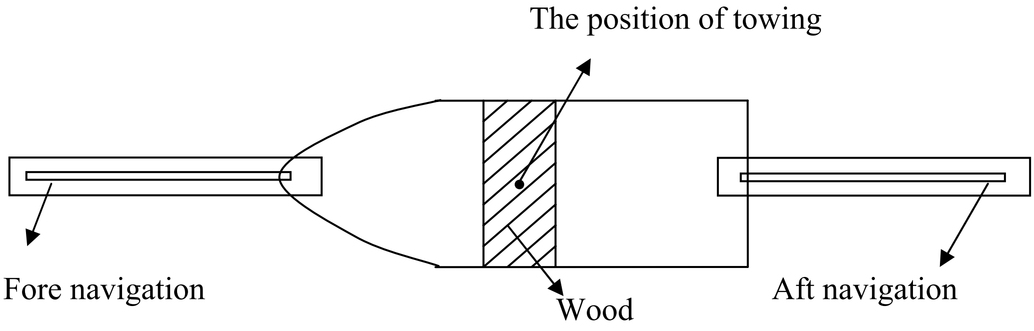

(a) The top view

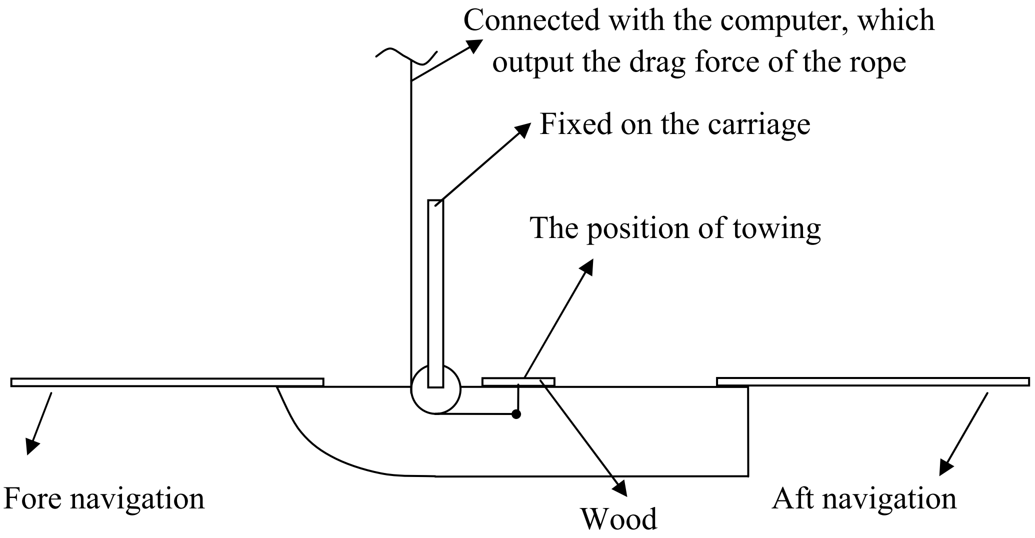

(b) The side view

Fig.3.5 The assembled ship model

3.2 Experimental methods

3.2.1 Towing tank

The model tests are carried out in the towing tank (Fig.3.6) at Jiangsu University of Science and Technology. The length, width and depth of the tank are 100 m(*L*), 6 m(*W*) and 2.5 m(*D*), respectively. The water depth is 2.0 m.

Fig.3.6 Towing tank

Fig.3.7 The carriage

During experiments, the humidity of the laboratory is about 70% and the water temperature is 20℃. An electrically-controlled carriage is used to tow the ship models properly. The maximum and minimum carriage speeds are 6 m/s and 0.01 m/s, respectively. The speed of the carriage and towing distance are controlled by a computer. The errors in the speed are not larger than ±0.1%. The force measurement instruments and displacement sensors are equipped with the carriage to measure the resistance and trim angle of the planing craft model. The total resistance, fore draft and aft draft are also measured using the sensors set up on the towing tank's carriage. A computer is used to control all devices, collect results and post-process data.

3.2.2 Linear Displacement Sensor

Measurement of the distance or displacement between two points in real time may be achieved by a wide variety of sensors. One of the linear sensors utilizes a resistive element having a sliding electrical contact. The resistive element is secured to one member and the contact is secured to the other member. As the members translate relative to one another, the resistance or voltage output varies and indicates the present sensed position. Today, many different designs utilizing moving magnetic or electromagnetic members, Hall Effect sensors and optical devices provide accurate and repeatable translation and position sensing. The Fig.3.8 is the linear displacement sensor.

Fig.3.8 Linear Displacement Sensor

3.2.3 Experimental techniques

The procedure of the model test is similar to those for traditional displacement ships. However, there are some special issues associated with a planing craft. For example, as the ship speed changes, the lift acting on a planing craft changes. Therefore, the displacement of the planing craft used in the experiments will not remain the same as the initial status. How to adjust the towing direction of the ship model and how to arrange the ballasts during the tests are important issues that need to be carefully addressed. For this purpose, some special techniques for the preparation and performance of the experiments are applied and they are discussed in this subsection.

1) Adjust the attitude

For the designed full-scale craft, the initial trim angle is 1 degree for planning crafts. So the ballasts are moved to ensure the draft to remain the same as the designed one after the model is put in the water. The initial values of fore draft and the aft draft are recorded to confirm the model's initial position.

2) Towing method

In this study, the ship model is towed along the axis of the design displacement through the gravity centre (Fig.3.9). It is configured to be moved freely in the vertical direction. The distance between the fore sensor and the aft sensor are measured.

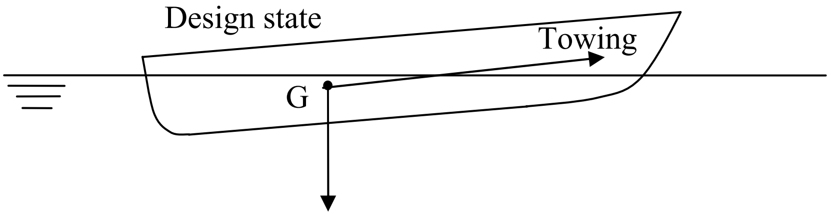

Fig.3.9 Towing method of ship model test

3.2.4 Ship model and test conditions

In the present experiments, the body fit coordinate system is used, which follows the motion of the ship model with its origin being located at the centre of gravity of the ship model. The *x*-axis in the ship model's centre-plane is parallel to the towing direction pointing downstream. Ten towing speeds are chosen from 2.04 m/s to 4.76 m/s to cover the designed speed. They are 1.7, 2.04, 2.38, 2.72, 3.06, 3.4, 3.74, 4.08, 4.39 and 4.76 m/s. This velocity range corresponding to the full-scale speed range of [5.4, 15], which covers all possible cruise speeds. The corresponding Froude numbers are 0.5, 0.6, 0.7, 0.8, 0.9, 1.0, 1.1, 1.2, 1.3 and 1.4.

3.2.5 Measured data and post-processing

In the model tests, the resistance, trim angle and wet area are measured under different towing speeds. For all cases, the corresponding wet length Froude number (Fr_s) and Reynolds number (Re_s) are calculated as follows,

$$Fr_S = U_C / (gL_w)^{0.5} \tag{3.1}$$

and

$$Re_S = U_c L_w / \nu \tag{3.2}$$

in which, U_c is the towing speed , L_w is the wetted length of the ship model with a specific forward speed and ν is the kinematic viscosity coefficient of water. Since the wetted length of the ship changes under different navigation conditions, $Fr_{s,}$ is preferred when analyzing the hydrodynamic properties. However, before the model test is run, e.g. during the ship design process, the wetted length of the ship under different conditions is unknown and therefore of difficult evaluation. On the other hand, the length of the craft is specified and independent of the navigation conditions. Therefore, the Froude number (Fr) calculated using

$$Fr = U_C / (gL)^{0.5} \tag{3.3}$$

may be better for guiding the ship design. The Froude number based on length L is also calculated for each towing speed.

The resistance (R_t) is measured using a sensor. In order to compare the results under different test conditions, the dimensionless resistance coefficient (C_d) is calculated for each cases using

$$C_d = \frac{R_t}{\frac{1}{2}\rho U_C^2 S} \tag{3.4}$$

where ρ is the density of water and S is the wetted area of ship model with a certain forward speed.

For a planing craft at the cruise speed the planing surface provides lift forces to support the weight of the craft and a portion of the ship is lifted out of the water. Therefore, the planing craft advances with a certain trim angle and sinkage. A positive trim angle means that the bow is upward and the sinkage is positive downward. The magnitude of the trim angle and the sinkage affects the navigation performance of the craft. The trim angle (θ) is calculated using the fore draft and aft draft measured in the experiments,

$$\tan\theta = \frac{(f_0 - f_t) - (a_0 - a_t) - (d_f - d_a)}{l} \tag{3.5}$$

where, f_0 and f_t are the reading of the fore sensor in the initial condition and in the steady status (referred to as steady reading), respectively; a_0 is the initial reading of aft sensor and a_t is the steady reading of aft sensor; d_f and d_a are the initial fore draft and aft draft, respectively; l the distance between two sensors as shown in Fig. 3.10.

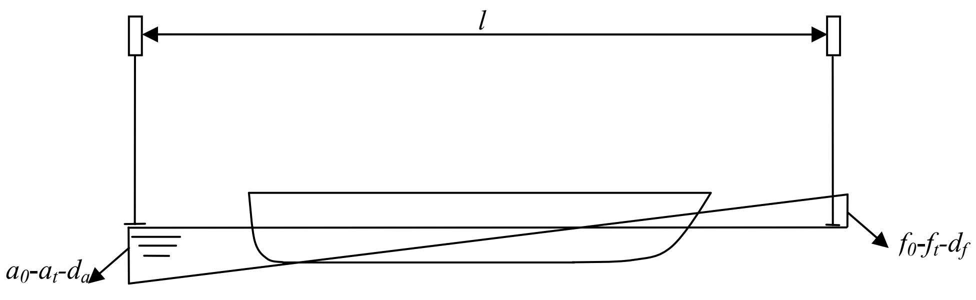

Fig.3.10 The water line at stable state

As indicated above, the displacement of the planing craft is changing during the tests and thus the wetted area is changing as well. The wet area is not easy to be directly measured during the experiments. Alternatively, it may be evaluated using the measured data of the trim angle. For this purpose, the water line corresponding to the trim angle and the wetted length at each status was determined (Fig.3.9). According to this water line, the wetted perimeter of the immersed cross sectional area at each body plan station can be obtained and therefore the wet area can be integrated.

$$S = \int_0^L \Gamma(x)dx \tag{3.6}$$

where, $\Gamma(x)$ is the wetted perimeter of the submerged cross-sectional area at each body plan station.

3.3 Results and discussion

A craft is planing when the length Froude number $Fr > 1.2$ (Savitsky 1992). During planing, the weight of the craft is mainly supported by hydrodynamic pressure loads, with buoyancy being less important. But when the speed continues to increase, the negative pressures relative to atmospheric pressure on the hull also increase. Pressures less than atmospheric pressure may result in dynamic instabilities of the vessel.

3.3.1 Resistance coefficient

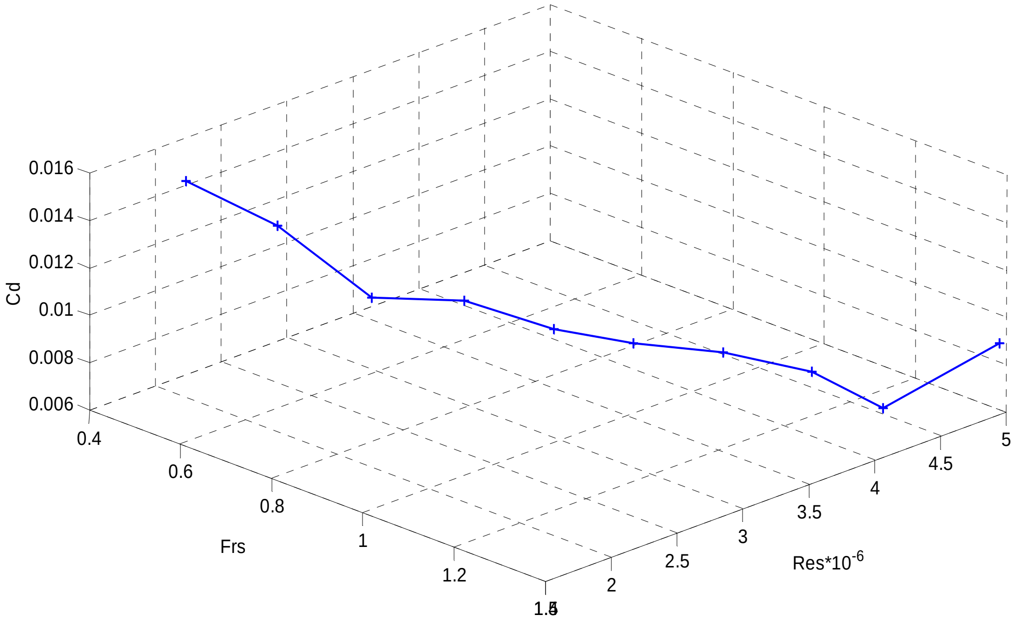

Fig.3.11 The resistance coefficient corresponding to different Froude and Reynolds numbers

Fig.3.11 presents the resistance coefficient against Froude and Reynolds numbers. This figure shows that when the Froude number less than 1.3 and the Reynolds number less than 4.2×10^6 the resistance coefficient decreases with the increase of Froude and Reynolds numbers. Beyond the values, the resistance coefficient increases along with Froude and Reynolds numbers. On the other hand, the trim angle goes oppositely, i.e., grows and then fall down along with Froude and Reynolds numbers, as shown in Fig. 3.12. They are clearly correlated.

3.3.2 Optimum Trim angel

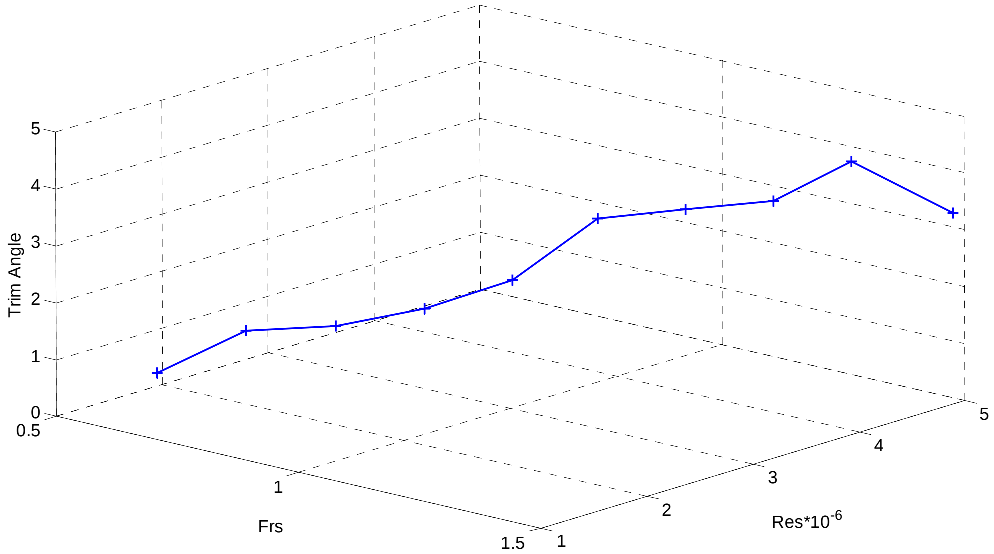

Fig.3.12 Trim angle corresponding to different Froude and Reynolds numbers

As has been seen from the previous two figures, the resistance is closely correlated to the trim angle. This suggests that it may be interesting to look at the optimum trim angle corresponding to the minimum resistance. For this purpose, Fig. 3.13 is plotted for the same cases shown in Figs. 3.11-3.12. As shown in this figure, when Frs=1.4 and Res=4.4×10^6 the resistance coefficient is minimum and the correspond trim angle is 4.3°. We may conclude that an optimum trim angle for this ship model from a resistance point of view is 4.3°. However, the value of the optimum trim angle depends on the hull form, and would be different for hulls which are not geometrically similar to this one.

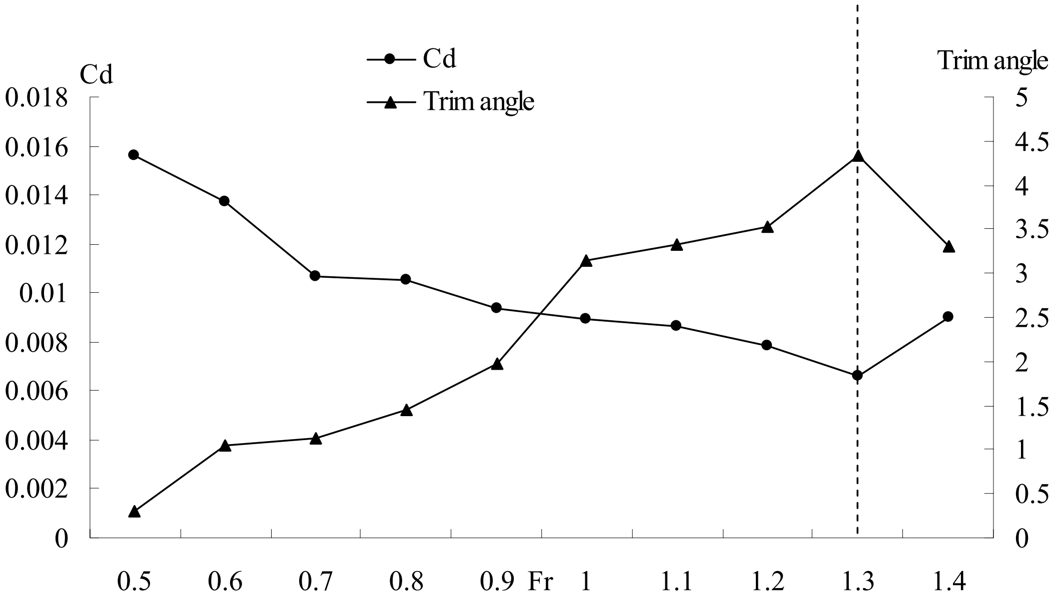

Fig.3.13 The optimum trim angle at planing speed from a resistance point of view

3.3.3 Comments on the empirical equation

When a craft is planing in the water with a certain forward speed, the forces acting on the hull are illustrated in Fig.3.14. R_v is the viscous resistance, T is the propeller thrust, $\triangle$ is the weight of the craft, N is the force due to nonviscous hydrodynamic pressures acting on the wetted hull, θ is the trim angle of the craft and l_{cg} is the longitudinal centre of gravity measured from the transom stern. The force N acting on the planing surface can be decomposed into horizontal component R_P and the vertical component $F_{L\beta}$. R_P is the pressure resistance and $F_{L\beta}$ is the hydrodynamic lift of planing surface.

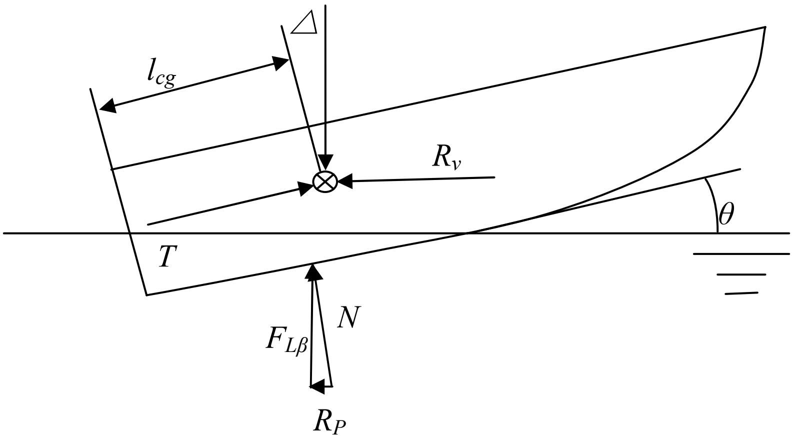

Fig.3.14 Forces acting on the planing craft (take-off status, Faltinsen 2005)

While a craft is in a relatively resting status, we assume that the frictional resistance R_v and the propeller thrust T act through the centre of gravity. In order to get the total resistance of the craft the navigation status of the craft with a speed needs to be decided at first. That means the motion parameters including, for example, trim angle and wetted length, were decided. The calculation is very complicated to decide on the navigation status of the craft according to the principle of the balance of force. If the vertical component force of the thrust of the propeller is neglected and the effect of the static buoyancy is not considered when we calculate $F_{L\beta}$, then the vertical force equilibrium and the moment equilibrium equation can be written as (Faltinsen 2005):

$$\begin{aligned} \Delta &\approx F_{L\beta} \\ l_{cg} &\approx l_p \end{aligned} \tag{3.7}$$

where, l_p is the longitudinal position of the centre of pressure. Through solving the equation (3.7) the navigation status can be decided. Then the total resistance R can be obtained. The details of how to decide the navigation status and how to calculate the naked hull resistance R_t are discussed here.

Navigation status

The empirical formulas were presented by Savitsky (1964) for the lift and centre of pressure coefficients for a prismatic and chine wetted planing hull. The formulas are based on extensive experimental data. The lift coefficient (Faltinsen 2005) can be written as

$$C_{L\beta} = C_{L0} - 0.0065\beta C_{L0}^{0.6} \tag{3.8}$$

Here

$$C_{L\beta} = \frac{F_{L\beta}}{0.5\rho U^2 B^2} \tag{3.9}$$

and

$$C_{L0} = \frac{F_{L0}}{0.5\rho U^2 B^2} = \theta_{\deg}^{1.1}\left(0.012\lambda_W^{0.5} + 0.0055\lambda_W^{2.5} / Fn_B^2\right) \tag{3.10}$$

Further, C_{L0} is the lift coefficient for zero deadrise angle (β=0°)

$C_{L\beta}$ is the lift coefficient

F_{L0} is the lift force for zero deadrise angle (β=0°)

$F_{L\beta}$ is the lift force

λ_W is the mean wetted length-to-beam ratio

$\theta_{\deg}$ is the trim angle of planing area in degrees

θ is the trim angle of planing area in radians

β is the angle of deadrise of planing surface in degrees

B is the beam of planing surface

$$Fn_B = U/(gB)^{0.5} \tag{3.11}$$

The beam is used as a length parameter in the Froude number in Eq. (3.11). The reason for that is that the beam is fixed whereas a longitudinal length, such as the wetted keel length, is not know before the equations of equilibrium for vertical force and trim moment for a given speed are solved. Eq. (3.8) is valid for $2^\circ \le \theta_{\deg} \le 15^\circ$ and $\lambda_W \le 4$. Fig 3.15 illustrates the definition of parameters associated with the hull geometry and the angles β and θ. The mean wetted length-to-beam ratio λ_W is equal to $0.5(L_K + L_C)/B$ (see Fig.3.14). L_K and L_C are, respectively, the keel and the chine wetted lengths. Sabitsky's formulas assume a prismatic hull form; for example, the deadrise angle is constant along the craft.

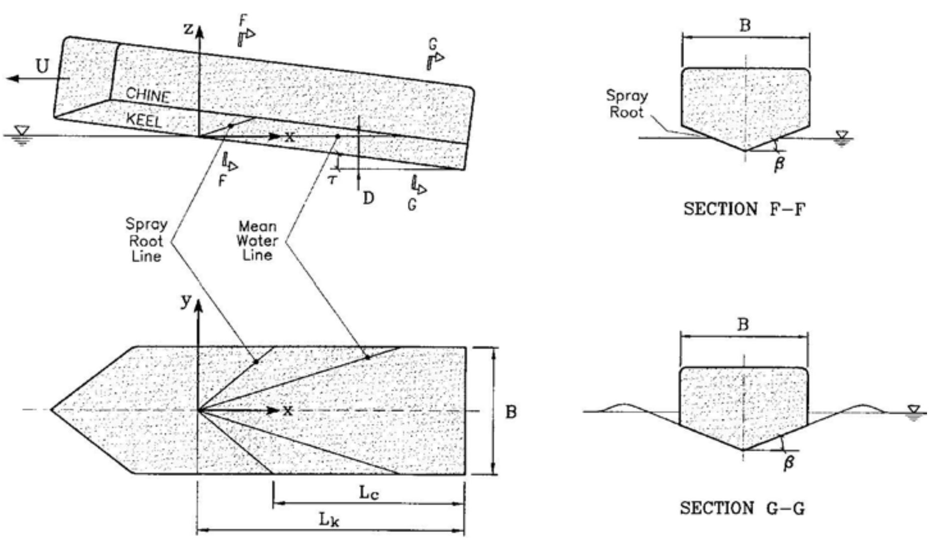

Fig.3.15 Coordinate system (x, y, z) and symbols used in a prismatic planing craft analysis (Savitsky 1964)

The longitudinal position of centre of pressure is expressed by:

$$\frac{l_p}{\lambda_w B} = 0.75 - \frac{1}{5.21 Fn_B^2 / \lambda_w^2 + 2.39} \qquad (3.12)$$

where l_p is the distance measured along the keel from the transom stern to the centre of pressure of the hydrodynamic force.

Naked hull resistance

The total resistance R of the craft with a speed consists of naked hull resistance R_t, air resistance R_{AA} and appendages resistance R_{AP}, which can be expressed as follows.

$$R = R_t + R_{AP} + R_{AA} \qquad (3.13)$$

The naked hull resistance of the planing craft consists of spray resistance, friction resistance and wave resistance. If the trim angle of the craft is θ, the horizontal force component of the resultant force of the friction resistance R_f and the hydrodynamic force R_n is the naked hull resistance R_t, there is a relationship between them:

$$R_t = R_P + R_\upsilon / \cos\theta = F_{L\beta} . \tan\theta + R_f / \cos\theta \qquad (3.14)$$

In Fig.3.15, if the trim angle θ is small then $\tan\theta \approx \theta$ and so:

$$R_P = F_{L\beta} \cdot \tan\theta = F_{L\beta} . \theta \qquad (3.15)$$

Here θ is in radians. After we calculate the trim angle θ and the wetted length l are calculated using the eq. (3.7), the pressure resistance $F_{L\beta}\theta$ can be found. The friction resistance R_f, can be calculated according to the flat plate friction resistance formula when the effect of the form factors ignored (i.e. the bending of the hull shape).

(1) Parameters required

For the planing craft designed in this study, the given data are shown in table 3.2.

The resistance can then be investigated. Savitsky (1964) did this by extensive use of graphs. However, a computer program can easily be made to determine the total resistance. The necessary steps, as suggested by Faltinsen (2005) are explained here.

Table 3.2 The given data for the planing craft

Displacement △ (kg)	8.144
Designed speed (kn)	8.53
Beam B (m)	0.35
Deadrise angle, β (°)	6
Beam Froude number Fn_B	2.37

(2) Calculation

Step 1 Average wetted length-to-beam ratio

Because the forces act through COG, l_p has to be equal to l_{cg}. Eq. (3.12) determines then the average wetted length-to-beam ratio λ_w. The unknown λ_w is therefore the solution of the nonlinear equation

$$\frac{l_{cg}}{\lambda_w B} - 0.75 + \frac{1}{\left[5.21 Fn_B^2 / \lambda_w^2 + 2.39\right]} = 0$$

The numerical solution gives answer λ_w=2.03166 for our case.

Step 2 Trim angle θ

We now use the fact that the lift force calculated by Eq. (3.8) balances the weight of the craft, that is,

$$C_{L\beta} = \frac{\Delta g}{\frac{1}{2}\rho V^2 B^2}$$

Using the mass density of water at 15℃, that is, ρ=1000kg/m^3 gives $C_{L\beta} = 0.0677$. Eqs. (3.9) and (3.10) are used to determine the trim angle θ by solving the equation

$$0.067 - (C_{L0} - 0.0065\beta C_{L0}^{0.6}) = 0$$

The solution is $\theta = 2.84°$

Step 3 Wetted length

The length $x_s = L_K - L_C$ along the keel from the intersection between the keel and the mean free surface until chine wetting starts is first defined. This can be obtained by

$$\frac{B}{2} = \frac{\pi}{2\tan\beta} x_S \theta \tag{3.17}$$

in which θ is given in radians. The chine wetted length L_C and keel wetted length L_K follow from

$$\lambda_w = 0.5(L_K + L_C)/B = 0.5(x_s + 2L_C)/B$$

This means $L_C = \lambda_w B - 0.5x_s = 0.592846m$ and $L_K = 2\lambda_w B - L_C = 0.829316m$. The consequence is that the draft of the keel at transom is:

$$D = L_K \sin\theta = 0.0411$$

Step 4 Effective horsepower

The resistance of the craft will now be calculated. The frictional resistance on the hull is obtained by Eqs. (3.18) and (3.19).

$$R_f = (C_f + \Delta C_f).\frac{1}{2}\rho V^2 S \tag{3.18}$$

$$C_f = \frac{0.075}{(\log_{10} Rn - 2)^2} \tag{3.19}$$

Here, C_f is the frictional resistance coefficient, ΔC_f is the roughness coefficient and S is the wetted area of the craft. Using that the kinematic viscosity coefficient $\nu=1.19\times 10^{-6}\text{m}^2/\text{s}$ for water at 15℃ gives a Reynolds number $\text{Re} = UL_K/\upsilon = 3.1\times 10^8$. The average hull roughness coefficient will be set equal to $\Delta C_f = 0.4\times 10^{-3}$. This gives $C_f = 0.003732$.

The wetted area is divided into two parts. The wetted area S_1 from the bow (x=0) up to where chine wetting starts ($x=x_s$) is chosen as the hull area below the spray root. In fact, this wetted part may be larger. It follows by introducing $d(x)$ as the vertical distance from the spray root to the keel at x and eq. (3.20).

$$\frac{B}{2} = \left(1 + \frac{z_{\max}}{Vt}\right)\frac{Vt}{\tan\beta} = \left(1 + \frac{z_{\max}}{Vt}\right)\frac{x_s\theta}{\tan\beta} \tag{3.20}$$

So that

$$S_1 = 2\int_0^{x_s} \frac{d(x)}{\sin\beta} dx = \frac{2}{\sin\beta}\int_0^{x_s}\left(1+\frac{z_{\max}}{Vt}\right)x\theta dx = \frac{\theta}{\sin\beta}\left(1+\frac{z_{\max}}{Vt}\right)x_s^2$$

Using eq. (3.21) to express x_s gives

$$\frac{B}{2} = \left(1+\frac{z_{\max}}{V_t}\right)\frac{V_t}{\tan\beta} = \left(1+\frac{z_{\max}}{V_t}\right)\frac{x_s\tau}{\tan\beta} \tag{3.21}$$

$$S_1 = \frac{\tan^2\beta}{\sin\beta}\left(\frac{B^2}{4(1+z_{\max}/Vt)\theta}\right)$$

$$\frac{z_{\max}}{Vt} = 0.5654$$

The wetted area from $x=x_s$ to the transom is simply

$$S_2 = \frac{B}{\cos\beta}L_C$$

The total area is by setting $1+z_{\max}/Vt = 0.5\pi$ equal to $S = S_1 + S_2 = 0.25\,\text{m}^2$. It follows that the longitudinal frictional force is 10.21N. We have to add the lift-induced resistance given by eq. (3.15) R_P=4.16N. The total longitudinal resistance force is then R_t=14.37 N. Then we repeat all the steps to calculate the total resistance and trim angle of the craft for different navigation speeds.

Repeat all the above steps, the resistance and the trim angle were calculated at different speed. The results are compared with the experimental values, see Fig.3.16.

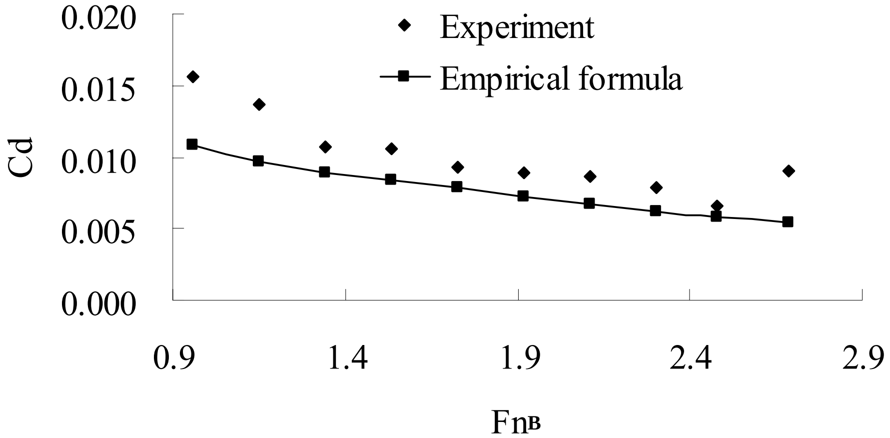

(a) Total resistance coefficient

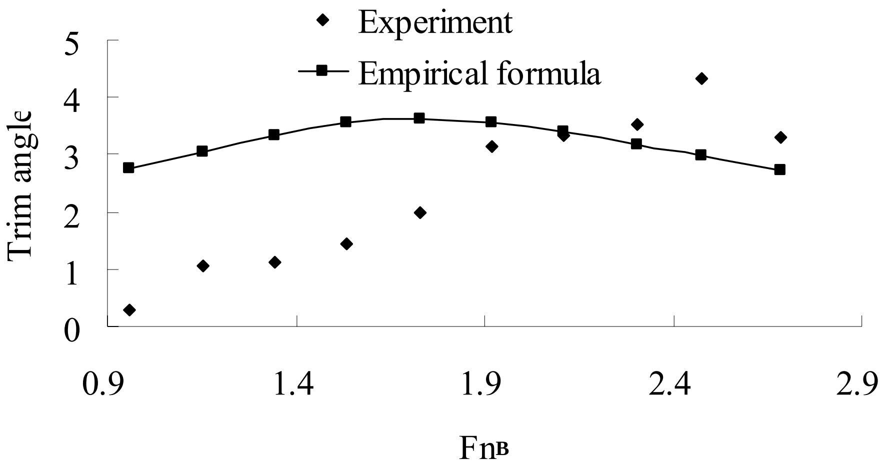

(b) Trim angle

Fig.3.16 Comparison between the experimental data and Savitsky's formula (1964) for total resistance coefficient and trim angle at different navigation speeds

Fig.3.16 shows comparisons between the empirical formula and the experimental results for the total resistance coefficient and the trim angle. Infinite Froude number Fn_B is assumed in Eqs. (3.10) and (3.12). Because there is a simple relationship (see Eq. (3.15)) between R_P and $F_{L\beta}$, results are not presented for $F_{L\beta}$. The figures show that when $1.9 \leq Fn_B \leq 2.4$ the experimental and empirical results are very close but the errors of empirical formula may not be acceptable in other regions. For the planing craft design in this study the designed speed is 8.53 kn ($Fn_B = 2.48$), so the empirical formula may be used for estimating the resistance.

4. EXPERIMENTAL STUDY OF HYDRODYNAIMCS OF GHC

This chapter presents the experimental study on the hydrodynamic feature of the GHC. Similar to the experimental study regarding the planing craft, the resistance coefficient and the trim angle of the GHC model are of most concern. As indicated before, the distinguish difference between the GHC and a planing craft is the hydrofoil installed in the front side of the GHC hull. Therefore, this chapter details the design and the performance of the hydrofoil. In addition, the effects of the initial attack angles and the submergence depths of the hydrofoil are also investigated. Based on the experimental results, an empirical method for predicting the resistance coefficient is suggested, which may provide useful reference for designers and engineers.

4.1 Hydrofoil design

The structure of “TV” type hydrofoil for the GHC is shown in Fig.4.1. In this design, only the chord length of foil needs to be determined. The span length of the hydrofoil of the model ship is obtained by transferring the chord length of the hydrofoil of parent ship using similarity theory, the principle parameters of the parent ship are shown in table 1. The ratio of the model and the parent ship is 1:10. So the length of the ship model is 1.18m, the weight is 8.144kg and the foil span length is 390mm.The design speed of the ship model is 4.39m/s.

Table 4.1 Principle parameters of the GHC (parent ship)

Length (m)	11.8
Breath (m)	3.5
Draft (m)	0.7
Initial wetted length L_s (m)	11.2
Initial wetted area S_s (m^2)	4.13
Weight (t)	8.144
Foil span length (m)	3.9
Design speed V_s (m/s)	13.89
Design speed V_s (kn)	8.54

The following are the details regarding the calculation for the chord length of the hydrofoil of parent ship.

(a) (b)

Fig.4.1 The front view of the TV-shaped hydrofoil (a) and the cross section of the hydrofoil (b)

4.1.1 Lift calculation:

The following calculation steps are to decide the chord length of parent ship's foil, which are all based on the formula from Chapter 2 of Kalezayev (1985).

At first, we estimate the value range of chord length. The span-to-chord ratio λ is related to velocity. The value range is:

$$\lambda = \frac{300}{V_S}(1 \pm 0.4) \tag{4.1}$$

where, $V_s = 27kn$, so $\lambda = 7 \sim 16$. And the chord length $c = \frac{l}{\lambda}$, the span length l equals 3900mm, which means $c = 244mm \sim 558mm$.

When the velocity is in the range of 50~90km/h, the unit load of the hydrofoil is given by the following formula:

$$\frac{D_a}{S_h} = A' \rho V_s^{\ 2} \tag{4.2}$$

Where D_a is the load carried by hydrofoil, S_h is area of the hydrofoil, $A^{'}$ is a dimensionless coefficient. According to the figure in Chapter 2 of Kalezayev (1985), we get $\frac{D_a}{S_h} = 2t/m^2$. In this design, the lift of hydrofoil equals 60% of designed displacement, this means D_a=4.89t. From calculations: S_h=5.88m^2 and therefore, c=440mm.

The lift of the hydrofoil L_f can be written as:

$$L_f = \frac{\rho V_s^{\ 2}}{2} C_L S \tag{4.3}$$

where, the lift coefficient C_L can be defined as:

$$C_L = \frac{k_\varphi \frac{\partial C_L}{\partial \alpha}\left(\alpha + \alpha_0 - \Delta\alpha_0\right)}{1 + \frac{\partial C_L}{\partial \alpha} \cdot \frac{k_\varphi}{\pi\lambda}\left(1+\tau\right)\xi\left(\frac{\bar{h}}{\lambda}\right)} \tag{4.4}$$

$$\Delta\alpha_0 = \frac{\bar{c}}{2}\left(\frac{1}{k_\varphi} - 1\right) \tag{4.5}$$

$$\xi\left(\frac{\bar{h}}{\lambda}\right) = 0.85 + \frac{0.16}{\sqrt{\bar{h}/\lambda}} \tag{4.6}$$

Where k_φ is the dimensionless coefficient, $\frac{\partial C_L}{\partial \alpha}$ is the derivative of the lift coefficient to angle of attack, α is the angle of attack, $\Delta\alpha_0$ is the change of attack angle of zero lift caused by free surface, τ is the corrected value, $\xi\left(\frac{\bar{h}}{\lambda}\right)$ is the function considered the influence of immergence and the span length of foil on the flow domain, $\bar{h}$ is the relative immergence that equals to the chord length divided by immergence, $\bar{c}$ is the relative thickness of hydrofoil that equals to the chord length divided by the maximum thickness.

When we calculate the hydrofoil in viscous fluid, the derivative of the lift coefficient to angle of attack is $\frac{\partial C_L}{\partial \alpha} = 5.5$ and the attack angle of zero lift is $\alpha_0 = 1.74\bar{c}$. In the above formulas, S is horizontally-projected area. Relative submergence depth $\bar{h} = \frac{640}{500} = 1.28$, $\bar{c} = 0.06$, $\bar{f} = 0.06$. And the value of some coefficient are $k_\varphi = 0.952$ and $\Delta\alpha_0 = 0.0015$.

In summary, the chord length is 440mm, the lift of the hydrofoil is $L_f = 4.9t$. Its span is 3900mm and maximum thickness is 26.4mm. Considering the scale ratio to be 1:10 and according to the similarity theory the hydrofoil chord length is 44mm, its span is 390mm and maximum thickness is 2.64mm.

4.1.2 Hydrofoil positions

In order to study the effect of submergence and the initial attack of angle of the hydrofoil, the following issues should be considered:

1. How to adjust the initial attack of angle of the hydrofoil;
2. How to adjust the submergence of the hydrofoil;
3. Strength of the hydrofoil.

We set the initial attack of angle -2 degrees and 0 degree (Yang, 2006). Normally we need two sets of hydrofoil with two different initial attack of angles. In our experiment we changed the initial attack of angle through rotating the frame of the hydrofoil, see fig.4.2.

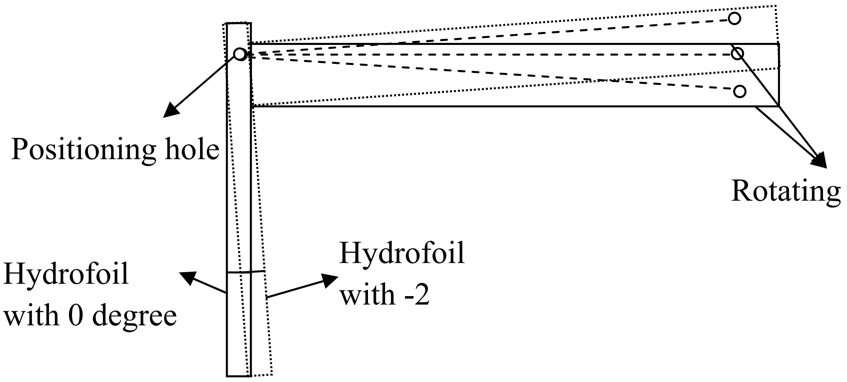

Fig.4.2 Side view of hydrofoil set with different attack of angles of the hydrofoil

Adjustment of the submergence of the hydrofoil is illustrated in Fig.4.3. There are three groups of positioning holes; the submergences are 40mm, 50mm and 60mm respectively.

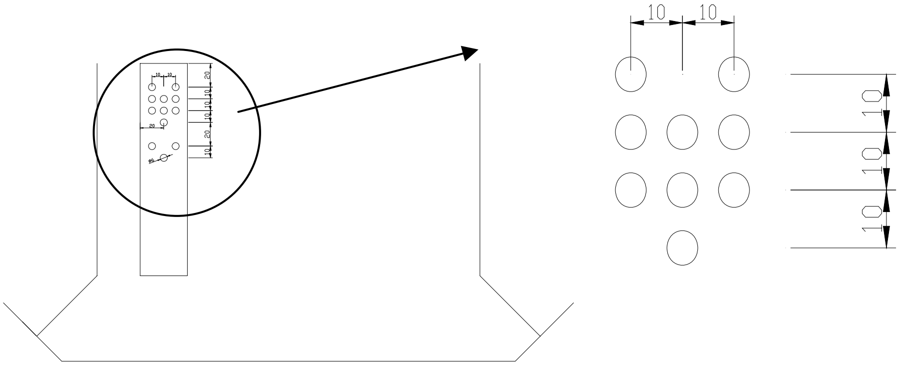

Fig.4.3 Front view of the submergence of the hydrofoil

4.2 Experimental methods

A sketch of the GHC is shown in Fig.4.4. The TV-shaped hydrofoil described above is mounted at a position about 0.43m from the bow. The hydrofoil is made of aluminum. The frame is made of stainless steel. During the tests, the board with a height of 80mm is fixed on the edge of the upper deck to prevent water from spraying on the deck.

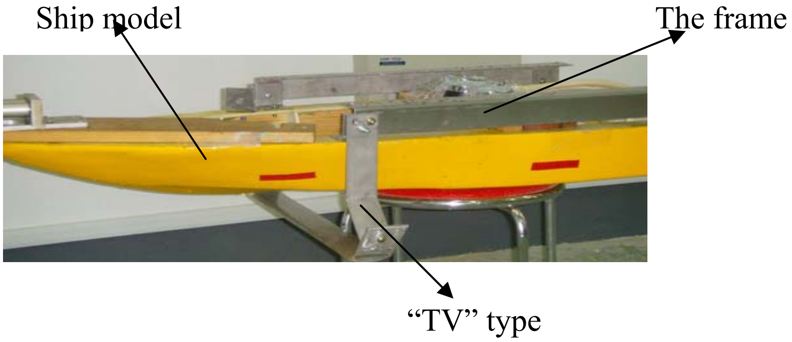

Fig.4.4 The GHC model

The experimental techniques of GHC model test are same as the techniques of planing craft model test. The details can be found in section 3.2.1.

Hydrodynamic characteristics of the model are affected by several parameters, such as the initial attack angle and submerged depth of the hydrofoil and towing speeds. Various cases are considered in the tests to study their effects. Table 4.2 gives the values of the parameters for all the cases.

Table 4.2 Test cases

Ship model	Initial attack angle of hydrofoil	Submerged depth of hydrofoil	Case No.	Towing speed (m/s)								
				1.7	2.04	2.38	2.72	3.06	3.4	3.74	4.08	4.39
Gliding-hydrofoil craft	0 degree	40 mm	I1	√	√	√	√	√	√	√	√	√
	0 degree	50 mm	I2	√	√	√	√	√	√	√	√	√
	0 degree	60 mm	I3			√	√	√	√	√	√	√
	-2 degree	40 mm	I4			√	√	√	√	√	√	√
	-2 degree	50 mm	I5			√	√	√	√	√	√	√
	-2 degree	60 mm	I6			√	√	√	√	√	√	√

4.3 Results and discussion

The model tests were performed in the towing tank under different test conditions with model speeds ranging from 2.38 to 4.76m/s (the corresponding length Froude number ranging from 0.4 to 1.3). For each test condition, the ship model was towed twice. Between the two towing tests, enough time is allowed to eliminate the ship waves. For each model speed, the resistance and the fore/aft draft are measured. The corresponding resistance coefficient and trim angle for each test condition are calculated using Eq. (3.4) and Eq.(3.5). Except measuring the resistance, trim angle and the wet area, a digital camera following the motion of the ship model is also used to record the wave pattern. Fig.4.5 shows an example. Although the wave pattern is not measured quantitatively, those recorded animation is useful for qualitatively analysis.

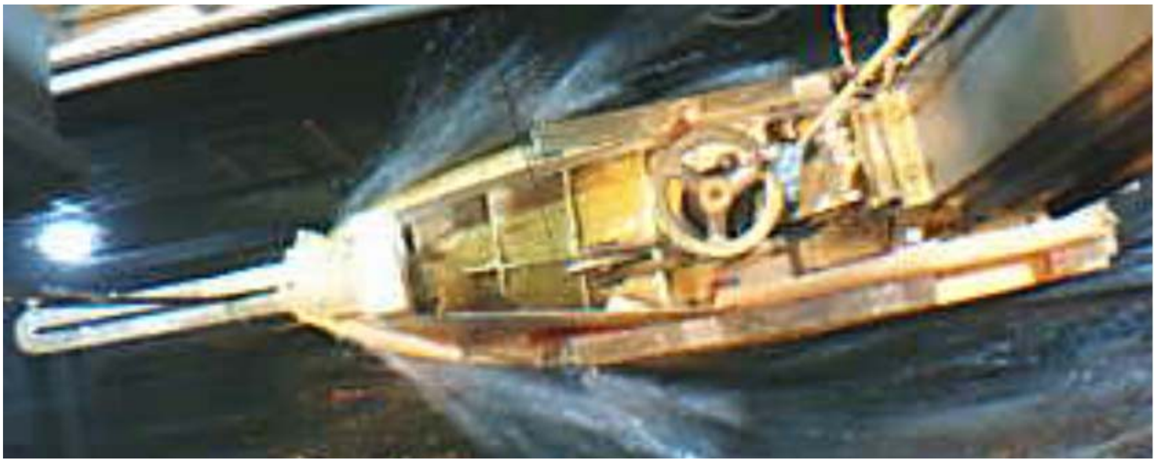

Fig.4.5 Experiment in towing tank

4.3.1 Hydrodynamics of the GHC ship model

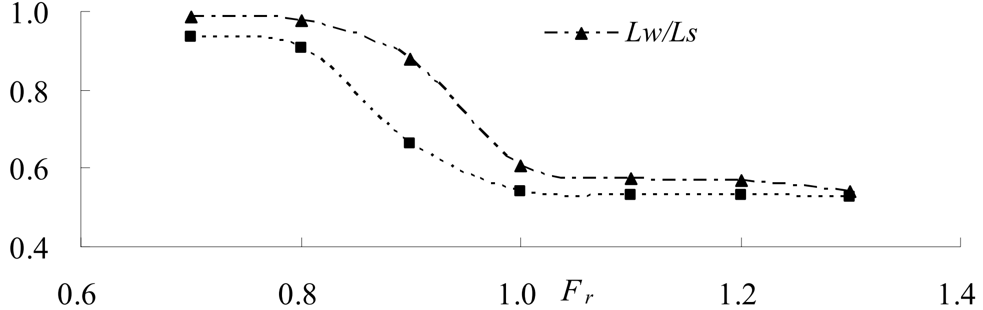

Fig.4.6 Wetted length and area in Case I2 ($Fr_s = U_c / \sqrt{gL_s}$)

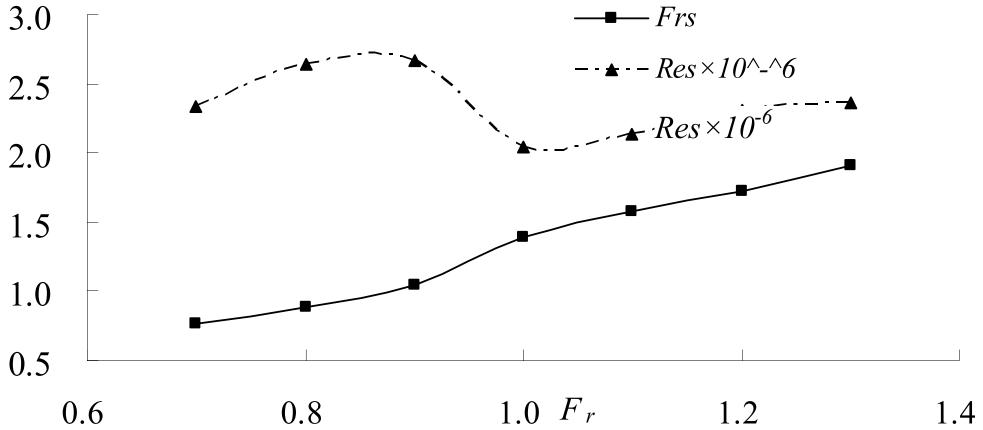

Fig.4.7 Corresponding Froude and Reynolds numbers against the Froude number based on the initial length in Case I2 ($Fr_s = U_c / \sqrt{gL_s}$)

As mentioned above, the corresponding wetted length and area are different for different speeds and thus the corresponding Froude number and Reynolds number are different from those based on the initial wetted length. It is interesting to see how they change with the Froude number based on the initial length ($Fr_s = U_c / \sqrt{gL_s}$, where L_s is the initial wetted length). Fig.4.6 shows the corresponding wetted length and wetted area for Case I2 while Fig. 4.7 presents the corresponding Froude and Reynolds numbers for the same case. It can be seen from Fig. 4.6 that the corresponding wetted length and area looks unchanged in the range of $Fr < 0.8$ or $Fr > 1.0$, though their values are different in the different ranges. In the range of $Fr < 0.8$, the wetted length and area are almost the same as the initial ones. This indicates that the trim angle is very small and the lift force acting on the hydrofoil may not be large enough to lift the model up, which was expected. On the other hand, the wetted length and area remain almost constant but much smaller compared with their initial values in the range $Fr > 1.0$. This implies that the trim angle and lift force on the foil do not significantly vary with the increase of the speeds under the condition. It is also seen from Fig. 4.6 that the reduction of the corresponding length and area are quite rapid in the range of $0.8 < Fr < 1.0$, indicating that the trim angle and the lift force on the foil increase quite rapidly with the increase of speeds in this range. Fig. 4.7 shows that the corresponding Froude number always increases with the increase of speeds, though the rate is different, while there is a reduction in the corresponding Reynolds number between $0.9 < Fr < 1.0$. The latter phenomenon indicates that the rate of the reduction in the wetted length is more rapid than the increase of the speed in this range.

Fig.4.8 and Fig.4.9 show the resistance coefficient and trim angle changes with the change of the corresponding Froude and Reynolds numbers for Case I2, in which the initial attack angle and the submerged depth of the hydrofoil are 0° and 50mm, respectively.

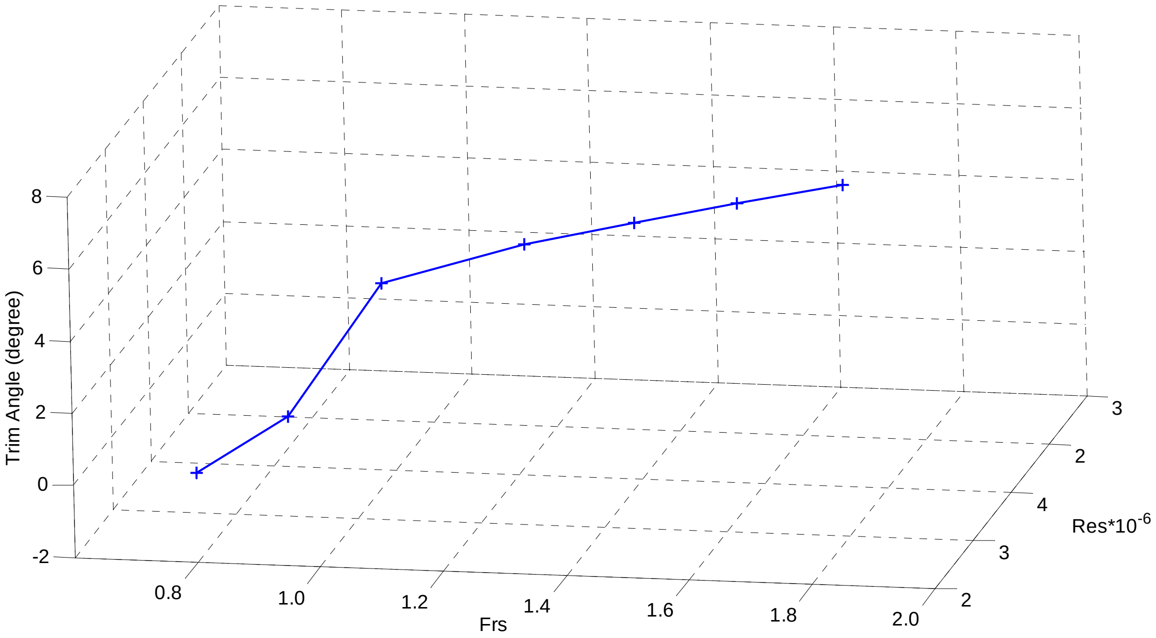

Fig.4.8 The Trim angle of GHC

(Case I2: initial attack angle of the hydrofoil: 0°, its submerged depth: 50mm)

As has been deduced, the trim angle is very small for small Froude number and its rate of change is very low when the Froude number is large (Fig.4.8). Only in the moderate values of the Froude number (0.8 to 1.4), it changes significantly from -2° to 6°. When Fr_s is larger than 1.4, the trim angle is almost a constant (about 6°). Fig.4.9 displays the resistance coefficient. This figure shows that the resistance coefficient has a rapid change in the range of $Fr_s \approx 0.8$ to 1.4, in which the trim angle rapidly increases. After that, the resistance constantly decreases. In this case, the Reynolds number increases to its peak value (about 3.0×10^6) and then has a rapid reduction similar to what has been observed in Fig. 4.7. Thereafter, it increases again as Fr_s increases but very slowly. It is interesting to note that although the value of Reynolds number at the smallest Froude number in Fig. 4.9 is roughly the same as that of the largest Froude number, the resistance coefficient is considerably different. This indicates that the same value of

Reynolds number may correspond to different values of the resistance coefficient and thus it may not be appropriate to use the Reynolds number as the unique dimensionless control number in design of prototype GHCs and model tests. Further research is required to understand the correlation between the Reynolds number and the resistance coefficient.

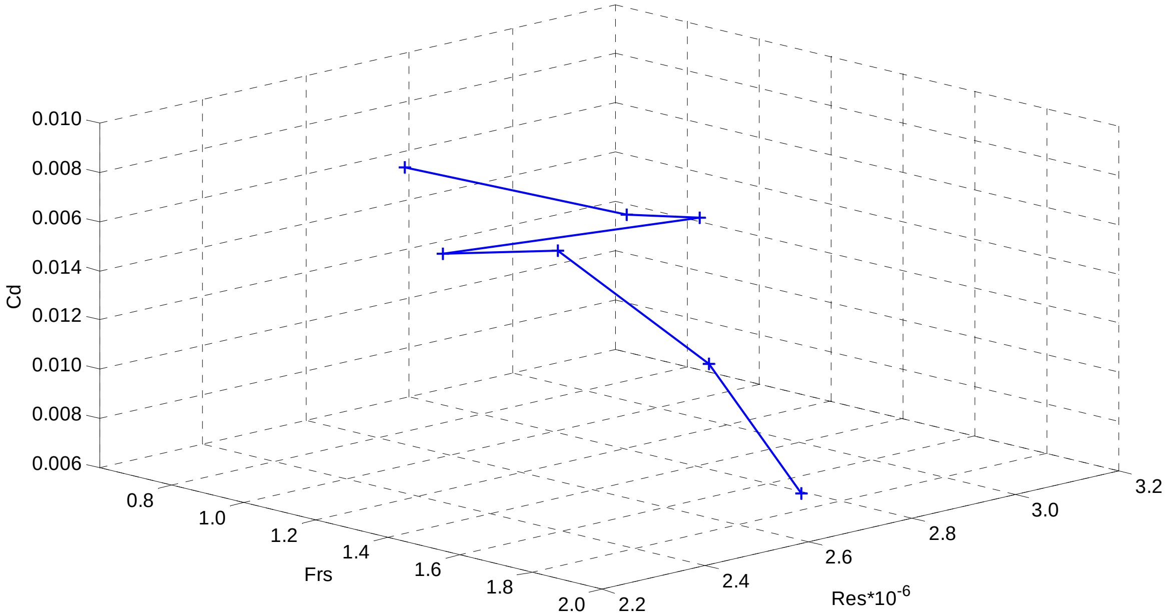

Fig.4.9 The resistance coefficient of the GHC

(Case I2: initial attack angle of the hydrofoil: 0°; its submerged depth: 50mm)

4.3.2 Effect of submergence depth of the hydrofoil

To analyze the effect of the submerged depth of the hydrofoil, Case I1, Case I2 and Case I3 are considered and the corresponding results are depicted in Fig.4.10 and Fig.4.11.

Fig. 4.10 displays the trim angle against the corresponding Froude number for the cases with different submerged depth of the hydrofoil. This figure shows that for all the submerged depths, the trim angle increases as the Froude number increases but the increase rate is very low when the Froude number is large enough. In addition, the trim angle in Case I2 (submerged depth= 50mm) is smaller than others in the whole range of the Froude number tested. More specifically, the trim angle in Case I2 is much smaller from those in other two cases in the ranges of Fr_s <1 and Fr_s>1.4, while the trim angles in the range of 1<Fr_s<1.4 are very close to those of Case I1 (submerged depth=40mm).

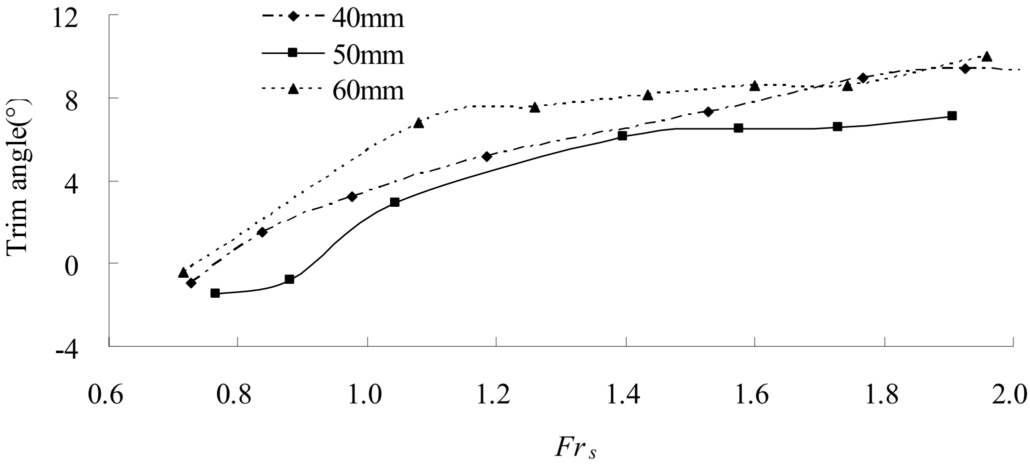

Fig.4.10 Trim angles in Case I1, Case I2 and Case I3 (initial attack angle of the hydrofoil: 0°)

Fig.4.11 presents the resistance coefficients for these cases. This figure shows that the resistance coefficient for Case I1 is considerably larger than those two cases. In addition, the coefficient for this case reaches its peak value at $Fr_s \approx 1.5$ and then decrease rapidly. This phenomenon is not evident in the other two cases.

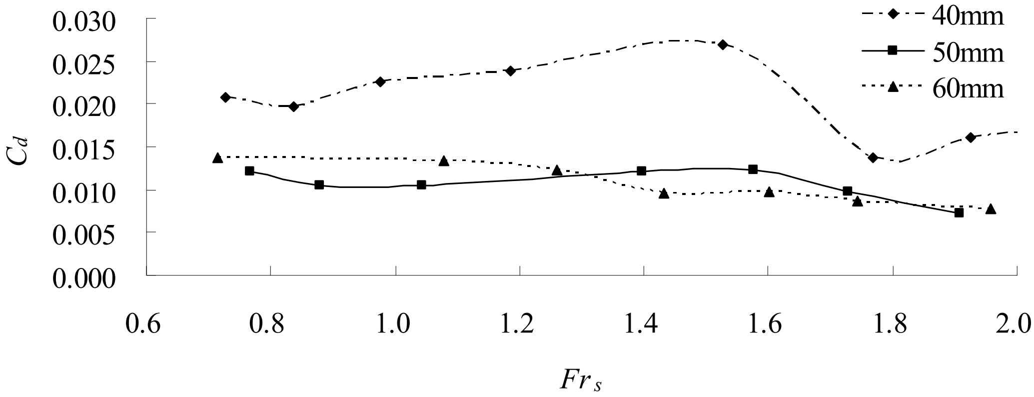

Fig.4.11 Resistance coefficients in Case I1, Case I2 and Case I3 (initial attack angle of the hydrofoil: 0°)

The resistance of the GHC consists of the resistance on the main hull and on the hydrofoil. The resistance on the main hull largely depends on the trim angle and wetted area but the resistance on the foil is affected by its submerged depth or by the free surface in other words. The closer the hydrofoil is to the free surface, the larger the wave induced by the foil should be and therefore the larger resistance on it. This may partially explain the phenomenon observed in that above figures where the large submerged depths correspond to smaller resistance. However, there are other factors affecting the properties and the characteristics of the submerged depth effect may exhibit different features from what are seen here if other parameters are changed. This is demonstrated in the following figures.

Considering Case I4, Case I5 and Case I6, the difference of these three cases from the previous three cases is due to the initial attack angle of the hydrofoil, which is -2° here rather than 0°. Fig.4.12 and Fig.4.13 present the trim angles and resistance coefficients for these cases.

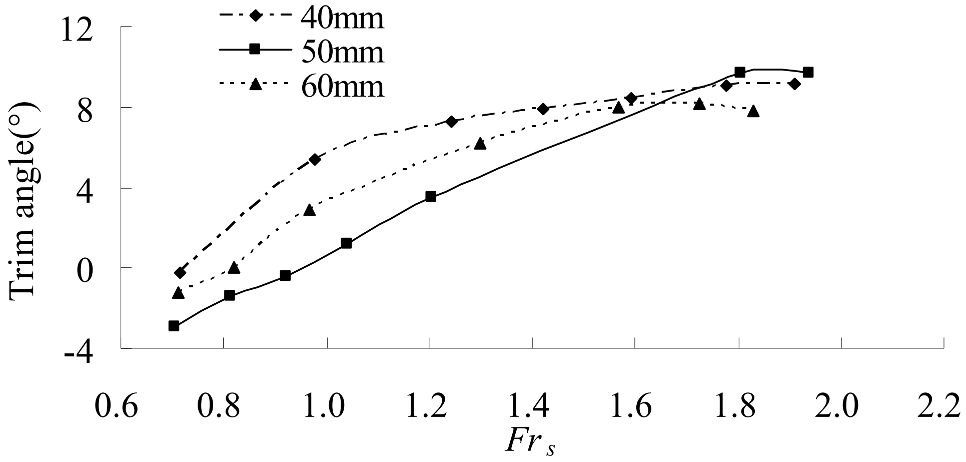

Fig.4.12 Trim angles in Case I4, Case I5 and Case I6 (initial attack angle of the hydrofoil: -2°)

Fig. 4.12 shows that the largest trim angle occurs to the submerged depth of 40mm when Fr_s < 1.7. This is different from that shown in Fig. 4.10 where the deeper submerged depth, i.e. 60mm, results in the largest trim angle when Fr_s < 1.7. In addition, it can also be found that when the submerged depth is 50mm, the corresponding trim angle is the smallest if Fr_s < 1.7. When $Fr_s \approx 1.7$, the trim angles for all the three cases are close to 8°. Looking at Fig. 4.13, we see that the variations of the resistance coefficients are more complex than those in Fig. 4.11. There is no case in which the resistance coefficient is always larger than others in the whole range of Froude number tested. Nevertheless, the coefficient for Case I4 (submerged depth =40mm) is smaller than those in other two cases when Fr_s > 1.7. This is opposite to what Fig. 4.11 shows, where the resistance coefficient for the submerged depth of 40mm is significantly larger. This complexity indicates that further research is required to fully understand the hydrodynamics of the GHC.

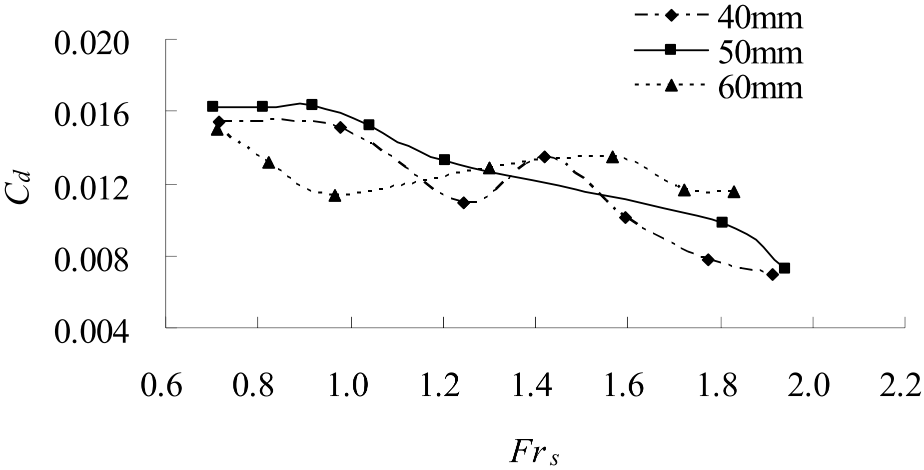

Fig.4.13 Resistance coefficients in Case I4, Case I5 and Case I6 (initial attack angle of the hydrofoil: -2°)

4.3.3 Effect Of The Initial Attack Angles Of The Hydrofoil

To further examine the effect of the initial attack angle of the hydrofoil, the data for Case I2 and Case I5 are compared in this subsection. Both cases have the same submerged depth of 50mm but different initial attack angles of the hydrofoil.

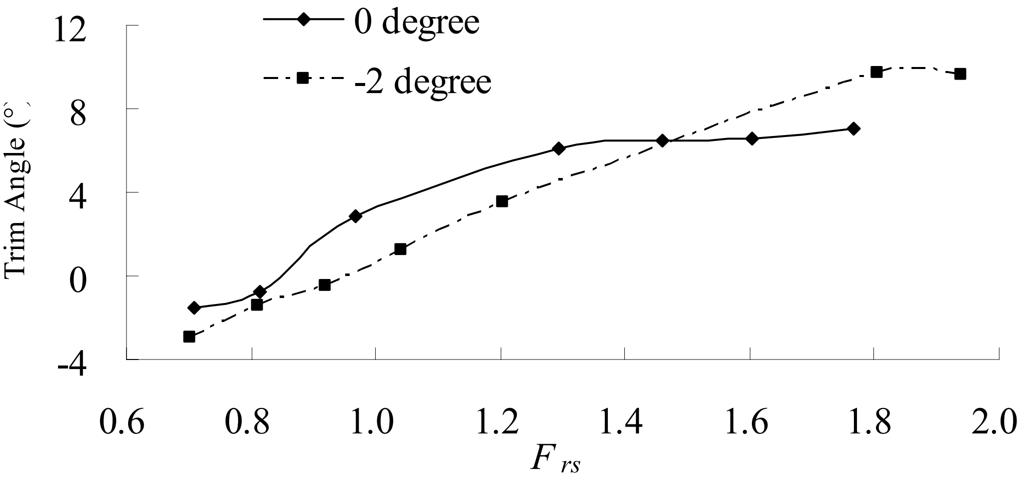

Fig.4.14 Comparison of trim angles for Case I2 and Case I5 (submerged depth of the hydrofoil: 50mm)

Fig.4.14 depicts the comparison of the trim angles for the two cases. This figure shows that when Fr_s <1.5 (Point A in the figure), a initial attack angle (0°) leads to relatively larger trim angle but when $Fr_s > 1.5$, it is opposite. On the other hand, the resistance coefficient for the initial attack angle of 0°, presented in Fig. 4.15, is smaller at the both ends than that for the initial attack angle of -2° but reaches a maximum value near $Fr_s = 1.5$ while there is not a maximum value for the latter case. This observation can only indicate that the hydrodynamic characteristics of the GHC is sensitive to the initial attack angle of the hydrofoil. More work is required to draw a general conclusion.

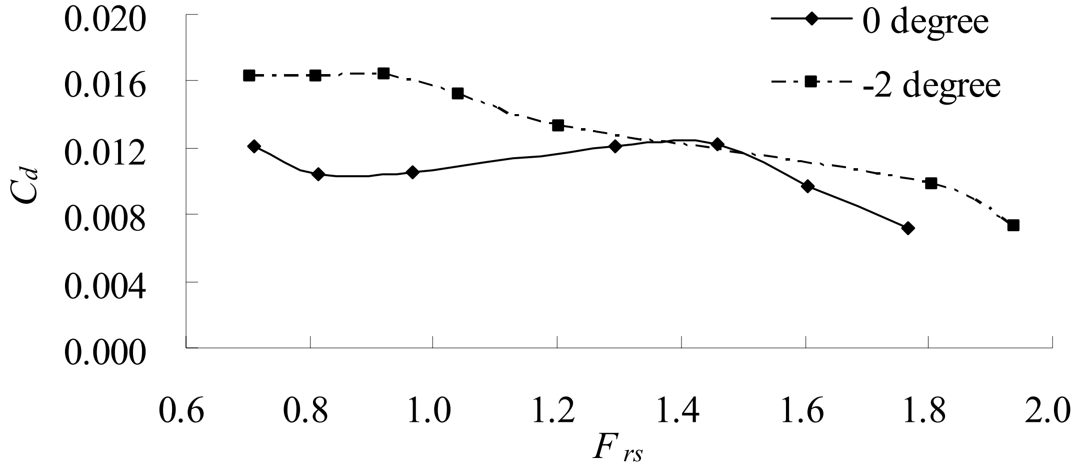

Fig.4.15 Comparison of the resistance coefficients for Case I2 and Case I5 (submerged depth of the hydrofoil: 50mm)

4.3.4 Effect of the Hydrofoil

As discussed in the Introduction, our previous studies have shown superiority of the GHC over the planing craft. In this section, it will be further discussed from the point of view of hydrodynamic properties. For this purpose, another experiment similar to those shown in Figs. 4.10-4.15 is carried out. In the experiment, the hydrofoil is removed and thus the model becomes a traditional planing craft (but its initial trim angle is set to be 1 degree, different from the GHC, for the planing craft to gain a final trim angle in a relatively shorter running distance). For the purpose of comparison, Case I2 for the GHC with the submerged depth of 50mm and the initial attack angle of hydrofoil 0° is considered here. In addition, to study the properties of the craft at corresponding speeds, the Froude number based on the initial wetted length is employed.

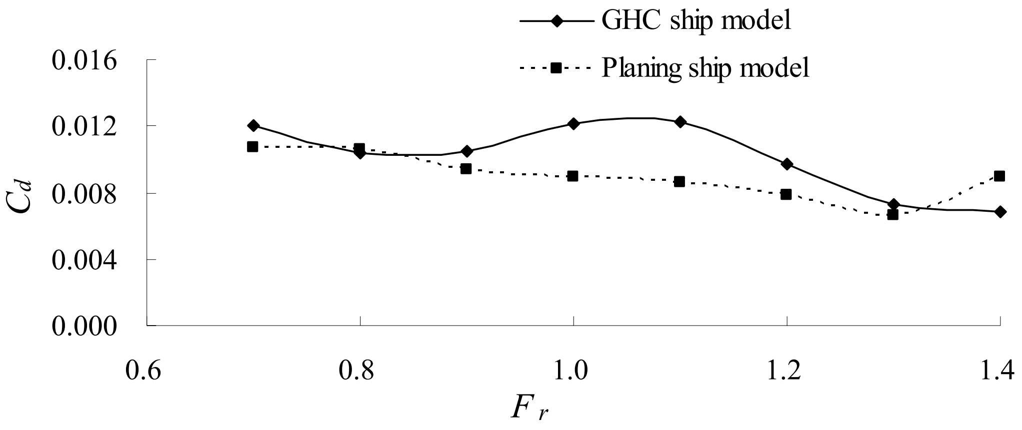

Fig.4.16. Comparison between the resistance coefficients of the GHC in Case I2 and the planing craft

Fig. 4.16 shows the comparison between the resistance coefficients of the GHC model and the planing craft model. An important feature can be found from this figure, that is, when *Fr* >1.3 the resistance coefficient of the GHC is smaller than that of the planing craft. In other words, at a high speed, the GHC has a better performance for a given power or it requires less power to achieve the same speed.

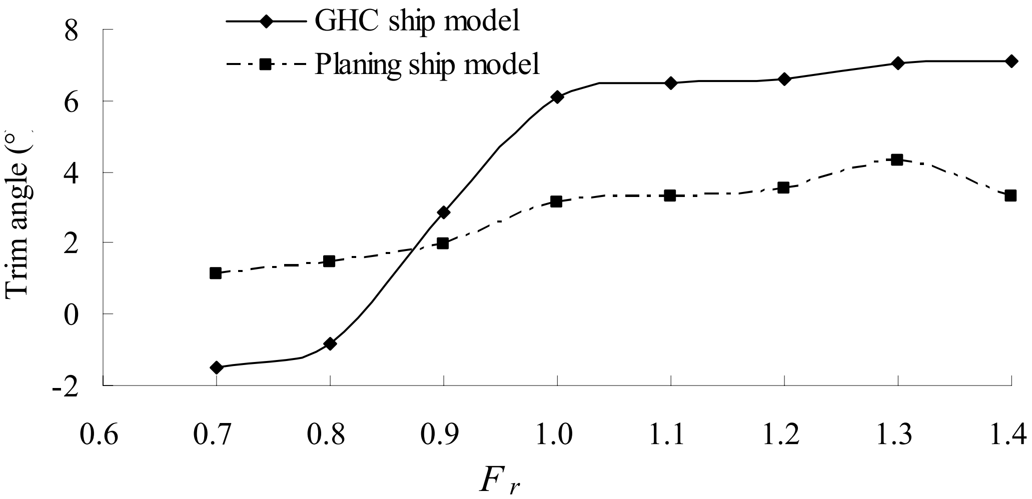

Fig.4.17 Comparison between trim angles of the GHC and the planing craft

Fig. 4.17 shows the comparison of the trim angles for the same cases in Fig. 4.16. It can be seen that the trim angle for the GHC increases rapidly until *Fr* =1 and when *Fr*>1, its trim angle remains constant. On the other hand, the trim angle of the planing craft increases in the range of *Fr*<1.3 but decreases after that value with the increase of *Fr*. This implies that the trim angle may go up or down when the velocity changes even due to small increments during real operations. This is consistent with the study by Zhou (2003), which revealed a serious pounding problem of the planing craft. In contrast, the trim angle of the GHC does not vary significantly in a large range of the Froude number as mentioned above and so the serious pounding problem may not appear to the GHC.

According to the discussions above on the two figures, it can be concluded that the GHC may be superior to the planing craft in two aspects: (1) being subjected to relative smaller resistance and (2) unlikely suffering from the serious pounding problem as long as the Froude number is large enough. This is the reason why the GHC was developed. Whether the GHC has a better performance than the planing craft depends on the design and choice of parameters. Nevertheless, this comparison demonstrates that as long as the parameters for the GHC are appropriate, its performance can be superior to the planing craft.

All the results in this chapter have been published by Chen et al. (2011).

5. IMPLEMENTATION OF CFD STUDYING HYDRODYNAMIC FEATURE OF HIGH-SPEED CRAFT

As indicated before, the FLUENT will be applied to numerically investigate and analyze the hydrodynamic behaviour of the GHC. The details of this software can be found in http://www.fluent.com/, only a brief introduction is given in this chapter. This includes the generation of computational mesh, governing equations and corresponding boundary conditions, free surface treatments and turbulence models. Based on the numerical tests, a guideline of using FLUENT to study hydrodynamic features of high-speed crafts, the implementations of outer boundary, mesh generation and turbulent models, will be proposed.

5.1. Introduction

FLUENT is one of the most popular commercial CFD (Computational Fluid Dynamics) software which has been developed by Fluent Inc. using C program since 1983. Now, it is commonly used to simulate and analyze fluid flows and heat transfer problems in complex geometric regions. The state-of-the-art CFD technologies including in FLUENT allows users to simulate many physical phenomena which may occur in practice. To do this, users need to select suitable mathematical models/governing equations, as well as relevant boundary conditions and other required parameters, for different physical problems, such as:

- Incompressible fluid flows;
- Single-phase multi-component flows;
- Flows with heat transfer and compressibility;
- Multi-phase flows;
- Other possibilities of simulation of fluid flows, such as non-newtonian fluid flows, flows through porous medium, etc.

Apart from the powerful capability in dealing with different flow problems, another feature of FLUENT is easy-to-use. The internal pre-process modules, including defining the computational domain, generating the mesh and so forth, allow users to discretize complex computational domains into high-quality meshes which ensure sufficiently accurate simulation. On the other hand, the post-process modules provide many usefully and convenient tools for the purpose of analyzing and viewing the results graphically, such as grids, contours, profiles, vectors and pathlines.

Furthermore, FLUENT is designed to run in different operation systems (such as Unix and Windows) and its integrated user-defined functions (UDFs) significantly enhances its capabilities to treat different complicated flow problems.

5.2 Basic theories and the implementation of the FLUENT to model high-speed

FLUENT solver involves a lot of concepts and numerical treatment methods of fluid mechanics. Here only the basic theories and methods that will be used in this study are introduced.

In the FLUENT modelling, the compressible viscid flow is considered. The continuity equation and the momentum equation are, respectively, given by

$$\frac{\partial \rho}{\partial t}+\frac{\partial}{\partial x_i}(\rho u_i)=0 \qquad (5.1)$$

$$\frac{\partial}{\partial t}(\rho u_i)+\frac{\partial}{\partial x_j}(\rho u_i u_j)=-\frac{\partial p}{\partial x_i}+\frac{\partial \tau_{ij}}{\partial x_j}+\rho g_i+F_i \qquad (5.2)$$

Where ρ is the density; u is the velocity; p is the pressure; ρg_i and F_i are the gravitational body force and external body forces, respectively; τ_{ij} is the stress tensor, which is given by

$$\tau_{ij}=\left[\mu\left(\frac{\partial u_i}{\partial x_j}+\frac{\partial u_j}{\partial x_i}\right)\right]-\frac{2}{3}\mu\frac{\partial u_l}{\partial x_l}\delta_{ij} \qquad (5.3)$$

where μ is the molecular viscosity. The subscripts i and j in Eqs (5.1)-(5.3) denote the mode of the motions and their values equals to 1, 2 and 3, corresponding to x-,y- and z-direction.

Turbulent flows are characterized by fluctuating velocity fields. Since these fluctuations can be of small scale and high frequency, it is too computationally expensive to directly simulate them in practical engineering calculations. In the FLUENT, Reynolds-averaged Navier-Stokes (RANS) equations are used. In the RANS models, the momentum equation reads

$$\frac{\partial}{\partial t}(\rho u_i)+\frac{\partial}{\partial x_j}(\rho u_i u_j)=-\frac{\partial p}{\partial x_i}+\frac{\partial}{\partial x_j}\left[\mu\left(\frac{\partial u_i}{\partial u_j}+\frac{\partial u_j}{\partial u_i}-\frac{2}{3}\delta_{ij}\frac{\partial u_l}{\partial x_l}\right)\right]+\frac{\partial}{\partial x_j}\left(-\rho\overline{u_i' u_j'}\right) \qquad (5.4)$$

Where $\overline{u_i}$ and $u_i^{'}$ are the mean and fluctuating velocity components ($i = 1,2,3$). In Eq. (5.4) the velocities and other solution variables corresponds to ensemble-averaged (or time-averaged) values, not the instantaneous values in Eq. (5.2). Eq. (5.4) has the similar general form to the instantaneous Navier-Stokes equations (Eq. 5.2). The additional term is the Reynolds stress term $-\rho\overline{u_i^{'}u_j^{'}}$ which represents the effects of turbulence. Many turbulence models have been developed and are available in the public domain. Detailed review of the turbulence models can be found in Kochevsky and Nenya (2003).

By using the FLUENT, the procedure to study hydrodynamic features of high-speed crafts is summarised in Fig. 5.1.

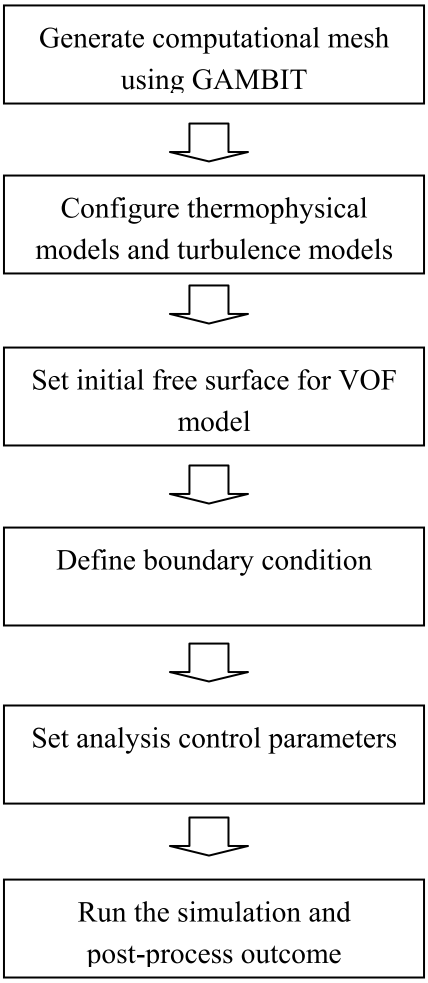

Fig.5.1 The flow chart describing the procedure of FLUENT simulation

5.3. Turbulence models

FLUENT provides the following choices for turbulence models:

- Spalart-Allmaras model
- k-ε models
    - Standard k-ε model
    - Renormalization-group (RNG) k-ε model
    - Realizable k-ε model
- k-ω models
    - Standard k-ω model
    - Shear-stress transport (SST) k-ω model
- v^2-f model
- Reynolds stress model (RSM)
- Detached eddy simulation (DES) model
- Large eddy simulation (LES) model

The details of these models will not be given here, readers may be referred to the FLUENT instructions or corresponding papers by Wang (2007).

To investigate the effect of turbulence models on the hydrodynamics in the case with free surface, the hydrofoil NACA4412 was chosen. The model and the computation domain are shown in Fig.5.2. Considering the calculation precision and computational efficiency, the computational domain extends 7.0 chord downstream, 3.0 chord upstream, and fixed submergence depth is 1.0 chord; we defined $F_c = U/\sqrt{gc}$. The non-dimensional total resistance, frictional resistance coefficient and pressure coefficient are defined as:

$$C_R = \frac{R_T}{0.5\rho U^2 C}, \tag{5.5}$$

$$C_f = \frac{R_v}{0.5\rho U^2 C}, \tag{5.6}$$

$$C_p = \frac{R_p}{0.5\rho U^2 C} \tag{5.7}$$

where R_T , R_v and R_p are the total resistance, viscous resistance and pressure resistance respectively. U is the incoming flow speed, c is the chord length and g is the acceleration of gravity.

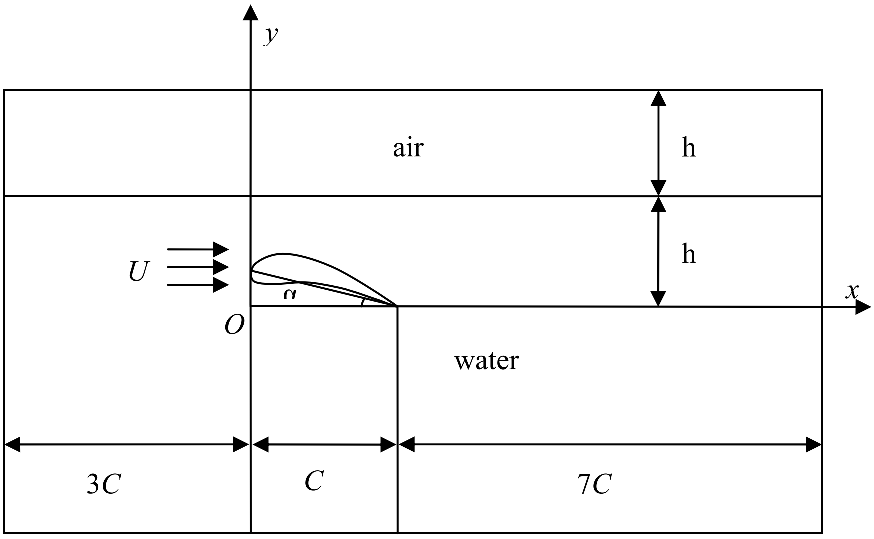

Fig.5.2 Definition of coordinate system and notation

In the investigation, *Fc*=1.0. The models to be studied will be one equation Spalart-Allmaras model, two equations standard $k-\varepsilon$ model, RNG $k-\varepsilon$ model, Realizable $k-\varepsilon$ model, standard $k-\omega$ model and SST $k-\omega$ model. S-A one equation model, applied in aeronautics field widely, was rarely used in ship hydrodynamics previously. At present some researchers use this model because it is simple and it is not very sensitive to numerical errors (Sakir Bal, 1999). Actually various $k-\varepsilon$ turbulence models have been used in ship hydrodynamics because they are powerful, economic and good accuracy. $k-\omega$ turbulence model is a relatively new model and it developed very quickly in ship hydrodynamics. At present it is used widely and according to the literatures, the numerical results obtained by $k-\omega$ model are better (Jin Wei, 2009) than others.

Table.5.1 Comparison of resistance coefficients obtained by 8 different turbulence models (*Fc*=1.0)

Turbulence model	S-A model	Standard $k-\varepsilon$	RNG $k-\varepsilon$	Realizable $k-\varepsilon$	Standard $k-\omega$	SST $k-\omega$	RSM	LES
Coefficient of total resistance	0.0624	0.0656	0.0655	0.0643	0.0623	0.0639	0.0661	0.0630
Coefficient of friction	0.0080	0.0114	0.0109	0.0100	0.0090	0.0095	0.0116	0.0092
Coefficient of pressure resistance	0.0544	0.0542	0.0546	0.0542	0.0533	0.0544	0.0545	0.0538

The table 5.1 shows the comparison of resistance coefficients in cases with different turbulence models for the above case. The experimental result of total resistance coefficient is 0.064 (Sakir Bal, 1999). From table 5.1 we can see that the resistance coefficient obtained by SST $k-\omega$ model is closest to the experimental result, consistent with investigations in literatures concluding that SST $k-\omega$ model is more appropriate to study the viscous flow with free surface. The resistance coefficient predicted by S-A model is much smaller than the experimental result. Standard $k-\varepsilon$ model, RNG $k-\varepsilon$ model and realizable $k-\varepsilon$ model are better than the S-A model. Meanwhile, the coefficients of pressure resistance of all turbulence models are very close in table 5.1, the effect of turbulence model on pressure resistance can be ignored. Thus, SST $k-\omega$ model is adopted for other case in this thesis.

5.4 Generation of computational mesh

FLUENT provides a software package called GAMBIT which is designed to analyze and generate the mesh for the CFD and other scientific applications. GAMBIT is visualized software supported by a graphical user interface (GUI) that simplifies the basic steps, such as data input, mesh building and generating, zone types assigning. GAMBIT can generate both structured and unstructured grids. For unstructured grids, the nodes are distributed in the domain in a random way, according to the specified density law of node distribution. It is easy to fit the boundaries and so to satisfy the requirement of complicated-geometry domain. However, the discrete counterparts of the flow equations in such a grid are cumbersome. From this point, it would be better to use structured meshes. To do so, one may first split the computational domain into several blocks in order to fit the complicated boundary surfaces in some cases. In each block, the structured grid is generated.

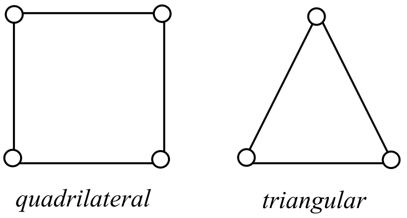

Fig.5.3 Typical shapes of 2D grid cells

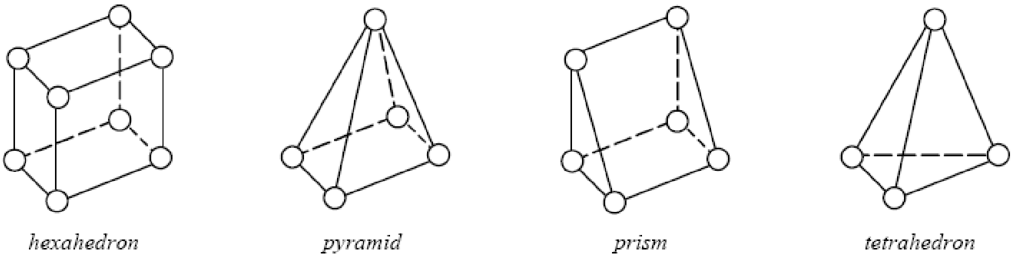

Fig.5.4 Typical shapes of 3D grid cells

On the other hand, the GAMBIT can generate different types of cells. In 2D cases, quadrilateral (Fig 5.3a) and triangular cells (Fig.5.3.b) are acceptable. While in 3D cases, it can generate hexahedral, tetrahedral, pyramid, prism and tetrahedron cells (Fig.5.4). Both single-block and multi-block meshes, as well as hybrid meshes containing different types of cells are acceptable. FLUENT also accepts grids with hanging nodes (i.e., nodes on edges/faces are not the vertices of all the cells sharing those edges/faces) and grids with non-conformal boundaries (i.e., grids with multiple sub-domains in which the grid node locations at the internal sub-domain boundaries are not identical).

In order to improve the accuracy of the results, the computational mesh should be fine enough to resolve the physical effects occurring inside the domain. For example, the nodes should distribute closer to each other in the area where the spatial derivatives of physical parameters is larger, particularly near the moving boundaries such as free surfaces and hull surfaces. Furthermore, excessively stretched or skewed cells should be avoided when generating the grid because the numerical error mainly appears in those cells and therefore affect the convergence properties of the numerical models.

The selection of the mesh types depends on the complexity of the problem solved and the numerical method used. Normally, if the grid nodes move towards to the flow direction the calculation result is better. Here we assume that the physical quantities are defined on the grid nodes. For the complex flow the hexahedral meshes are better suited to the numerical processors than tetrahedral meshes, such as the flow around the hull. At the present stage, the common mesh types are the following:

Single-block structured mesh. This is the simplest computing grid and was used commonly, the grid is generated through algebraic functions and solving differential equations. The program of single-block structured mesh is easy and requires less computer memory because of the consecutive number of the grid. If we use this mesh type the computational space need to be a rectangle or cuboid, or at least has a rectangular boundary with a regular or rectangular grid. In case of very complex shape (such as ships with appendages), single-block structured mesh may not be suitable. In addition, the change of grid resolution in a particular area (such as near the hull) will lead to change the grid resolution in other unnecessary areas causing that the skewness is too big and thus affect the accuracy of the simulation.

Grid may also be severely deformed in the region with sudden changes in shape. At present, the single-block structured mesh is used to study the ship with relatively simple shape.

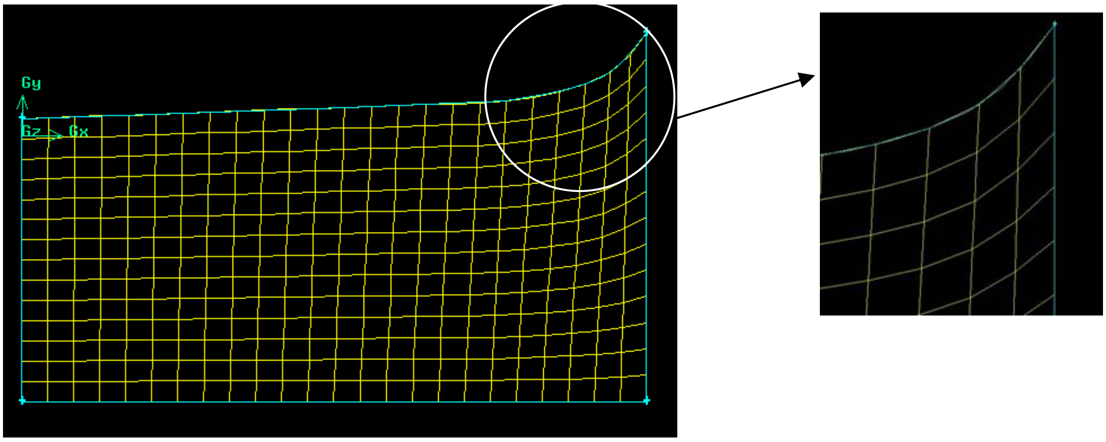

Fig.5.5 Single-blocked structured mesh

Multi-block structured mesh. It is difficult to fit complex domains with one mapping from a rectangular computational domain without generating excessively skewed grids. To get round this problem, the domain may be split up into blocks and each block is gridded, with some continuity requirements at the block interfaces. This is multi-block mesh. It is a compromise of single-block structured and unstructured mesh. The grid generation process splits into two parts, the decomposition of the physical domain into blocks and the gridding of each block. The advantages of multi-block structured mesh include gridding easily and fitting complex domains. More and more researchers use this kind of mesh in the CFD studies related to ships. In multi-blocked structured meshes, the cells on the interface may or may not match with each other, shown in Fig.5.6. The former is the traditional multi-blocked structured mesh. The latter allows specifying different grid density in different blocks, thus has better adaptive property and, therefore, more suitable for the problems with the interaction between ship hull and appendages.

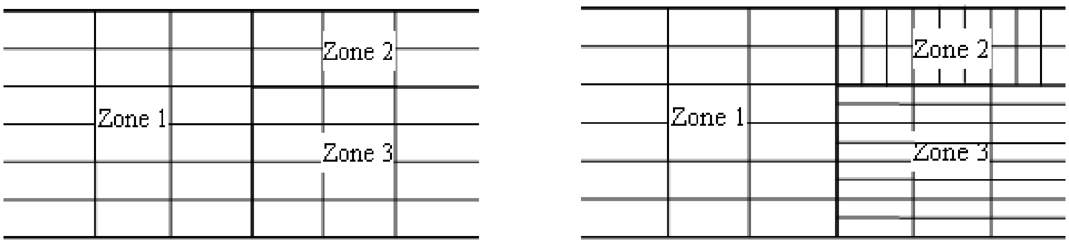

(a) Boundary matching (b) Boundary mismatching

Fig.5.6 Multi-block structured mesh (a) boundary matching and (b) boundary mismatching

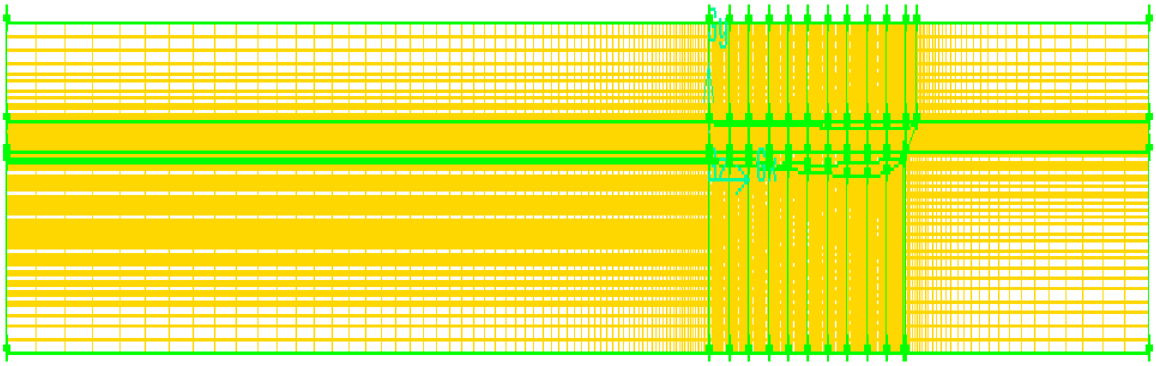

Fig.5.7 3D multi-block structured mesh for the domain of ship flow (there are 67 blocks)

However, there are also disadvantages with fully boundary-fitted multi-block grids as discussed below.

- The blocking requires a great deal of user effort, which maybe one man-month for complex configurations. During the design process of a product, several different physical configurations can be considered and each may need a time-consuming blocking. This obviously slows down the overall design process;
- Changes of geometry in one block lead to changes to many other blocks;
- Change in the grid point distribution in one block, e.g. adding points near a sharp feature on an object, generally causes the changes in other blocks to maintain the grid point continuity;
- Requirement of grid point continuity makes it difficult to increase resolution in one block without (unnecessarily) increasing the resolution in other blocks.

The most commonly used method of structured grid generation is multi-block with transfinite interpolate or elliptic generation in the blocks. The regularity of structured grids allows fast solvers to be used, vectorisation/parallelisation is easy and cache use is efficient. There is a large user effort in constructing the multi-block decomposition but the tendency for complex domain configurations now moves to the use of unstructured meshes, which can be automatically generated, even though the solvers are slower.

Unstructured mesh. Unstructured meshes were developed mainly for the finite element method. It is the most adaptable grid which conforms to the boundary of the domain. Unstructured mesh eliminates the structural limitation of nodes and overcome possible problems by controlling the distributions of nodes/elements in structured mesh generation.

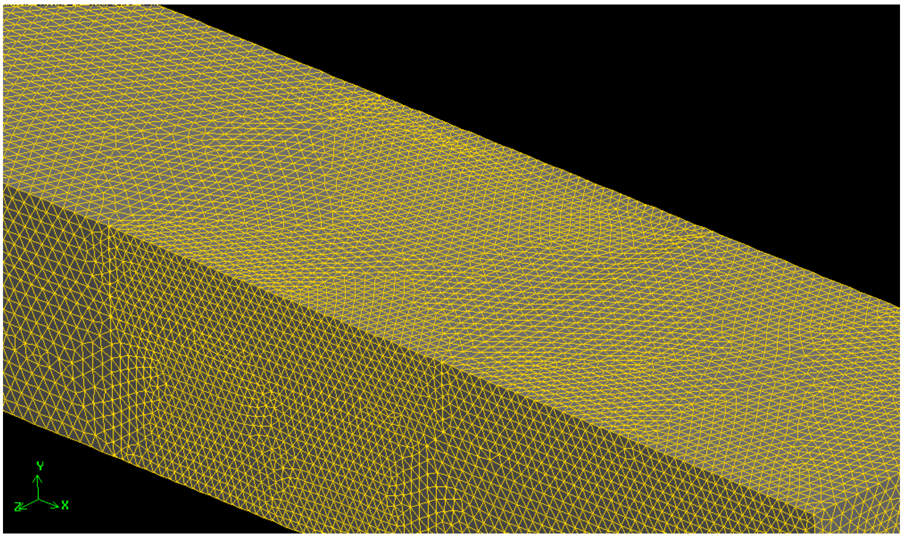

Fig.5.8 Flow domain meshed by unstructured mesh

However, the unstructured may be not suitable for dealing with viscous flows, partially due to the low generation procedure and limitations in cell shapes. Based on the decomposition/mapping technologies and the Delaunay triangulation method, only triangular mesh (2D) or tetrahedral (3D) mesh can be generated. Compared to rectangular/cubic structured mesh, the triangular/tetrahedral unstructured mesh discretizing the same computational domain has much more number of nodes and, therefore, requires more computer resources and computational time. In CFD focused on ships the unstructured mesh is rarely used currently but is expected to be applied by more and more researchers as the development of the computer hardware.

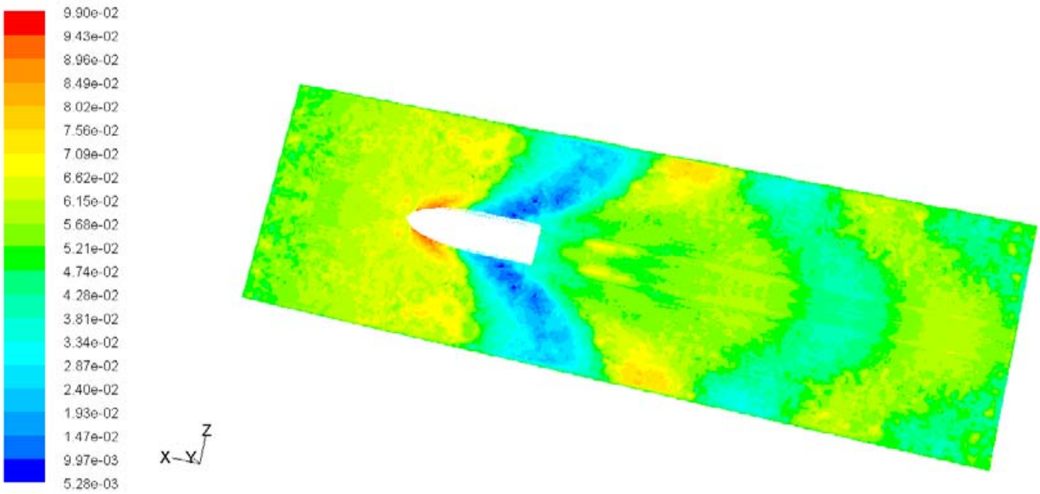

(a) The wave elevation of planing craft at *Fr*=0.5 (unstructured mesh)

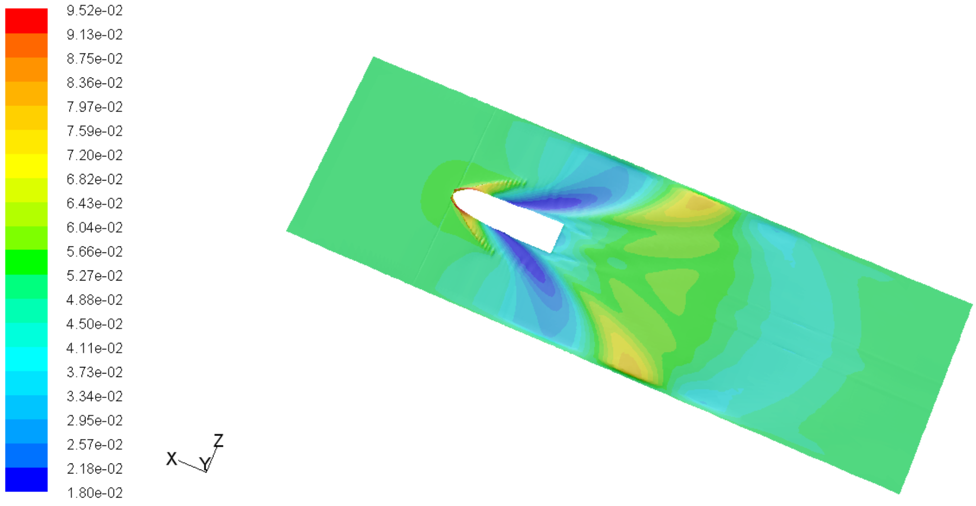

(b) The wave elevation of planing craft at *Fr*=0.5 (structured mesh)

Fig.5.9 The wave elevation of planing craft at *Fr*=0.5

Another problem with the unstructured mesh is that numerical saw-tooth may be found because the size, aspect ratio, quality as well as the connectivity property of neighbouring cells may be not continuous, as demonstrated in Fig. 5.9, where the wave elevation of a planing craft at *Fr*=0.5, in cases with unstructured mesh and multi-block structured mesh. In the results with unstructured mesh (Fig. 5.9a), the free surface elevation is not smooth but with significant saw-tooth in space. However, the structured mesh leads to smoother results without visual spatial oscillation. Thus, multi-block structured mesh is the most commonly used mesh, except for cases with relatively complicated structure geometry, such as GHC. As discussed before, for complicated fluid domain, the structured mesh is not easy to be generated. In such cases, a hybrid mesh combining structured and unstructured mesh is used.

Hybrid mesh. As discussed above, both the structured and unstructured meshes have advantages and disadvantages. In order to take their advantages and avoid their disadvantages, the hybrid mesh with unstructured or structured mesh at different blocks, is generally employed in order to well fit the boundaries, improve generation efficiencies and reduce the numbers of cells/nodes in discretisation.

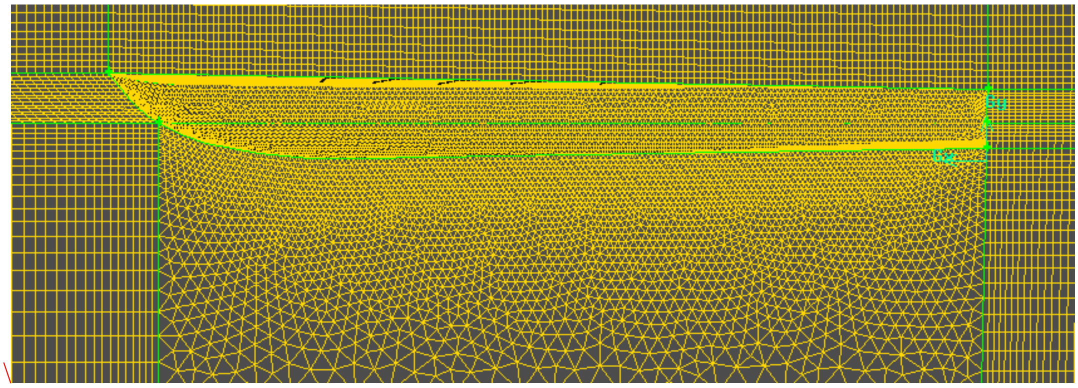

Fig.5.10 Computational grid near planing craft

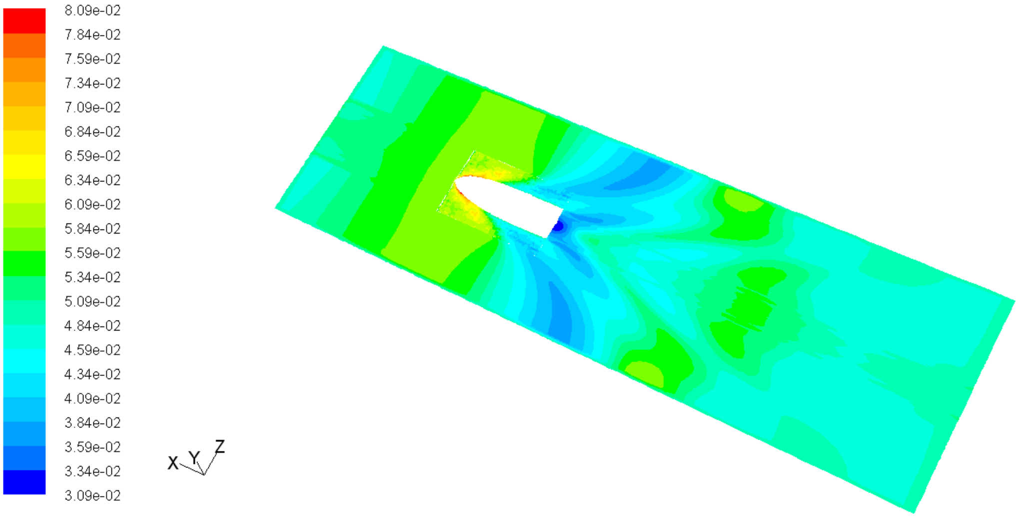

(a) The wave elevation at *Fr*=0.7

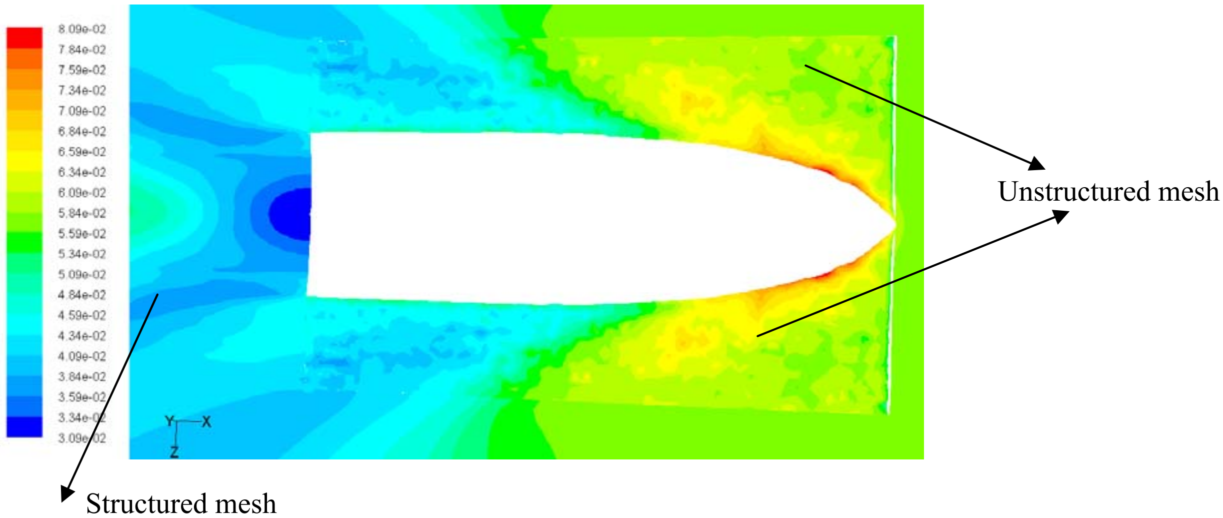

(b)The wave elevation near the craft at *Fr*=0.7

Fig.5.11 The wave elevation at Fr=0.7

An example is shown in Fig.5.10. The results corresponding to the wave elevations around a planning craft are shown in Fig. 5.11, in which the wave elevation seems to be smooth, similar to that by structured mesh, and no visual saw-teeth are found in space.

5.5. Boundary conditions

Generally, the computation domain for ship travelling in free surface is hexahedron including water and air, as shown in Fig.5.12. Only half domain has been simulated because the ship structure is symmetrical. The boundary include: inlet, outlet, ship, and symmetry, one side of computation domain, top and bottom.

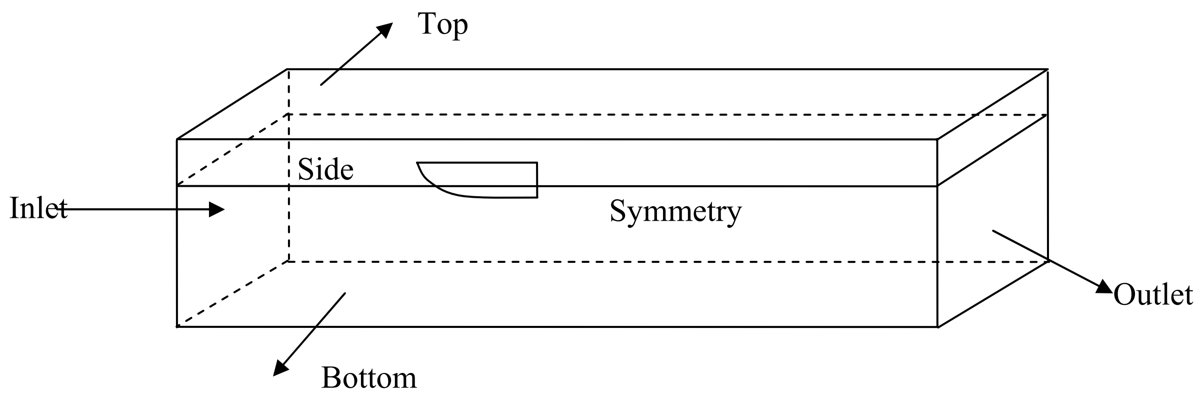

Fig.5.12 Computation domain and boundary conditions of a free-surface ship

Inlet: The boundary inlet in this study is velocity inlet for flow simulation of free-surface ship. Velocity inlet boundary conditions are used to specify the incoming fluid velocity, together with all relevant scalar properties of the flow at the inlet boundary. The specified values at the inlet should not include the effects of any bodies inside the domain. Therefore, the inlet boundary should be located well before the body. The only parameter we need to set is the navigation speed of the ship.

Outlet: There are two kinds of outlet boundary conditions for appropriate ships travelling in free-surface flow. One is the pressure outlet boundary condition, specifying static(gauge) pressure at the outlet boundaries. In Fluent, the specified static pressure at the outlet boundaries is considered only for case where the flow is subsonic, whereas for case where the flow becomes locally supersonic, the pressure at the outlet will be replaced by values extrapolated from the flow in the interior layers instead of the specified pressure. For the cases considering in this thesis, the pressure at outlets is assigned to be proportional to the depth of the water, following $p = \rho g h$ where, ρ is the density of water, g is the acceleration of gravity and h is the depth of water. This treatment does not exactly satisfy the physical boundary conditions at the end of the tank but is justified by the fact that (1) the error due to this assumption does not significantly affect the results near the hulls if the domain size is sufficiently large; (2) the wave on such boundaries may be damped using numerical damping zone. The second outlet condition is the outflow boundary condition, which may be used in the cases where the flow velocity and pressure are not known prior to solving the flow problem. Flow exiting outflow boundary exhibits zero normal diffusive flux for all flow variables.

Ship: Wall boundary conditions are applied to the intersecting surface between the fluid and the solid regions. In viscous flows, the no-slip boundary condition is enforced on the walls by default, but a tangential velocity component in terms of the translational or rotational motion of the wall boundary may also be allowed (i,e., slip wall boundary condition). In this work, non-slip boundary condition is chosen.

Symmetry: When the fluid domain (the physical geometry of interest) as well as the physical problem, such as the expected pattern of the flow solution, is symmetrical with respected to a wall, the symmetry boundary condition is imposed on it for the purpose of reducing the size of the computational domain and so improving the computational efficiency. It is also applied to model zero-sheer slip boundaries in viscous flows.

Top, bottom and side: The same non-slip wall boundary condition is adopted for the top, bottom and side boundaries. Obviously, the top and the side walls do not physically exist. If the size of computation domain is big enough, so the effect of the top and side can be ignored. For the shallow water case, the bottom boundary represents real seabed and thus the wall boundary condition is suitable. However, for deep-water problem, the bottom may be an artificial boundary truncating the computational domain in depth. The justification of assigning wall boundary condition can also be given by the same reason as that for top and side wall. It should be noted that if the problem is symmetrical about the longitudinal axis of the ship, one may only simulate half of the computational domain with a symmetrical boundary condition on the central plane consistent with the longitudinal plane of the ship. In that case, one may also assign a wall boundary condition on the central plane which is equivalent to the symmetrical boundary condition.

5.6 Free surface flow model

Another very important phenomenon, which must be taken into account in the numerical studying of the hydrodynamic feature of the high-speed craft, e.g. GHC, is the free surface. In Chapter 4, the importance of the free surface effect (wave effect) on the resistance has been demonstrated. To consider the free surface, the Volume of Fluid (VOF) model is used in the FLUENT. In this model, an additional function *F,* which expresses the 'concentration of liquid in gas, is supplemented with the governing equations.

$$\frac{\partial(F\rho)}{\partial t}+\frac{\partial}{\partial x_j}\left(F\rho u_j\right)=0 \qquad (5.8)$$

Volume fraction F equals 1 when the volume of the cell is fully filled by fluid and 0 when it is fully filled by gas. If the cell crosses the free surface, the value of F ranges between 0 and 1. Initially, the position of the free surface should be specified. The detailed algorithm for numerical solution using this model was described in Harlow and Welch (1965) and Hirt and Nicholls (1981).

6. INVESTIGATION OF MESH DEPENDENCE AND COMPUTATION DOMAIN SIZE

When calculating the model by Fluent, the size (Δl) of cells is very important to meet a given accuracy within feasible calculation time. In order to show that the obtained solution is grid-independent, it is necessary to perform computations at several computational grids with different sizes. Thus, one can determine the value of the size at which the solution hardly changes with further increase of this value. Another important aspect of the ship viscous flow calculation is the selection of the turbulent model. Every turbulent model is based on experimental results and theoretical analysis. Therefore they are not generally applicable. Different flow field need to adopt a specific turbulent model to get better simulation results.

In this chapter, the NACA4412 hydrofoil and the Wigley hull are chosen to study the turbulent model adaptability and mesh dependence to find a more suitable turbulent model for ship flow calculation.

6.1 Case Ⅰ: NACA 4412 hydrofoil

There are three reasons for analyzing this problem. First, it is a bridge for 3-D calculations, and it is part of GHC. Second, it is much faster than the corresponding 3-D one. Furthermore, there are plenty available experiment data to compare.

6.1.1 The calculation model and boundary condition

A steady uniform flow past a fixed 2-D hydrofoil beneath the free surface of water is considered. The *oxy* cartesian coordinate system is chosen, with x is in the horizontal direction, y is positive upwards, as shown in Fig.6.1. Considering the calculation precision and computational efficiency, the computational domain extends 7.0 chords downstream, 3.0 chords upstream, and fixed submergence depth is 1.0 chord.

In Fig.6.1, U is the incoming uniform flow velocity, h is the submergence depth, C is the chord, and α is the angle of attack. In this calculation, C=1m, h=C, and α=5°.

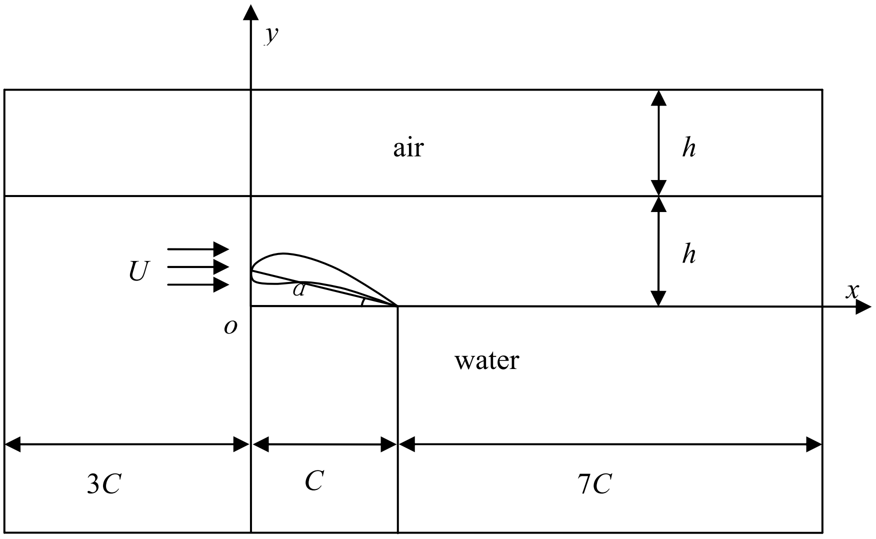

Fig.6.1 Definition of coordinate system and notation

The multi-block structured mesh was used. The calculation field is divided into twelve parts. There are 24195 nodes, 47355 faces and 23850 quadrilateral cells totally. The grid is shown in Fig.6.2 and Fig.6.3.

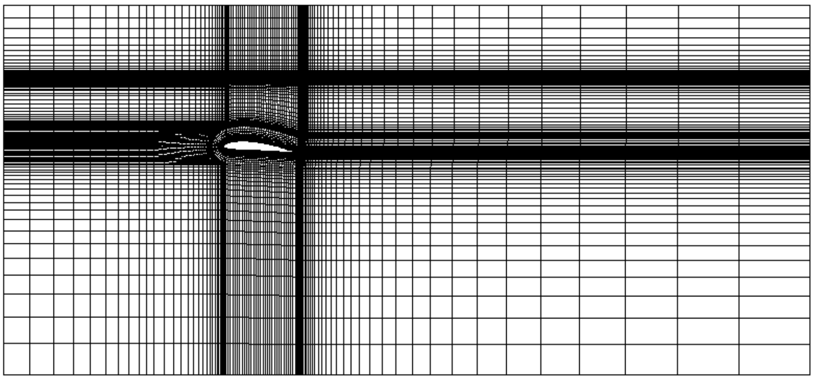

Fig.6.2 The grid of calculation field

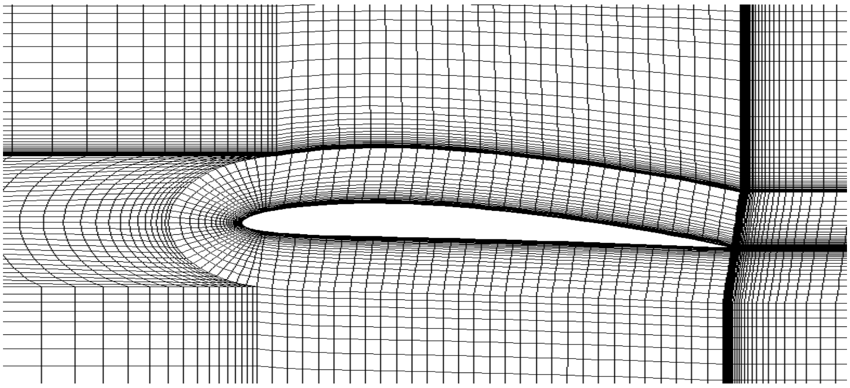

Fig.6.3 The grid around the hydrofoil

For this problem, the k-ε standard viscous model is chosen. Free surface model is the volume of fluid, and pressure-velocity coupling method is SIMPLEC. As to boundary conditions, the velocity inlet boundary condition is applied at inlet, and the pressure outlet boundary condition is applied at outlet. The boundary condition on the hydrofoil surface is the wall.

It should be noted that the outlet boundary condition may be set as outflow condition. The outflow boundary condition is valid in fully-developed flows where the diffusion flux for all flow variables in the exit direction is zero. That may happen in the region far downstream from the hydrofoil. Because the time and computer memory are limited, the calculation field can not be long to satisfy the outflow boundary condition. The reasonable results can not be obtained. Therefore, the pressure-outlet is used. The detail of the pressure-outlet boundary condition was discussed in Chapter 5.

6.1.2 Numerical results

A number of numerical tests were carried out. The results are compared with those given in Yeung and Bouger (1979). The non-dimensional total resistance coefficient, lift coefficient and pressure coefficient are defined as:

$$C_R = \frac{R_T}{0.5\rho U^2 C}, \tag{6.1}$$

$$C_L = \frac{R_L}{0.5\rho U^2 C}, \tag{6.2}$$

$$C_p = \frac{\left(p - p_{ref}\right)}{\frac{1}{2}\rho U^2} \tag{6.3}$$

where R_T is the total resistance (including pressure resistance and viscous resistance) and R_L is the lift force. p is the static pressure and p_{ref} is the reference pressure.

The criterion of convergence is very important in order to obtain reasonable results. There are no universal metrics for judging convergence. Residual definitions that are useful for one class of problem are sometimes misleading for other classes of problems. Therefore it is a good idea to judge convergence not only by examining residual levels, but also by monitoring relevant integrated quantities such as drag or heat transfer coefficient.

For most problems, the default convergence criterion in FLUENT is sufficient. This criterion requires that the scaled residuals decrease to 10^{-3} for all equations. Sometimes, however, this criterion may not be appropriate. Typical situations are listed below.

(1) If one makes a good initial guess of the flow field, the initial continuity residual may be very small leading to a large scaled residual for the continuity equation. In such situation it is useful to examine the unscaled residual and compare it with an appropriate scale, such as the mass flow rate at the inlet.

(2) For some equations, such as for turbulence quantities, a poor initial guess may result in high scale factors. In such cases, scaled residuals will start low, increase as non-linear sources build up, and eventually decrease. It is therefore good practice to judge convergence not just from the value of the residual itself, but from its behaviour. One should ensure that the residual continues to decrease (or remain low) for several iterations (say 50 or more) before concluding that the solution has converged.

In all cases in this thesis, the convergence of the results was assessed through monitoring the resistance coefficient or the lift coefficient.

In Fig.6.4, the coefficients of resistance changing with time for different Froude numbers ($Fc=U/(gc)^{0.5}$) are shown. We can see that the results are convergent to a constant as expected after sufficient long time but the process depends on the value of Froude numbers. Generally speaking, the larger the Froude number, the less the time during which the coefficients of resistance fluctuate.

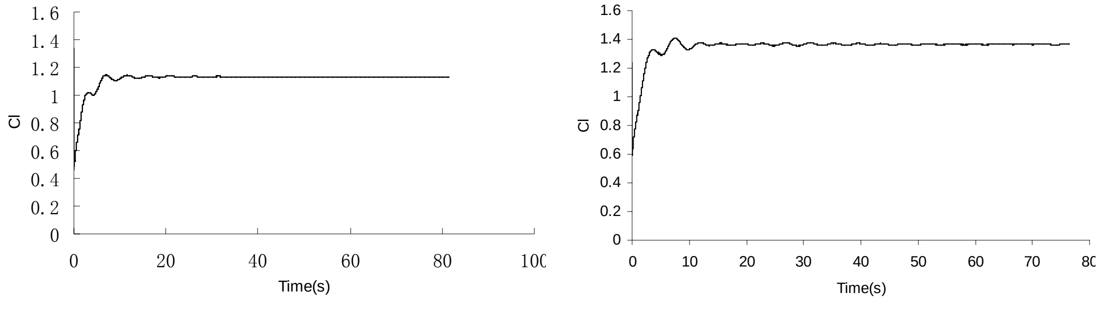

(a) Fc=0.4　　　　　(b) Fc=0.5

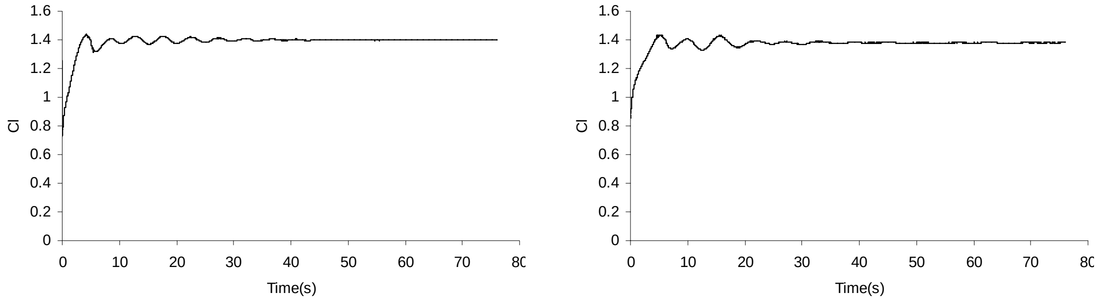

(c) *Fc*=0.6 (d) *Fc*=0.7

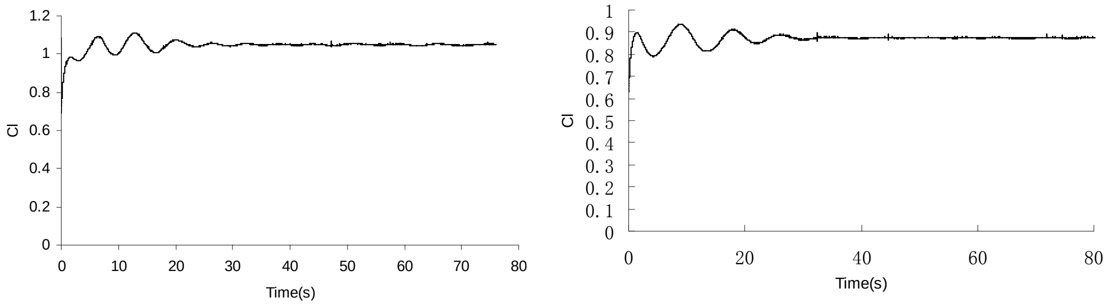

(e) *Fc*=0.8 (f) *Fc*=0.9

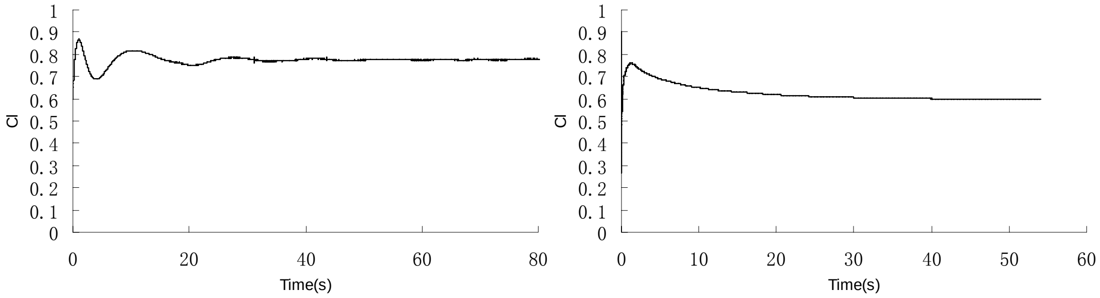

(g) *Fc*=1.0 (h) *Fc*=1.2

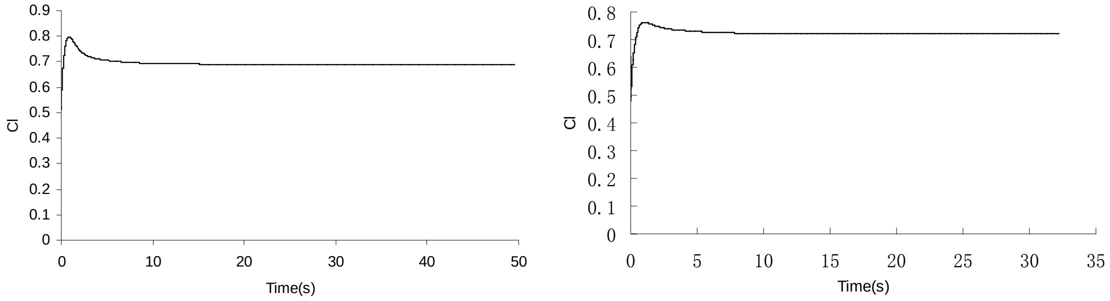

(i) *Fc*=1.4 (j) *Fc*=1.6

Fig.6.4 The coefficients of lift changing with time for different Froude numbers

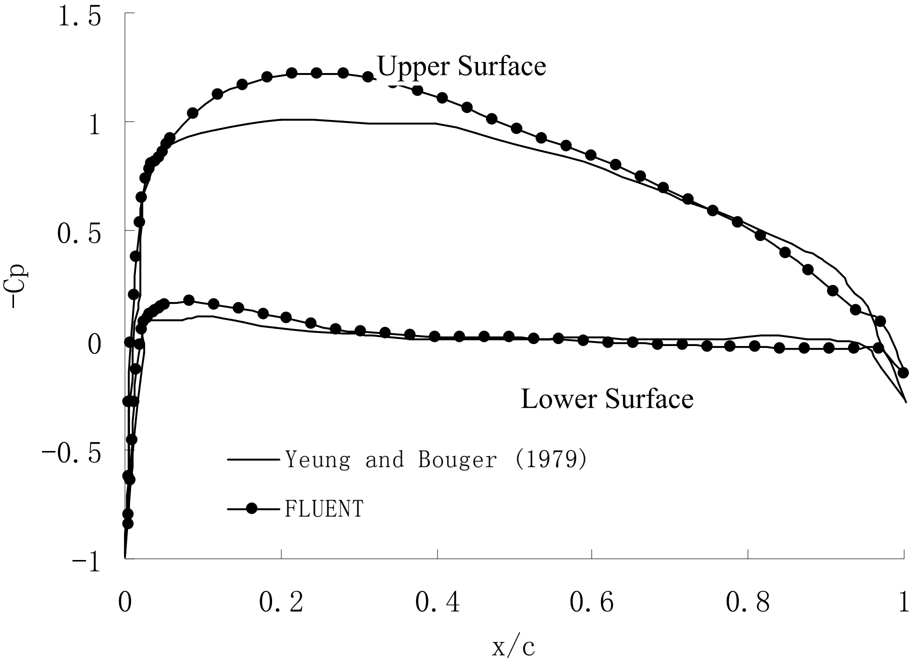

Fig.6.5 Pressure distribution on NACA4412 hydrofoil with angle of attack 5° (*Fc*=1, *h*/*c*=1)

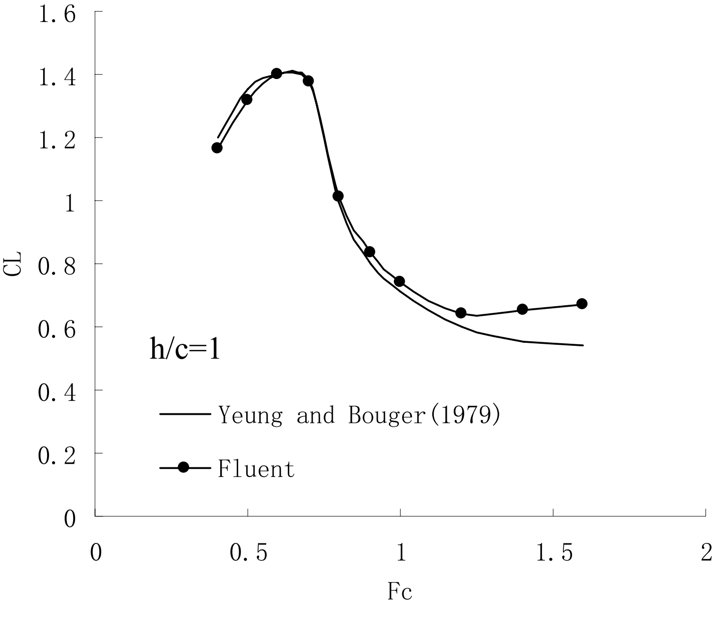

Fig. 6.6 Lift coefficient of NACA4412 hydrofoil with angle of attack 5° for increasing Froude numbers

In Fig.6.5, the calculated pressure coefficient distribution on the hydrofoil for *Fc*=1 and *h*/*c*=1 is compared with that given by Yeung and Bouger (1979). The corresponding lift and resistance coefficient values are C_L=0.742, C_R=0.062 comparing with C_L=0.756 and C_R=0.063 of Yeung and Bouger (1979). The C_p values calculated by the present method are in good agreement with those reported by Yeung and Bouger (1979), except near the leading and trailing edges. In Fig. 6.6, the effect of Froude number on lift coefficient is shown and compared with that given in Yeung and Bouger (1979).

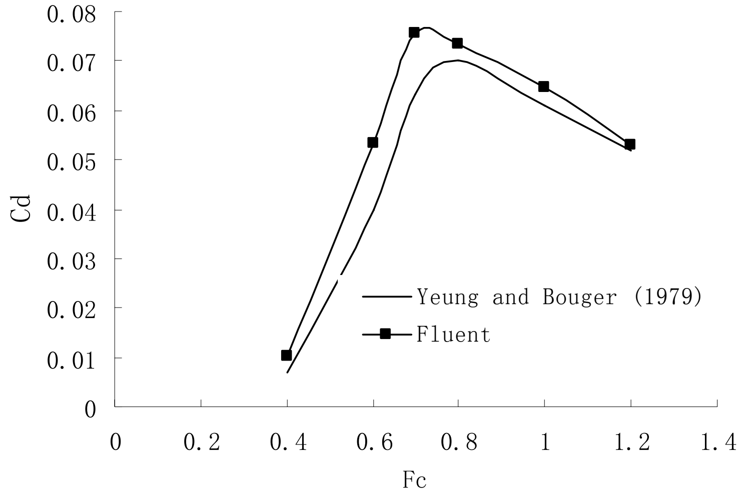

Fig.6.7 Resistance coefficient of NACA4412 hydrofoil with angle of attack 5°for increasing *Fc*

From Fig.6.7, it can be seen that the lift coefficient decreases with Froude numbers larger than 0.6 and that there is some difference between the results. Fluent takes viscosity into account. The coefficient of lift obtained by Yeung and Bouger did not include the viscous effect. This may be the reason for the difference between them.

6.2 Case Ⅱ: Wigley hull

In this section, the hydrodynamics of Wigley hull with free surface are discussed. Owing to its simple geometry and a large number of available databases for resistance and wave elevation, the Wigley hull has been widely used to validate computational methods.

6.2.1 The calculation model and boundary condition

The standard Wigley hull is of mathematical hull form with its geometric surface defined as:

$$y(x,z)=\pm\frac{B}{2}\left[1-\left(\frac{2x}{L}\right)^2\right]\left[1-\left(\frac{z}{T}\right)^2\right],$$

where *L* is the hull length, *B* the full hull beam and *T* the hull draft. For the standard Wigley hull used in this computation, the length-to-beam ratio *L*/*B* is 10 and the beam-to draft ratio *B*/*T* is 1.6.

A Cartesian coordinate system *o-xyz* fixed to the body is established, with its *y*-axis in the opposite direction of gravity, *y*=1m at the undisturbed free surface and *x*-axis in the longitudinal direction towards the stern of the ship (Fig.6.8).

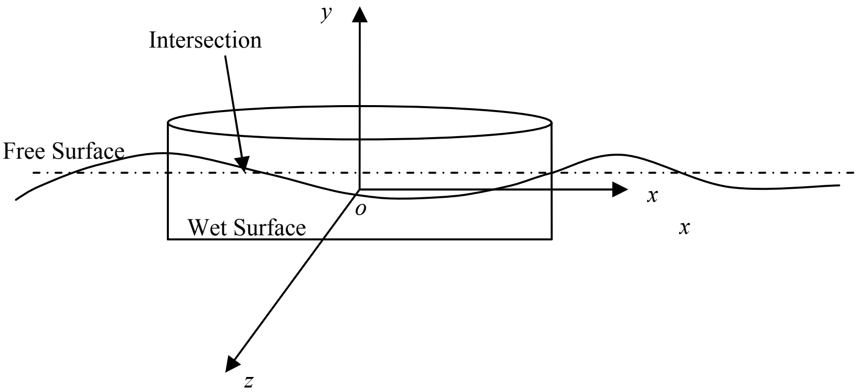

Fig.6.8 The Cartesian coordinate system *o-xyz* and notations for a ship hull moving on a free surface

The computational domain extends 4 ship length downstream, 1.5 ship lengths upstream, 1.5 ship length in the *z*-direction, 1 ship length in the positive *y*-direction and 2 ship length in the negative *y*-direction. The mesh of calculation field is shown in Fig.6.9. In this case, 9588 nodes are used on the free surface and 707 nodes on the hull wetted surface.

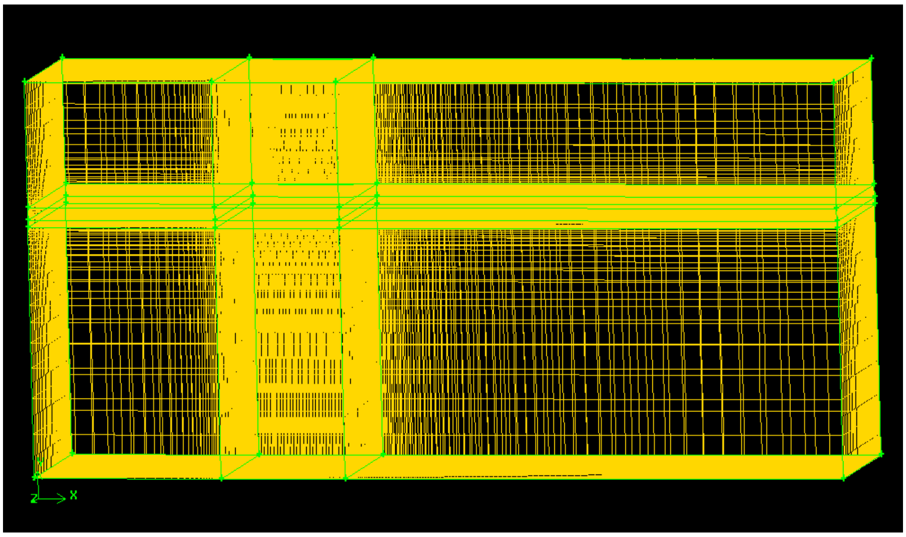

Fig.6.9 The mesh model of Wigley hull

6.2.2. Calculation model and results

To calculate the model by Fluent software, incompressible flow is assumed. The standard k-epsilon turbulence model is selected according to investigations described above. In this case, the Wigley hull is fixed with incoming velocity of fluid specified.

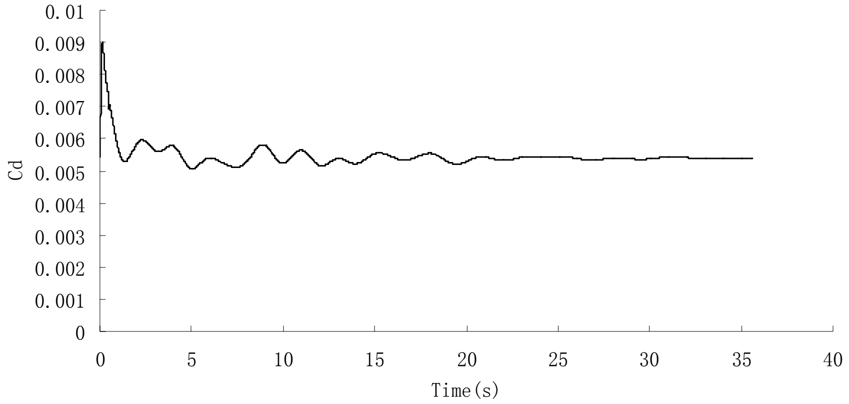

(a) *Fr*=0.25

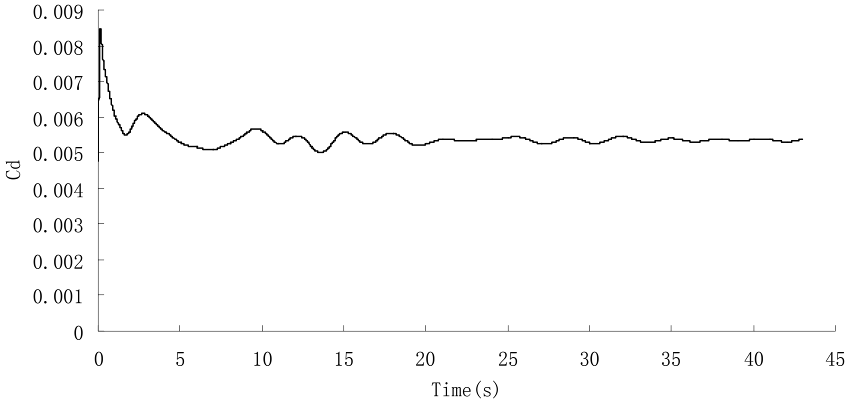

(b) *Fr*=0.289

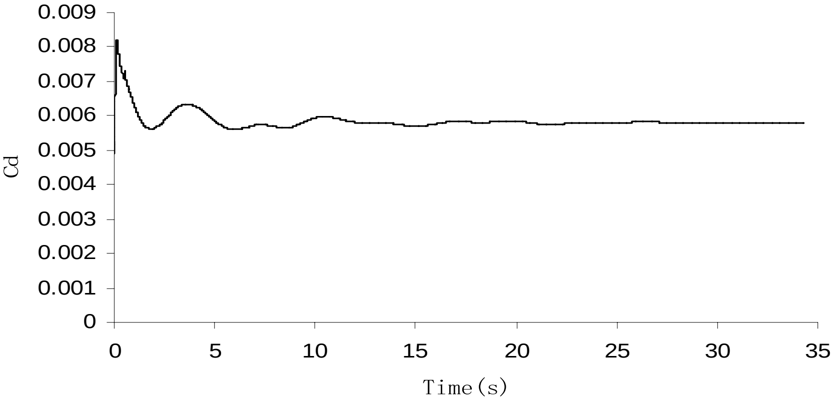

(c) *Fr*=0.316

Fig.6.10 The coefficient of resistance changing with time

We calculate the model at three different Froude numbers: 0.25, 0.289 and 0.36 respectively. The time step is 0.005 second, the minimum size of the grid is 0.008 meter. Fig.6.10 shows the change of resistance coefficient with time. From Fig.6.10 we can see that the coefficient of resistance converge to a steady value of approximately 0.006.

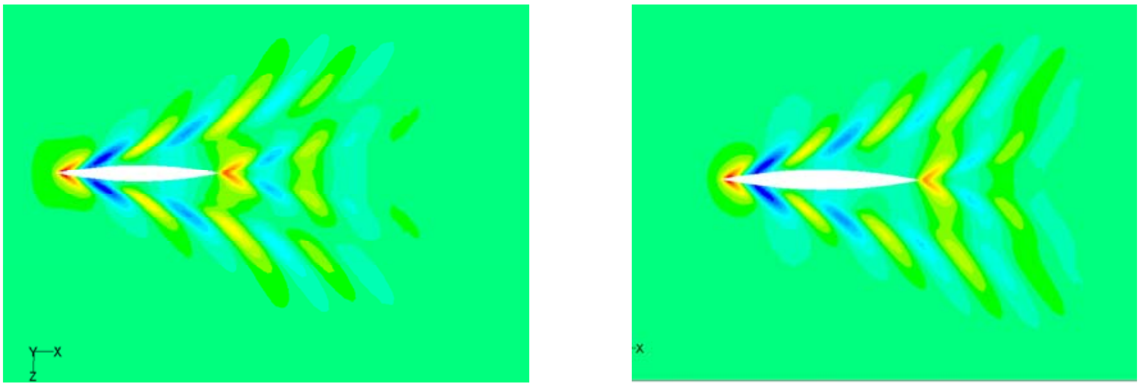

(a) *Fr*=0.25 (b) *Fr*=0.289

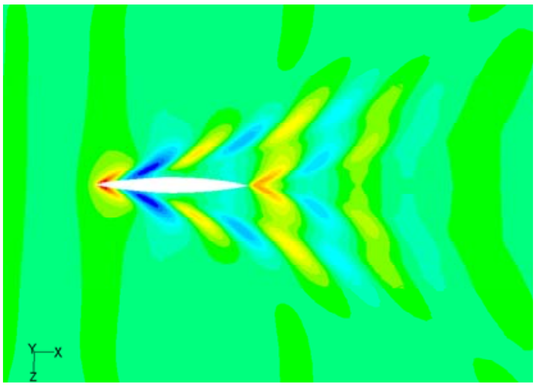

(c) *Fr*=0.316

Fig.6.11 Wave patterns generated by a Wigley hull advancing at different Froude numbers

The computed wave pattern for the standard Wigley hull at Froude numbers 0.25, 0.289, 0.316 are shown in Fig.6.11 when the result converged. These are top views of the free surface profiles. The free surface wave is well developed and does not change significantly after that. The results confirm that the wave starts at and transverse wave appears after the stern.

Fig.6.12 presents the comparisons of the wave elevations along the hull between the experimental measurements and the numerical results from the FLUENT software for Froude numbers 0.25, 0.289 and 0.316, respectively. The experimental measurements are given in Kajitani et al. (1983). The values agree well with the experimental measurements over the series of Froude numbers considered. The wave elevations from the Fluent software are a slightly lower near to bow than the experimental measurements (Beck (1998)), in particular at Froude number *Fr*=0.316. The rest of the wave elevations along the hull show a satisfactory agreement with the experimental measurements, particularly at Froude number *Fr*=0.316, where the wave elevation is almost coincident with the experimental data.

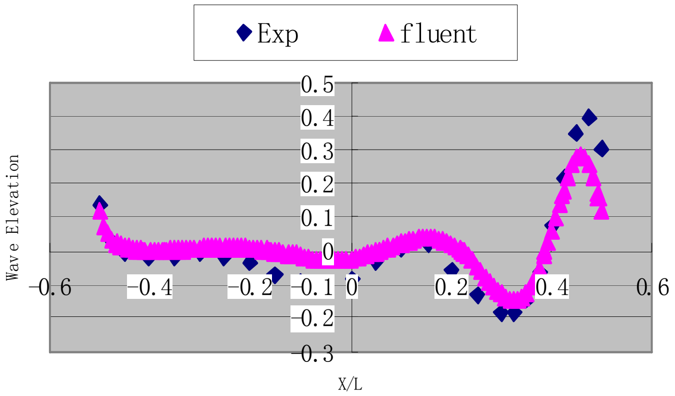

(a) *Fr*=0.25

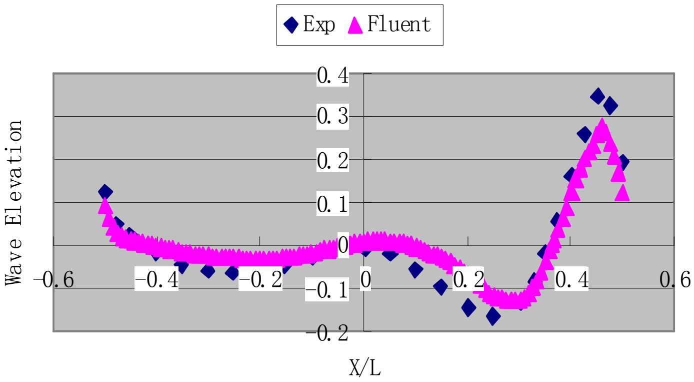

(b) *Fr*=0.289

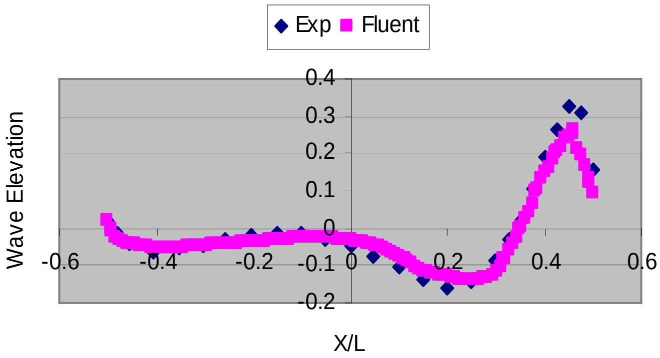

(c) *Fr*=0.316

Fig.6.12 Comparison of wave elevation along Wigley hull with experimental measurements at *Fr*=0.25, 0.289 and 0.316, respectively

A comparison of total resistance coefficient with the published results (Beck, 1998)) is given in Fig.6.13. The total resistance coefficient is defined by $C_d = R_t /(0.5\rho U^2 S)$, R_t is the total resistance, U is the velocity of flow and S is the hull wetted surface area.

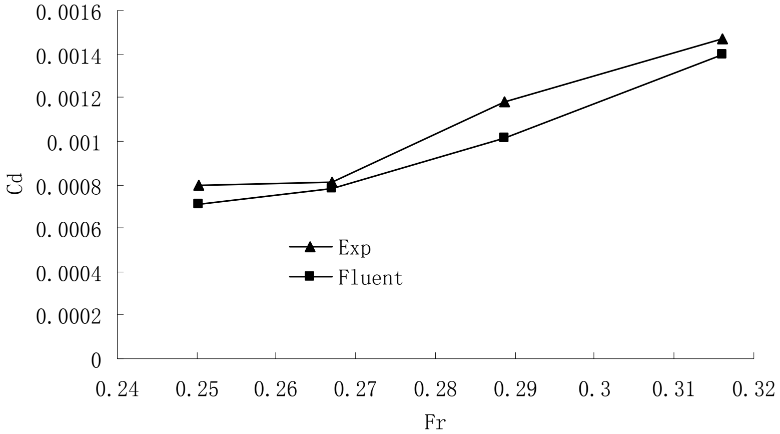

Fig.6.13 Comparisons of the wave resistance coefficients vs. Froude numbers after motion becoming steady

As can be seen in the figure 6.13, the numerical values of C_d have the same trend to that of experimental data as Froude number increases. The agreement between them in the range of Froude number is satisfactory.

6.2.3 Effect of sizes of computation domain

The case of wigley hull with Fr=0.316 is chosen to analyze the effect of sizes of computation domain. There are two sizes shown in table.6.1.

Table.6.1 Two sizes of computation domain

	No.1 domain	No.2 domain
downstream	4 ship length	7 ship length
upstream	1.5 ship length	1.5 ship length
in the z-direction	1.5 ship length	3 ship length
in the positive y-direction	1 ship length	1 ship length
in the negative y-direction	2 ship length	2 ship length

Fig.6.14 shows the comparison of wave pattern for different sizes of computation domain. From Fig.6.14 we can see that the wave patter is similar for two sizes of computation domain. Furthermore, the resistance coefficient C_d is 0.0045 for No.1 domain and 0.052 for No.2 domain. So the results do not depend on the size of computational domain used in 6.2.1. The elements in No.1 domain are 473250 and in No.2 domain are 1047000. We almost can save half computation time.

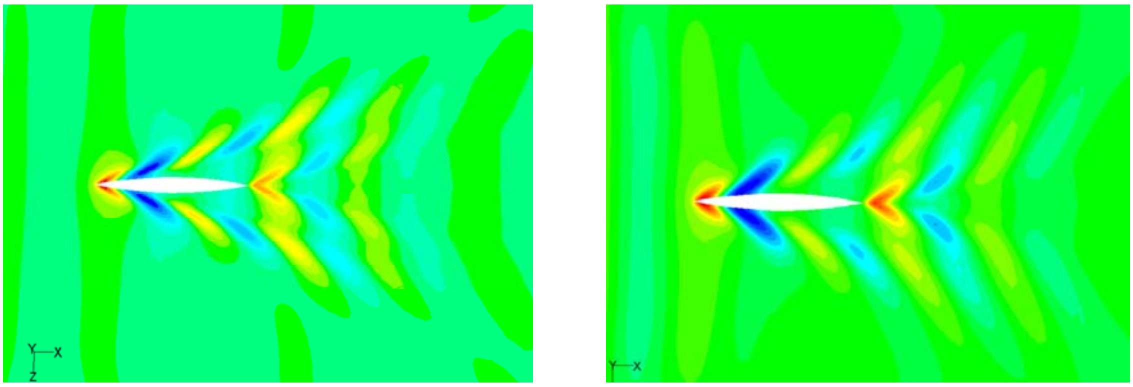

(a) No.1 domain (b) No.2 domain

Fig.6.14 Comparison of wave pattern for different sizes of computation domain

6.2.4 Effect of grid size

In order to investigate the effects of cell sizes, we select the case of *Fr*=0.316 and *Fr*=0.289. Fig.6.15 shows the comparison of the wave elevation with experimental measurements for different sizes of cells. It can be seen that the coefficient is closer to experimental results with reduction in cell sizes and become acceptable when $\Delta l = 0.008$.

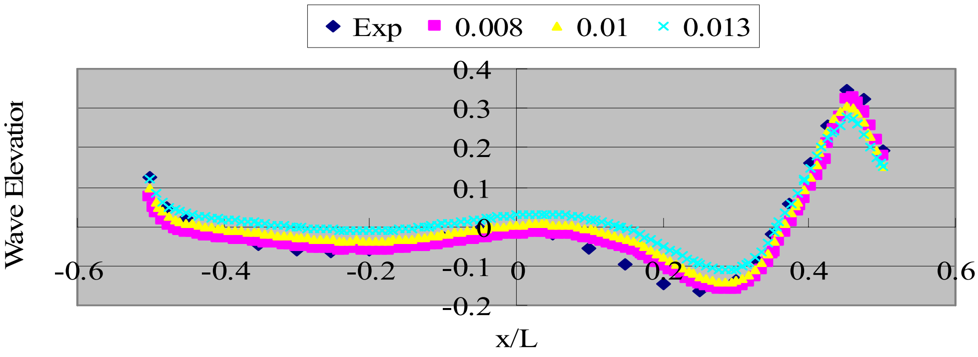

(a) *Fr*=0.289

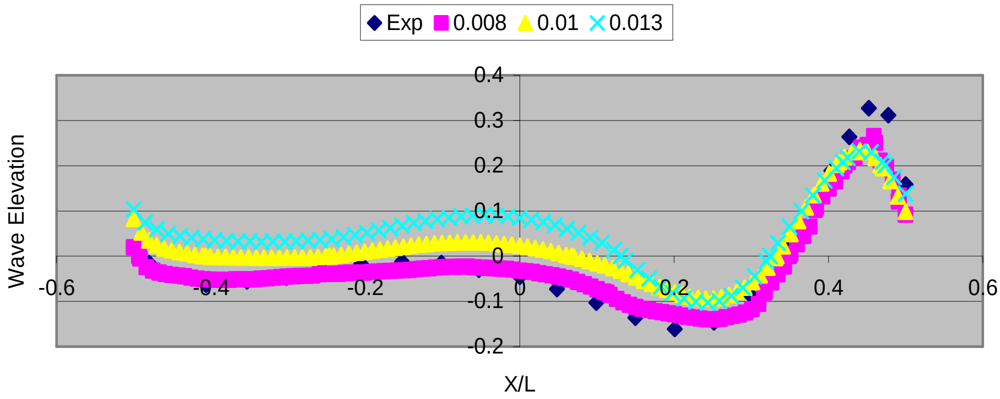

(b) *Fr*=0.316

Fig.6.15 Comparison of the wave elevation along Wigley hull with different mesh size

7. NUMERICAL INVESTIGATIONS ON HYDRODYNAMIC CHARACTERISTICS OF A PLANING CRAFT IN STEADY FLOW

In order to evaluate ship hydrodynamics in design we need to obtain the flow characteristics around the hull. Normally there are two ways to predict the flow characteristics of the ship. The first one is the model test, in which a ship model is tested in a towing tank and the second one is the computational fluid dynamic (CFD) simulation. Model test is a traditional method and has been used for a long time. In Chapter 3 and Chapter 4 the details of model tests for planing craft and gliding-hydrofoil craft have been presented. However it requires a lot of manpower and material resources, and is quite expensive. In addition, some variables, especially the spatial distribution of some important parameters, e.g. the pressure, cannot be measured detailed in model tests. CFD simulates the flow field around the hull based on the highly developed computer technology and CFD software. Compared with the experiments, the numerical investigations is usually cheaper and is able to provide more detailed insight of continuous spatio-temporal distribution of physical quantities.

In this chapter, the FLUENT is used to investigate the hydrodynamic characteristics of a planing ship in steady flow. The resistance of the craft, the wave pattern and the pressure field near the craft are investigated. By comparing the simulated and experimental results to check whether CFD software FLUENT is sufficiently accurate for studying high-speed craft in viscous free surface flow.

7.1 Calculation model for planing craft

The planning craft simulated in this chapter is the ship model we discussed in Chapter 3. The details about the craft are shown in Chapter 3. Table7.1 is the principal dimensions of the planing craft.

Table 7.1 Principal dimensions of planing craft

Scale ratio	10
Length (m)	1.18
Breadth (m)	0.35
Draft (m)	0.07
Initial wetted length L_S (m)	1.12

A Cartesian coordinate system *o-xyz* fixed to the body is established, with its *y*-axis in the opposite direction of gravity, y=0.05m at the undisturbed free surface and x-axis in the longitudinal direction towards the stem of the ship (Fig.7.1).

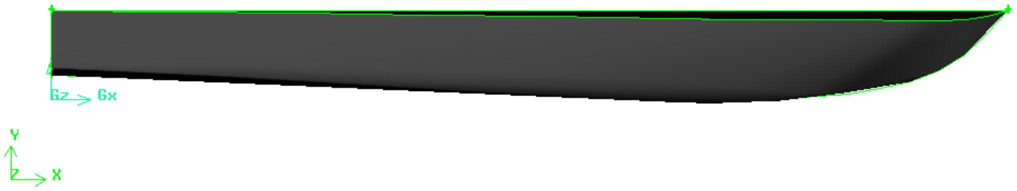

Fig.7.1 Planing craft and coordinate system (z direction)

7.2 Grid Generation and Turbulence model

When using the CFD method to simulate the viscous flow field caused by a planing craft, the first step is to discrete the computational domain, i.e. grid generation. The quality of the grid is sensitive to the accuracy of the results. Therefore much attention should be paid to the grid generation procedure in numerical investigations. Normally the grid generation may spend more than half of the entire CPU time for a 3D flow simulation with complex geometry of a ship. At present, the geometry of the model studied in ship dynamics is becoming more and more complex. How to generate high-quality computational grid has become an important issue of CFD, even for commercial software, in which the quality of the cell need to be manually controlled.

In this chapter we choose an actual planing craft as the simulation model. The geometry of the stem and the stern of the planing craft are complex. As discussed before, single-block structured grid for such cases may not have sufficient high quality to ensure good accuracy of the numerical results, and, therefore, multi-block unstructured-structured grid is used here. The discussion on preferred grid type can be found in the previous chapter and will not be repeated here. The computational domain is discretised by hybrid tetrahedral-hexahedral mesh where hexahedral (brick) cells are relatively more computationally efficient than tetrahedral cells and thus distributed over the whole computational domain except region near complex body surface where tetrahedral cells are generated in order to well fit the boundaries with higher quality than the hexahedral cells. This configuration of the computational grid take the advantages, minimise the disadvantages of both hetrahedral and hexahedral grids and leads to high robustness of the solution. The whole computational domain in this investigation are divided into 48 blocks, the total number of cells are 705,490. In order to simulate the free surface and boundary layers , the grids near the free surface and hull surface are further refined. Fig.7.2 and Fig.7.3 show the grid of the computational domain and the planing hull surface. Based on the discussion in Chapter 5 SST $k-\omega$ turbulent model are chosen for the problem in this chapter.

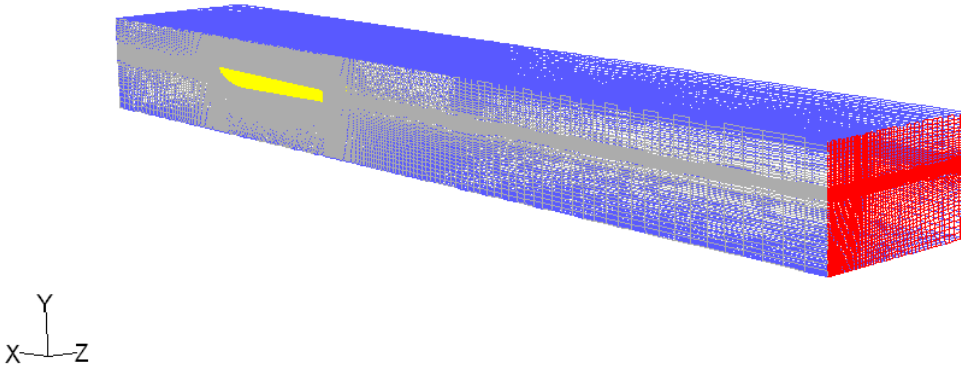

Fig.7.2 Computational grid with 705490 elements

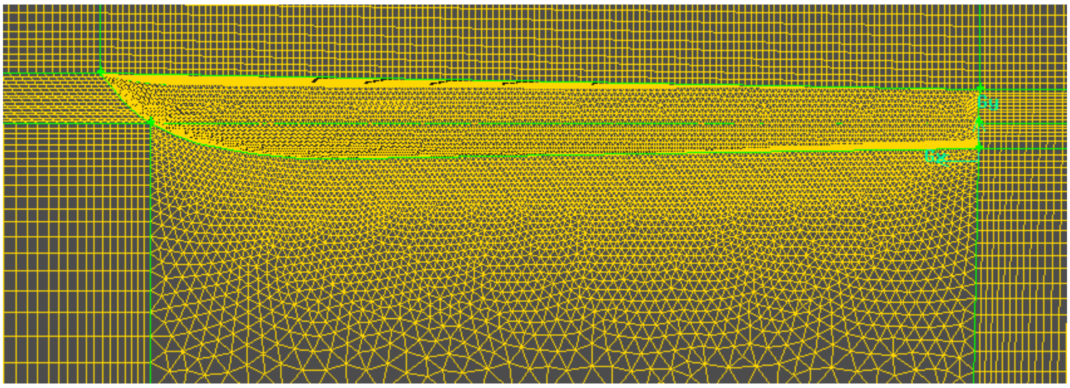

Fig.7.3 Computational grid near planing craft

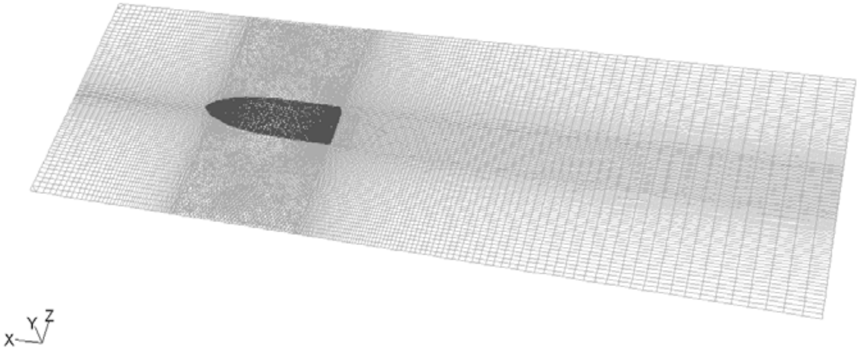

Fig.7.4 Grid on the water-surface around the planing craft hull

Turbulence model selection is another important factor that affects the accuracy of the results. Based on the discussion in Chapter 5 SST $k-\omega$ turbulent model was chosen for the problem in this chapter.

7.3 Boundary condition and initial condition

In order to save the computational time, only half of the domain was considered, assuming the fact that the problem with planing craft is symmetrical about the central longitudinal plane of the craft. Through implementing the symmetrical condition on the central longitudinal plan of the craft, the solutions on other half domain can be obtained and the solutions within the entire domain are shown in the post-processor as in Fig.7.4. The whole computation domain is surrounded by the following boundaries:

(1) Upstream boundary, 1.5 ship lengths upstream from the stem;

(2) Downstream boundary, 4.5 ship lengths downstream from the stern;

(3) Side boundary, 1.5 ship length in the transverse direction of the craft (z-direction in the coordinate system used in the simulation),

(4) Bottom and top boundaries: 1 ship length vertically above the free surface and 2 ship length submerged below the free surface (y-direction in the coordinate system used in the simulation);

(5) Symmetric plane, consistent with the central longitudinal plane of the craft, i.e. the grey surface in Fig.7.2;

(6) Ship hull. 396 nodes on the hull wetted surface.

In the simulation, the coordinate system is fixed with the craft and so the craft speed is represented by an incoming current at the same speed but in the opposite direction. The no-slip boundary condition is imposed on the hull surface. The free surface is identified by a volume fraction which is obtained by solving the VOF equation. The boundary condition with user-defined function (UDF) based on pressure outlet introduced in Chapter 5 is applied at the outlet boundary.

7.4 Numerical results

Although this is a steady problem in the coordinate system we use, the free surface profile is unknown at prior to the numerical simulation and, therefore, the unsteady module is chosen with initial condition for the free surface being still water. After sufficiently long duration of the simulation, the free surface, as well as the whole system, becomes steady. We analyse the results at steady state for the comparison with the experimental data.

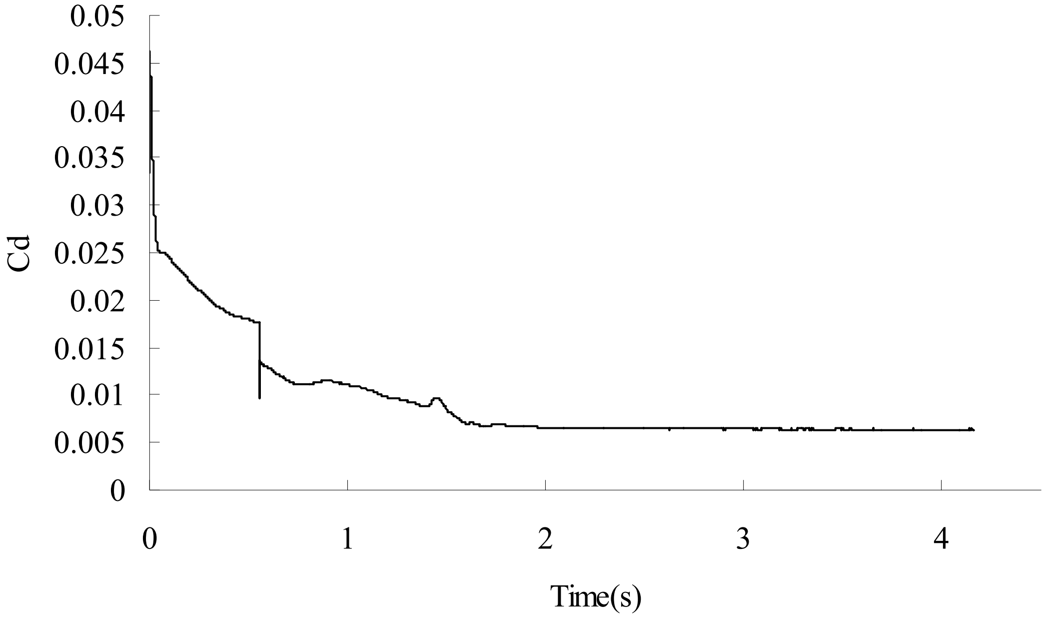

Fig.7.5 Time history of the convergence of the resistance coefficient

In the first case considered here, the speed of the ship model is U=4.39m/s, corresponding a Reynolds number of 4.89×10^6 and a Froude number of 1.3. The numerical results are obtained on a single-processor computer Pentium IV 2.4 GHz and 2Gb RAM. Fig.7.5 shows the time history of the resistance coefficient, which is essential for the design and analysis of the planing craft. As expected, the resistance coefficient converges to a constant value with the increase of computational time. The resistance coefficient at steady state is 0.005. This justifies the approach that uses unsteady model to simulate steady problem with free surface.

7.4.1 Validation of resistance coefficients with different Froude numbers

The experimental results and the corresponding numerical results of resistance coefficient are compared in Fig.7.6 (a) in the cases of Froude number ranging from 0.6 to 1.3. As can be seen in Fig.7.6 (a), the numerical values of C_d have the same trend as those of experimental data with a varying Froude number.

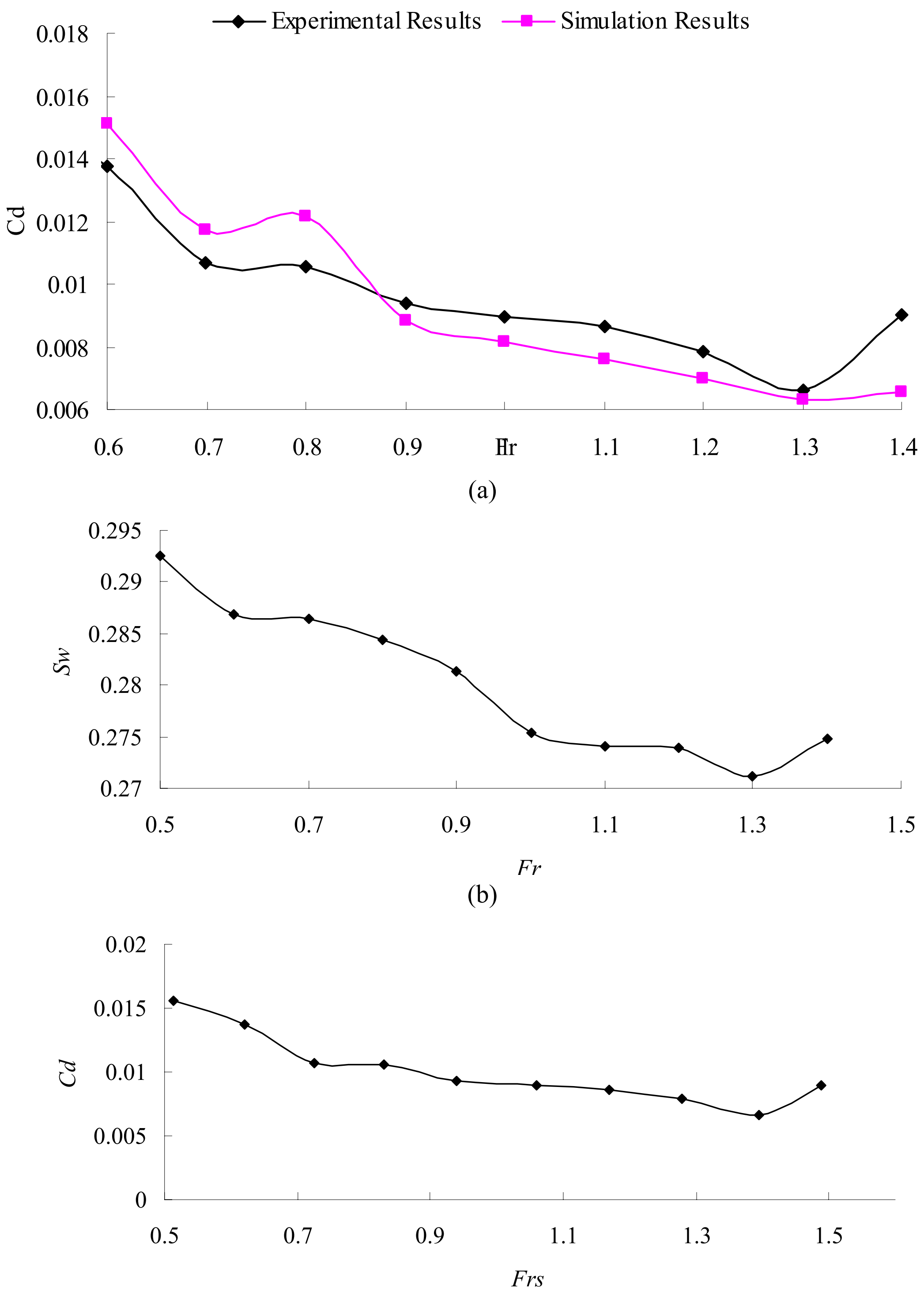

Fig.7.6 Comparison of the resistance coefficients (C_d)

A visual difference between the experimental results and the simulation results can be found in Fig.7.6(a) for the resistance coefficients within a wide range of the Froude number. The resistance coefficients obtained from the numerical simulation are greater than the experimental data when $Fr<=0.8$ but are smaller than the experimental data when $Fr>=0.9$. This may be due to the fact that the area of wetted surface in the experiments is different from that in the numerical simulation. In the numerical investigation, the trim angle of the planing hull is specified by the corresponding value in the experiment at the steady state and the vertical location of the centre of gravity of the hull is located satisfying the wetted surface at initial state (at rest) is the same as the steady-state value in the corresponding experiment. The effects of the ship wave on the change of the wetted surface in the numerical investigation, which may be significant as shown in Fig.7.6(b), is not considered in Fig.7.6(a). Therefore, it is more convenient to compare the resistance coefficients in terms of the wet length Froude number (Fr_s) using Froude number similarity law. The corresponding comparison of resistance coefficients in cases with different Fr_s between the numerical simulation and the experiments is presented in Fig.7.6(c), which confirms a better agreement between the numerical and experimental results.

7.4.2 Wave patterns corresponding to different Reynolds numbers

As indicated before, a board with a height of 80mm is fixed on the edge of the upper deck of the physical model to prevent green water and water spraying on the deck.

The performance of such board is clearly demonstrated in Fig.7.7 comparing the wave profile around the planing craft in the case with (Fig.7.7b) or without the board (Fig.7.7a). In this case, the Froude numbers is 0.6. As illustrated, water has flowed over the deck in the case without the board and similar water spraying is not found in the case with board. This is consistent with what observed during the physical model test.

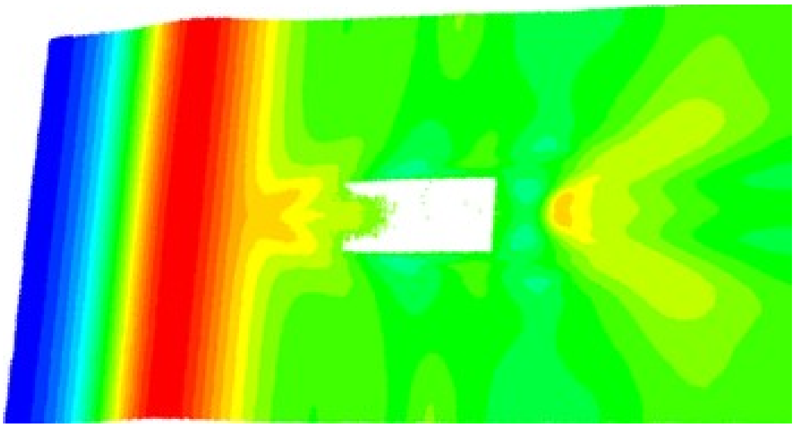

(a) Without the board

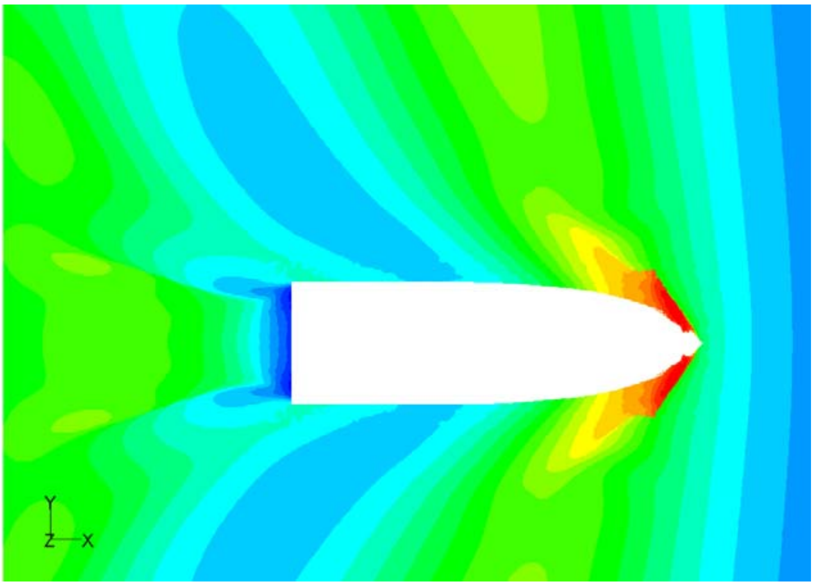

(b) With the board

Fig.7.7 The influence of the board on wave patterns generated by a planing craft (*Fr*=0.6)

More results with wave profiles around the planing craft are given in Fig.7.8 for Froude numbers of 0.6, 0.9and 1.04, respectively. These are top views of the free surface profiles. It can be noted that the free surface profile presented in Fig.7.8 is at steady state and is well developed.

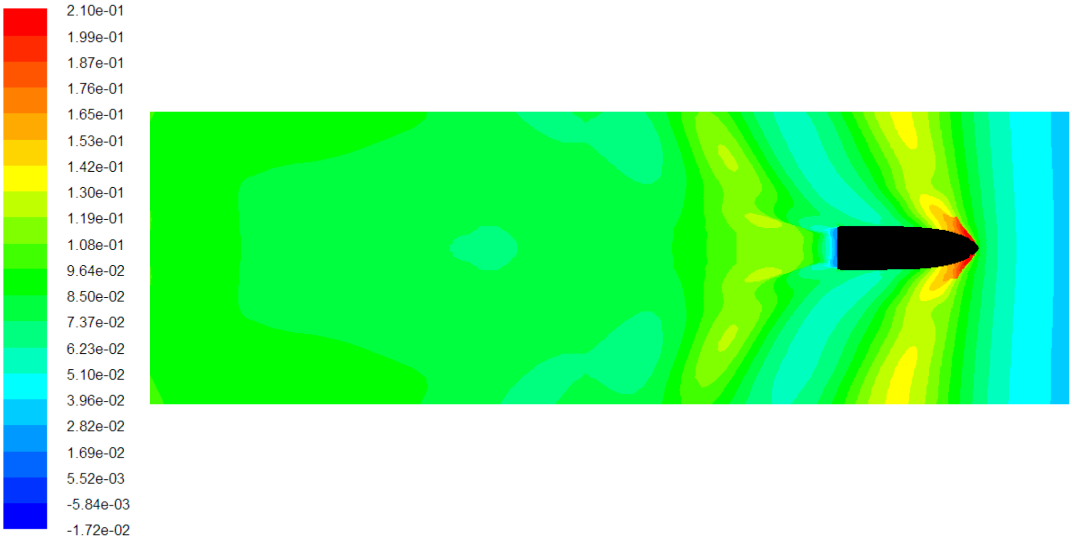

(a) *Fr*=0.6

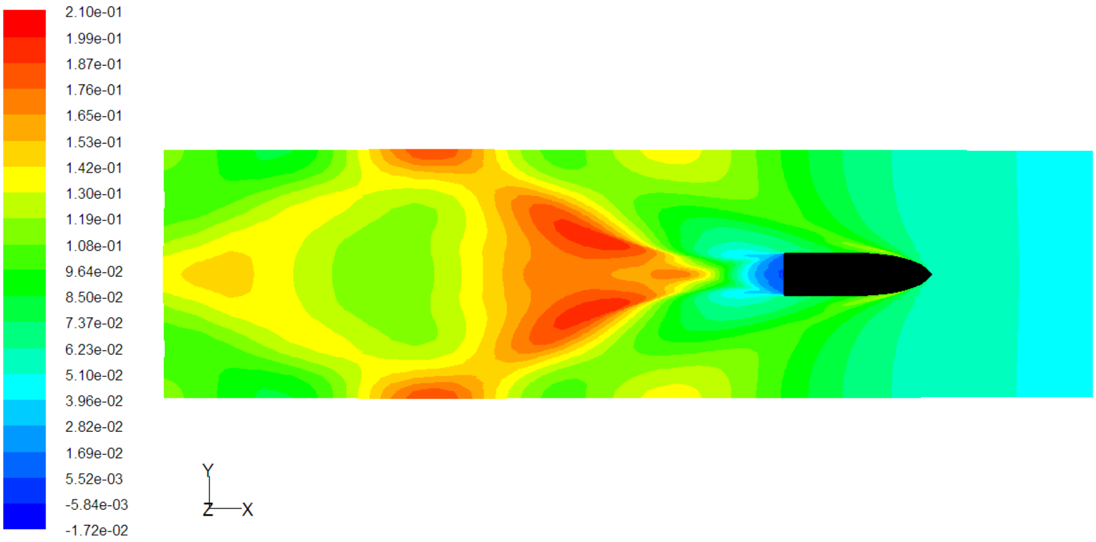

(b) *Fr*=0.9

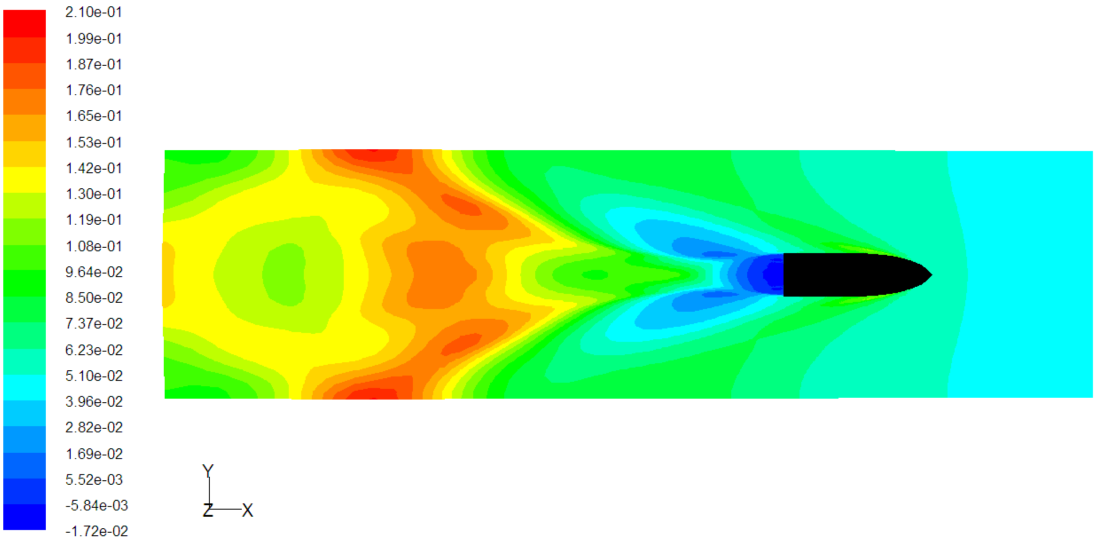

(c) *Fr*=1.0

Fig.7.8 Wave patterns generated by a planing craft advancing at different *Fr*

It can be seen that the wave patterns are different for the cases with different Froude numbers. For lower Froude number, the wave spreads in a relatively wider area and the maximum wave height occurs at the bow area, whereas for the relatively higher Froude number, the wave spreads in a narrower area and the maximum wave height occurs behind the ship. It should be noted that in Fig.7.8, clear reflection from side walls can be identified. Such reflection is not expected in practical cases with ship travelling in open sea and may slightly affect the numerical result. In further numerical investigation, different width of the tank may be considered to ensure the refection from the side wall does not affect the hydrodynamic behaviour of the ship, as indicated in Chapter 6 for Wigley Hulls. However, for the investigation presented in this section, the refection wave physically exist in the model test in the towing tank and is confirmed by the experiments.

7.4.3 Effect of sizes of computation domain

The corresponding investigation of the effects of the reflection waves from the side wall in the cases with planing craft is presented here. In this case, *Fr*=0.9 There are two sizes shown in table.7.2. The elements in No.1 domain are 478495 and in No.2 domain are 1081074.

Table.7.2 Two sizes of computation domain

	No.1 domain	No.2 domain
downstream	4.5 ship length	6.5 ship length
upstream	1.5 ship length	1.5 ship length
in the z-direction (transverse direction)	1.5 ship length	3 ship length
in the positive y-direction (vertically above the free surface)	1 ship length	1 ship length
in the negative y-direction (vertically below the free surface)	2 ship length	2 ship length

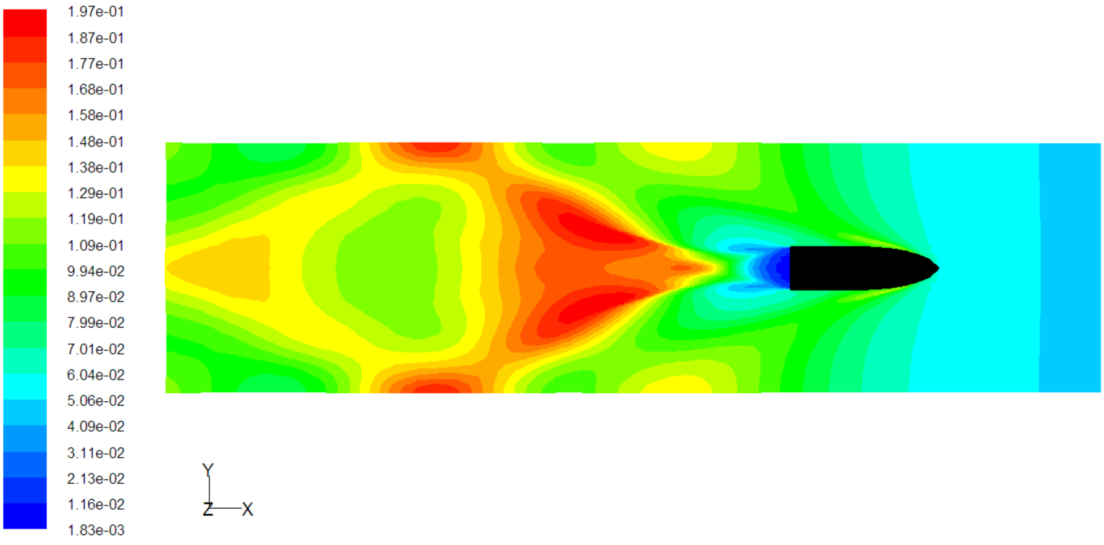

(a) No.1 domain

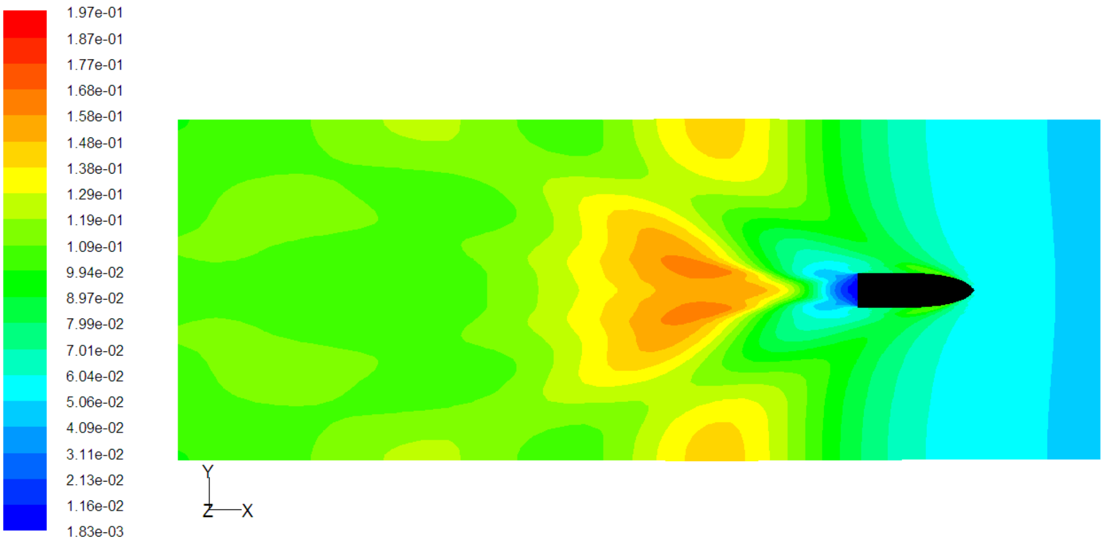

(b) No.2 domain

Fig.7.9 Comparison of wave pattern for different sizes of computation domain

Fig.7.9 shows the comparison of wave pattern for different sizes of computation domain. It can be seen that the wave patter is slightly different in the cases with different sizes of computation domain. However, the difference in resistance coefficient C_d is smaller than 3% (i.e. 0.008845 for No.1 domain and 0.00861 for No.2 domain), which may be considered as acceptable in practices. This indicates the refection waves due to the side wall do not significantly affect the resistance coefficient of the craft. This is reasonable because the refection waves mainly exist in the downstream of the ship and less likely they may affect the pressure distribution on the hull surface. Therefore, for the purpose of studying the resistance coefficients of the planing craft, a narrow computational domain is preferred because the CPU time spent on the case with narrower domain is only half of that for the wider domain However, if the wave field of planing craft need to be discussed in detail, the computation domain should be expanded.

7.4.4 Pressure distribution around the hull

Fig. 7.10 is the pressure coefficient distribution on the planing craft at different speed. The pressure coefficient C_P is expressed by:

$$C_P = \frac{P}{0.5\rho U^2 S} \tag{7.5}$$

where, P is the absolute pressure on the planing craft, S is the wetted surface area, U is the incoming speed and ρ is the density of the fluid.

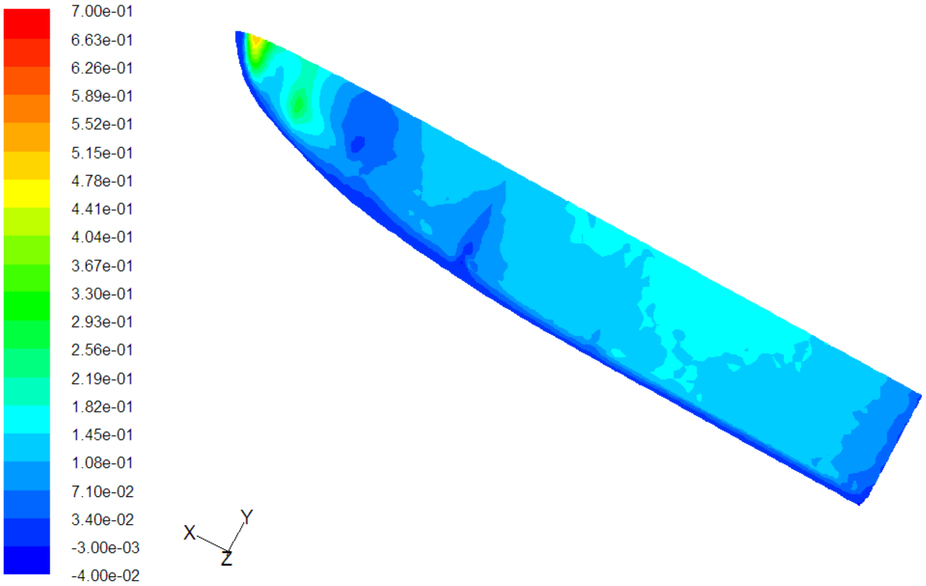

(a) U=3.06 and Fr=0.9

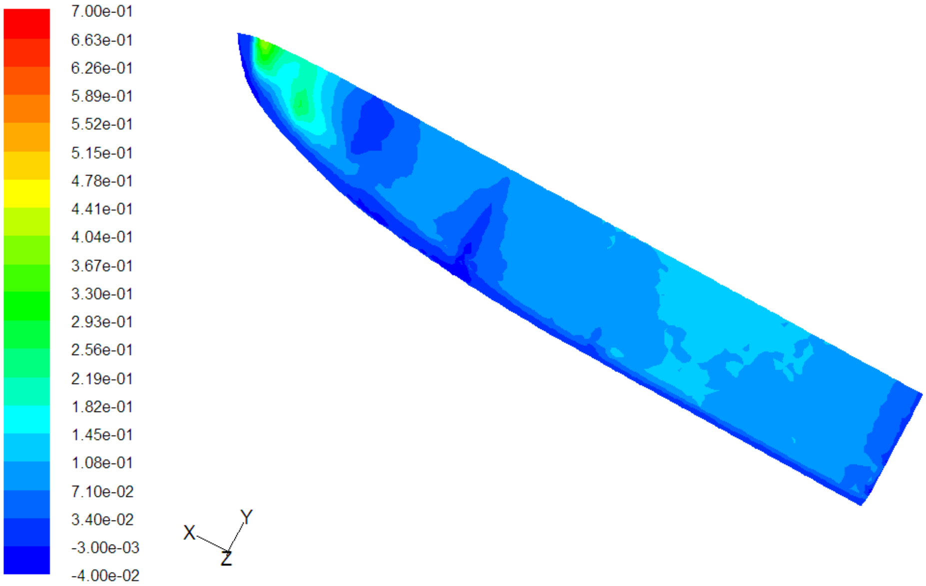

(b) U=3.4 Fr=1.0

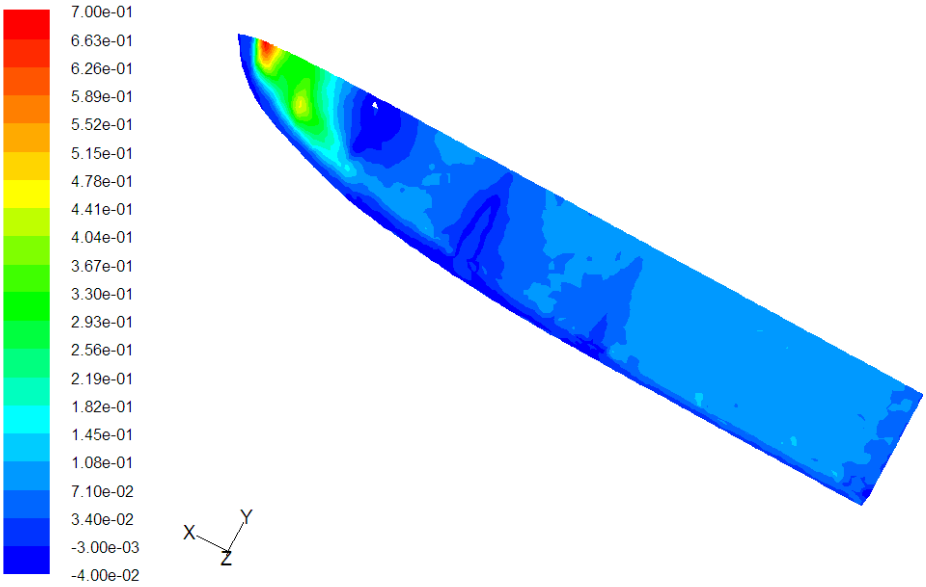

(c) U=4.76 Fr=1.4

Fig.7.10 Pressure distribution on the planning craft at different speeds

From Fig.7.10 we can see that the maximum pressure coefficient (the red region) occurs in the front of hull. Negative pressure areas (the dark blue region) are observed in the region of the stem bottom and middle ship bottom on port side and starboard side. And the negative pressure areas become smaller with the increase of Froude number. When the water flows with incoming speed U along the hull, the speeds are different at the different position on the hull because the hull is a complex 3D curved surface. The point in the front of hull is the stationary point, for which the speed is zero. According to Bernoulli equation, the pressure varies inversely with the speed. So the maximum pressure occurs on the stationary point. With the water flowing along the hull, the speed of water increases and the pressure decreases. When the speed of water is larger than the incoming flow speed U, there will be a negative pressure area. In the front of middle ship there are spray and velocity change in these region so the speed of water is larger than the incoming flow speed U. With the increase of Froude number area of spray and velocity change decrease so the area of negative pressure decrease, too. However, no experimental results of pressure distribution were available for planing craft.

8. NUMERICAL STUDY OF HYDRODYNAMICS CHARACTERISTICS OF A GLIDING-HYDROFOIL CRAFT IN STEADY FLOW

After successful numerical simulations on the viscous flow around planing crafts considering the free surface, the FLUENT is used to study the hydrodynamics characteristics of a gliding-hydrofoil craft (GHC) in steady flow in this section. By comparing the numerical results with the experimental results measured in Chapter 4 to further validate that the CFD commercial software FLUENT for modelling the GHC.

8.1 Calculation model for the gliding-hydrofoil craft

The GHC used in the numerical simulation is the same as the physical model detailed in Chapter 4. Table 8.1 gives the principal dimensions of the craft and the hydrofoil for completeness.

Table 8.1 Principal dimensions of gliding-hydrofoil craft

Scale ratio	10
Length (m)	1.18
Breadth (m)	0.35
Draft (m)	0.07
Initial wetted length L_S (m)	1.12
chord length (mm)	50
foil span (mm)	390
maximum thickness of hydrofoil (mm)	6

Considering a right-hand Cartesian coordinate system fixed in the space *o-xyz* as shown in Fig.8.1. The horizontal and vertical axes, *ox* and *oy*, are, respectively, in the longitudinal direction towards the stem of the ship and in the opposite direction of gravity. The origin *o* is at the base plane at transom, shown in Fig.8.1.

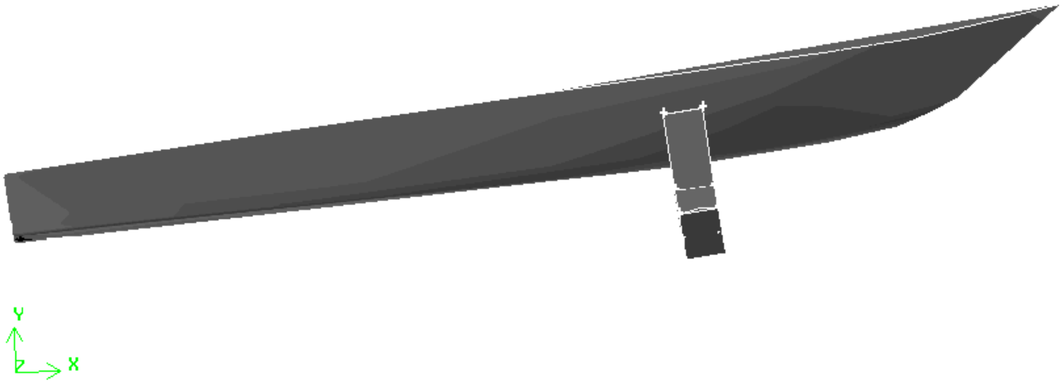

Fig.8.1 Gliding-hydrofoil craft and coordinate system

The geometry of the gliding-hydrofoil craft is more complex than the planing craft as it has a hydrofoil attached to the bottom of the hull (Fig.8.1). The multi-block unstructured-structured grid is used, similar to the case with planing craft. The computational domain is 4.5 ship length downstream from the extreme point of the ship aft, 1.5 ship lengths upstream from the extreme point of the ship forward, 1.5 ship length in the transverse direction of the hull (i.e. *z*-direction), 1 ship length vertically above the free surface (in the positive *y*-direction) and 2 ship length vertically below the free surface (in the negative *y*-direction). Again, hybrid tetrahedral-hexahedral grid is used to discretise the computational domain. The computational domain is divided into 48 blocks and there are in total 967,726 cells. The cells near the free surface and the hull surface are further refined to ensure sufficiently high resolution to capture the free surface and the boundary layer flow.

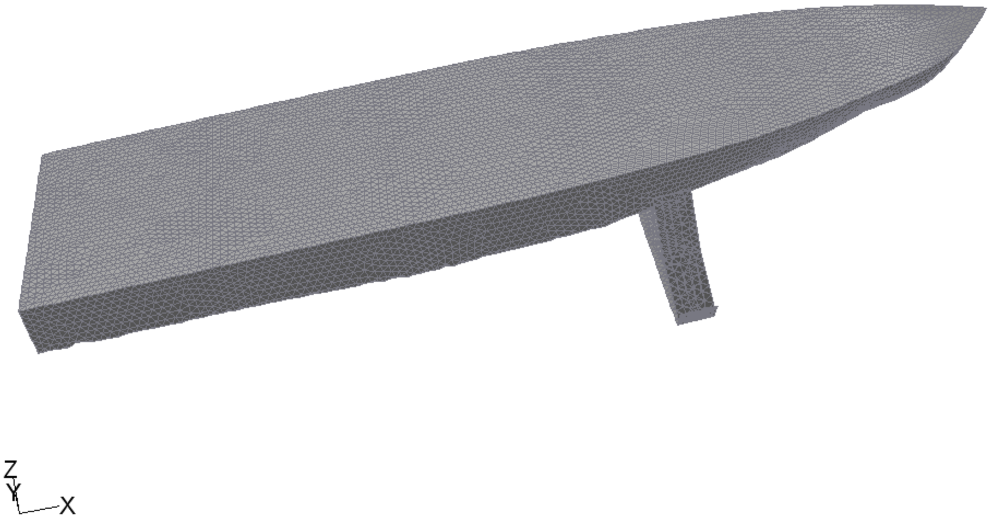

Fig.8.2 The Cartesian coordinate system o-xyz and mesh for a ship hull

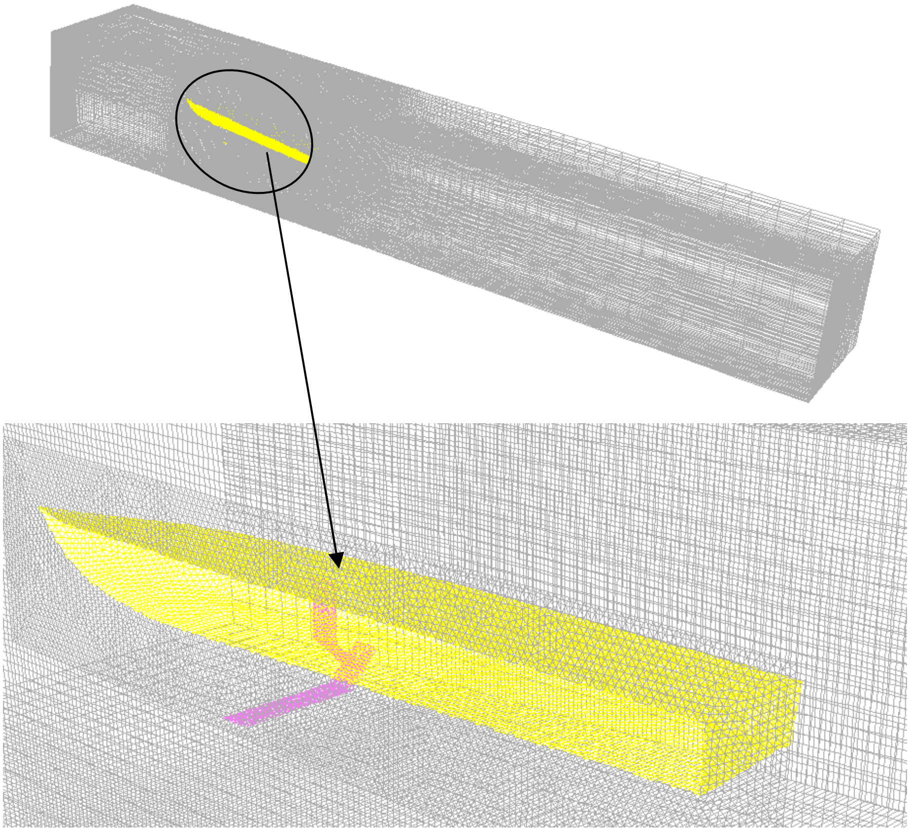

Fig.8.3 Computational grid with 967726 elements

Fig.8.2 and Fig.8.3 illustrate the grid on the surface of the GHC and the entire computational domain. Similar to the investigations on the planing craft, only half of the computational domain is used in the numerical simulations with a symmetrical boundary condition imposed on the central longitudinal plane of the GHC (Fig. 8.3).

8.2 Numerical results and discussion

Numerical model is simulated at the design speed 4.39m/s (corresponding to the Froude number of 1.3 and Reynolds number of 4.89×10^6), the trim angle is 7 degrees consistent with the experiments presented in Chapter 4. The submergence of the hydrofoil is 50mm. The boundary conditions and the initial conditions adopted here are the same as those for the planing craft presented in Chapter 7. SST $k-\omega$ turbulent model is chosen to model the turbulence.

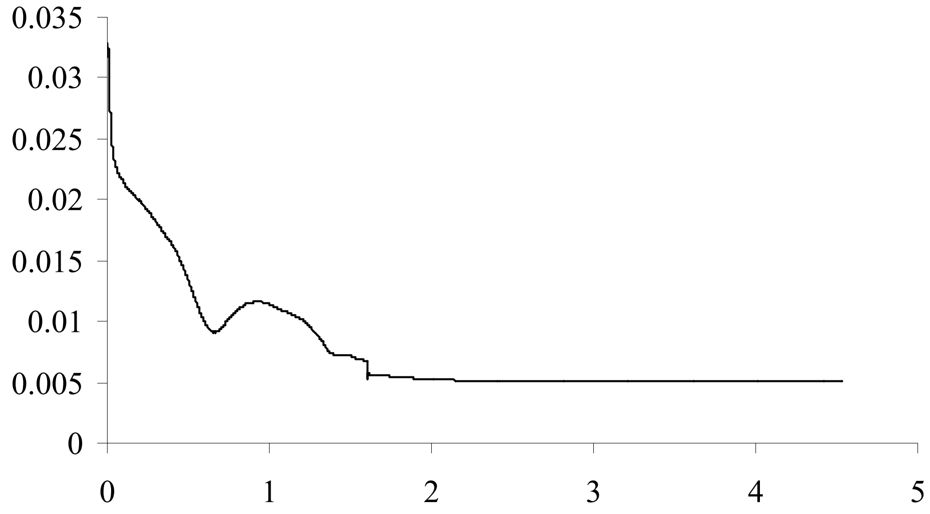

Fig.8.4 The coefficients of resistance changing with time (*Fr*=1.3)

Fig.8.4 shows the time history of the resistance coefficients. As expected, the resistance coefficients decreases and eventually becomes steady as the time increases, similar to that for the planing craft. This is a typical convergence process of the resistance of craft with free surface. The extremely large resistance coefficient in the beginning of the simulation is due to the transient effects because of a sudden induction of a large velocity from rest.

8.2.1 Validation of resistance coefficients with different Froude numbers

Fig.8.5 show the comparison of experimental resistance coefficients (in Chapter 4) with the numerical results for various Froude numbers, the initial attack angle and the submergence depth of the hydrofoil are 0° and 50mm, respectively.

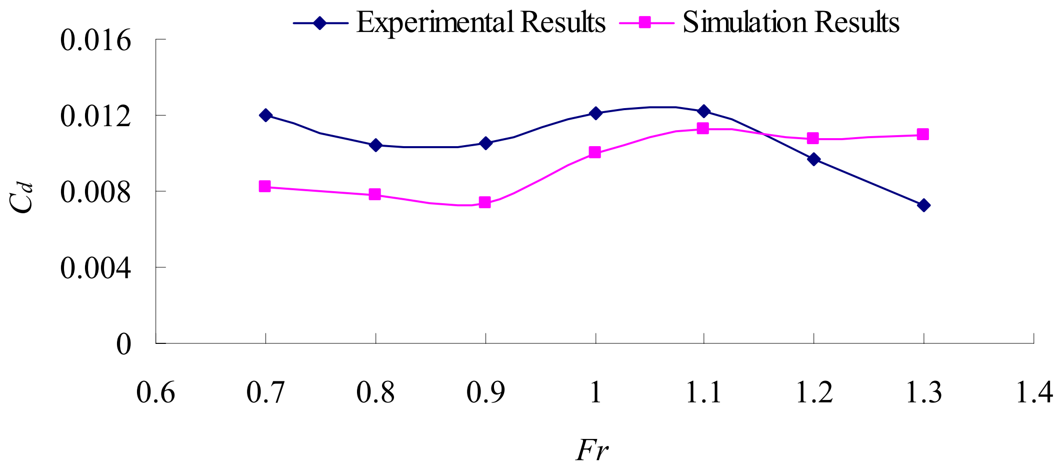

(a) Resistance coefficient vs *Fr*

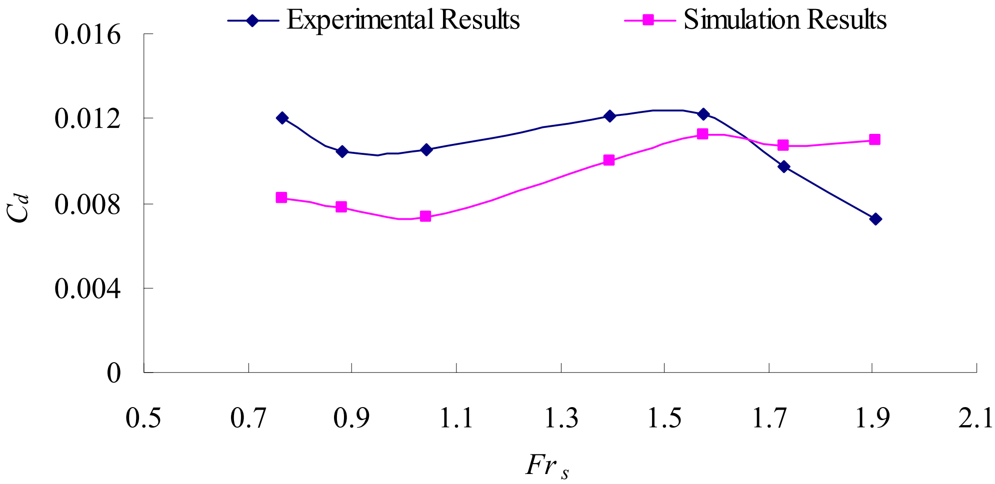

(b) Resistance coefficient vs Fr_s

Fig.8.5 Resistance coefficient of gliding-hydrofoil craft for various length Froude number (initial attack angle of the hydrofoil: 0°, submergence depth:50mm)

Similar to the investigation on planing hulls presented in Chapter 7, in the numerical simulations with GHC, the trim angle in each case is specified by the corresponding steady-state trim angles in the experiment and the vertical location of the centre of gravity is specified to satisfy the area of the wetted surface in the initial state is the same as the corresponding steady-state value in the experiment. Table 8.2 summarize the trim angle of the hull used in the numerical simulation.

Table 8.2 Trim angles, towing speed and initial area of wetted surface of GHC

Fr	0.7	0.8	0.9	1.0	1.1	1.2	1.3
Towing speed(m/s)	2.38	2.72	3.06	3.4	3.74	4.08	4.39
Trim angle(^{o})	-1.49	-0.81	2.88	6.09	6.50	6.60	7.07
S_w	0.38292	0.371796	0.271812	0.22144	0.21872	0.21805	0.215072

From Fig.8.5, we can see that two curves are consistent in terms of the trend. In particular, a hump of the resistance coefficient is found at F_r=1.1 in both the numerical and experimental results. However, a difference between the numerical results and the experimental data can be observed in Fig. 8.5, though different cell sizes and computational domain sizes have been used to ensure the convergence of the numerical results. Overall, the resistance coefficients in the numerical simulation is larger than the experimental data in case with *Fr* >1.15 and smaller when *Fr* <1.15 (Fig.8.5). However, in the comparison shown in Chapter 7, the numerical results are much closer to the model tests. This may be due to the difficulties in measuring the wetted surface in the experiments and in the numerical simulation for the cases with GHC in which local wave breaking is more significant than the corresponding cases with planing hull. Another possible reason is that the FLUENT cannot model the motion of the GHC and therefore the trim angle and the submerging depth of the hull is specified in the simulation. This is also different from the model tests which show that the trim angle changes and the hull may be moved vertically by the changing lift during the model tests. Considering these facts, the numerical results can be considered as acceptable.

8.2.2 Wave patterns for different Froude numbers

Fig.8.6 (a) to (f) are the contours of free surface elevation around GHC with Froude numbers ranging from 0.8to 1.3. It is clear that the wave patterns in cases with different Froude numbers are significantly different. Though the fully developed wake is obviously affected by the reflection from the wall, one may find that the wake spreads narrower as *Fr* increases, which is consistent with the results for a planing hull in Chapter 7. In all cases, a crest occurs at the board area; its location shifts further towards the stern as the increase of *Fr*. It is clearer in Fig. 8.7 which displays the wave elevation along the hull of GHC with different Froude numbers. As also observed from Fig.8.7, the highest elevation increases as Fr increases for relatively lower Fr, i.e. 0.8 and 0.9; as Fr further increases up to 1.3, the highest elevation decreases though the change of highest crest in the cases with *Fr* ranging between 1.0 and 1.2 is not significant. It is worth of noting that as the *Fr* increases, the trim angle also increases; the area of the wetted surface decreases up to *Fr*= 1.0 and becomes relatively steady afterwards (Fig. 4.7 and Fig.4.10). As a result, the stem is lifted above the free surface at high navigation speed, i.e. *Fr* >=0.9 in this investigation. Therefore, the water elevation curves for those cases do not cover the whole board area in Fig. 8.7.

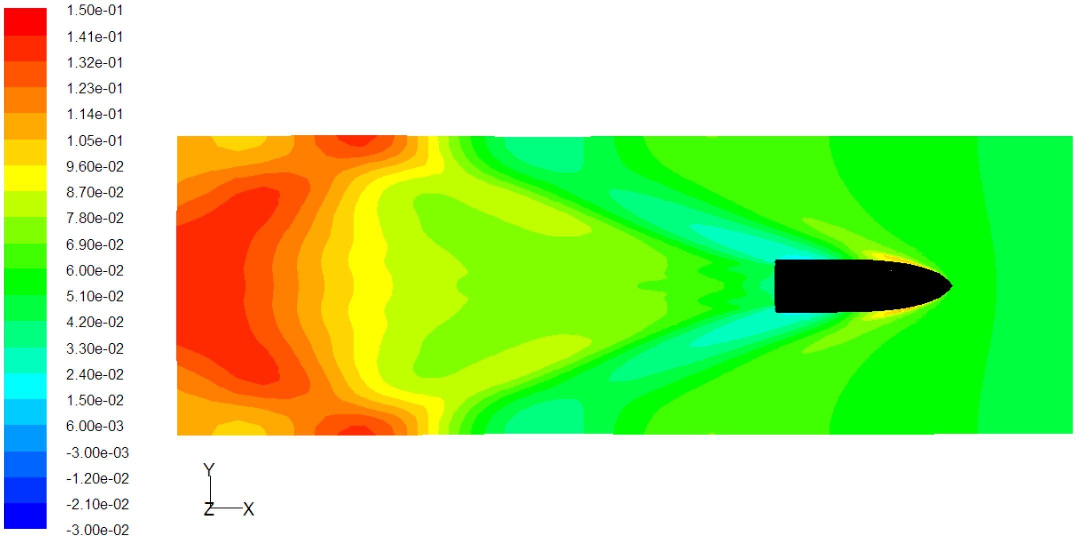

(a) *U*=2.72 m/s and *Fr*=0.8

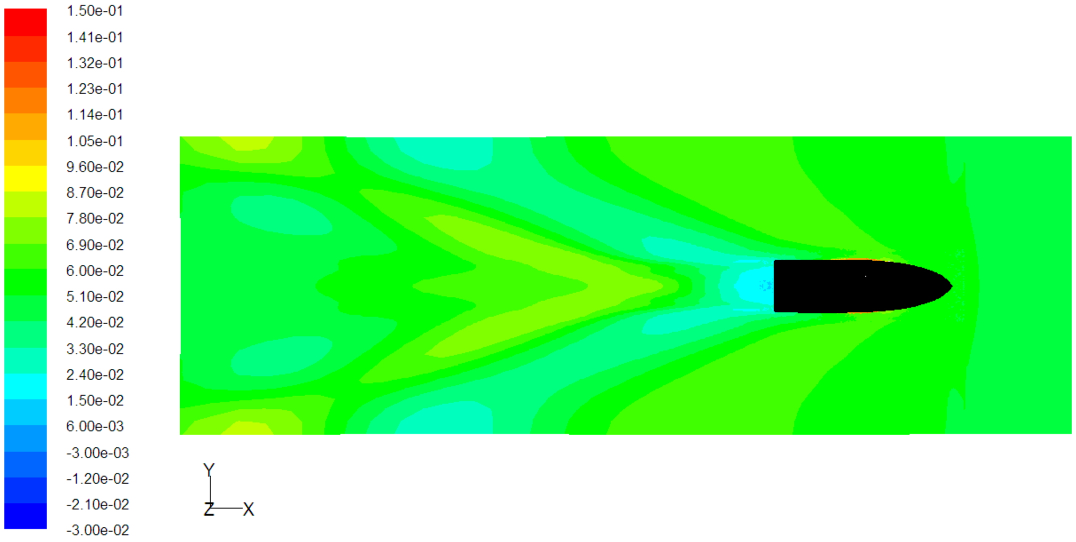

(b) *U*=3.06 m/s and *Fr*=0.9

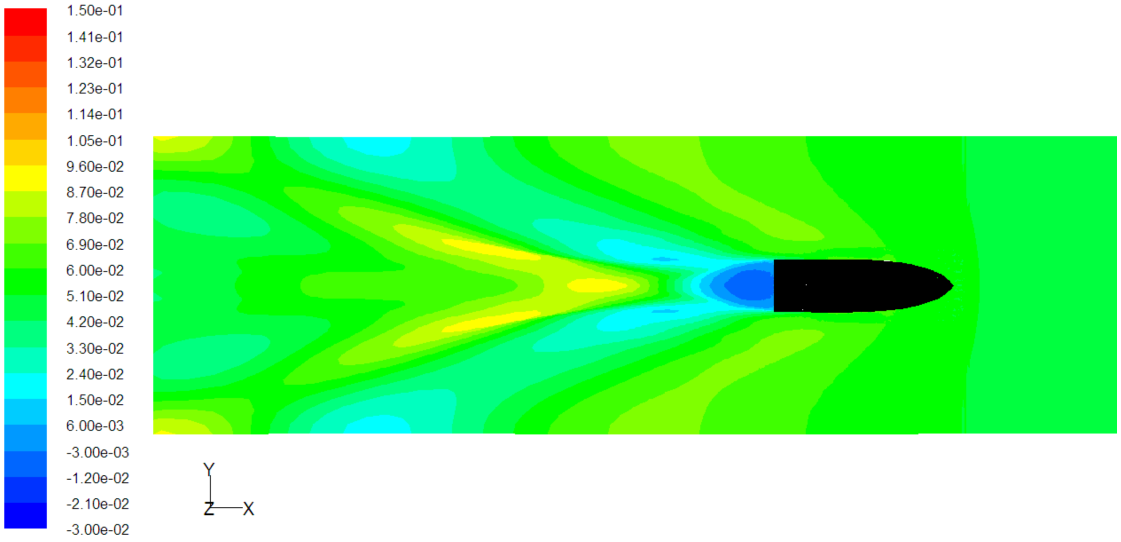

(c) *U*=3.4 m/s and *Fr*=1.0

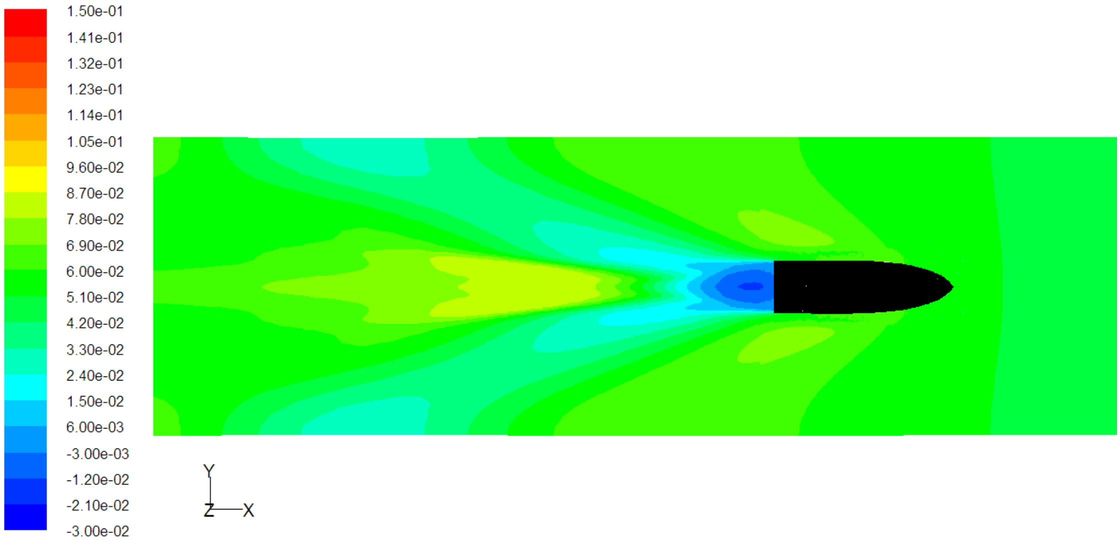

(d) U =3.74 m/s and Fr=1.1

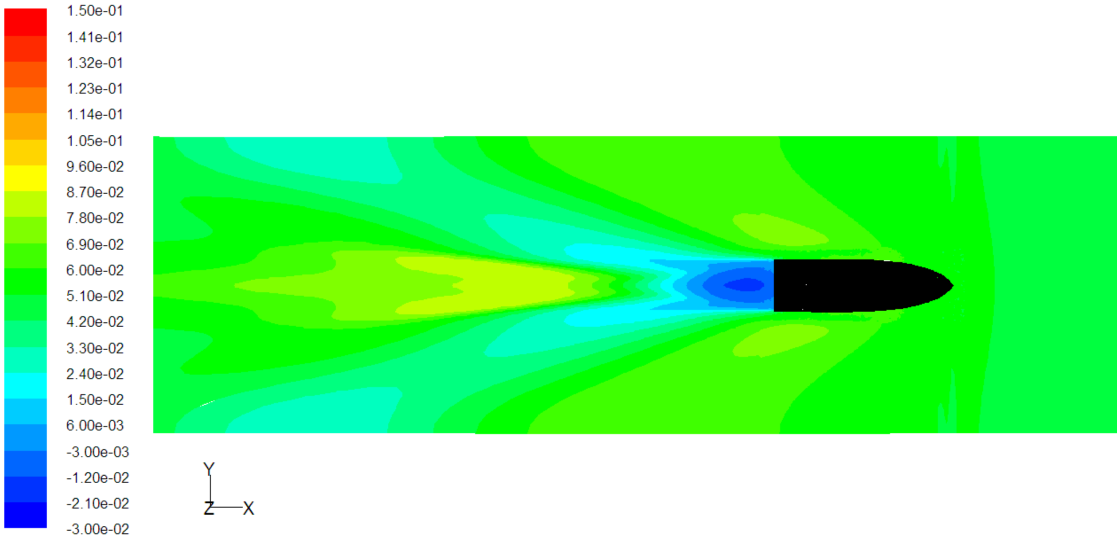

(e) U=4.08 m/s and Fr=1.2

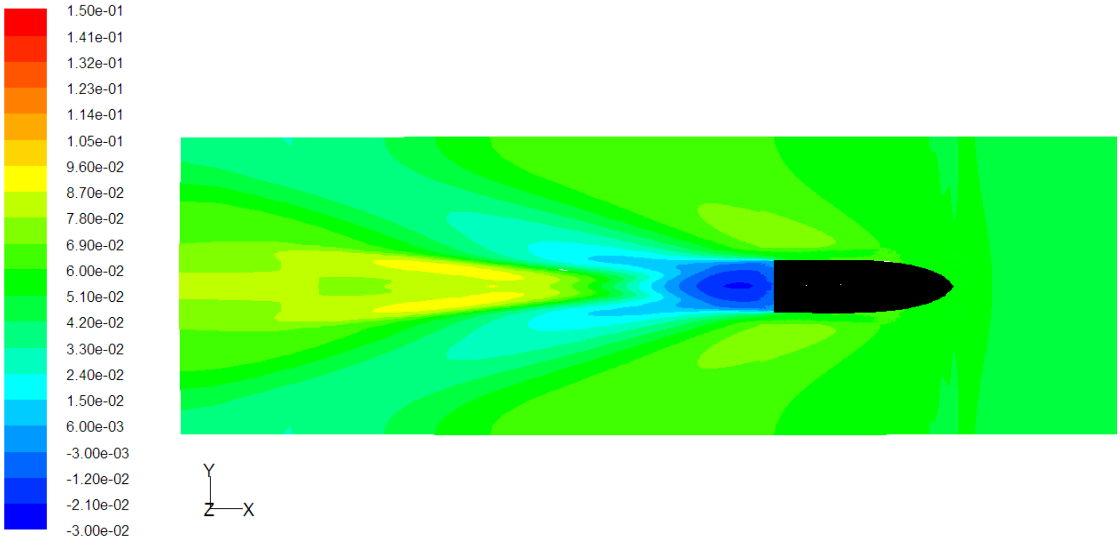

(f) U=4.39 m/s and Fr=1.3

Fig.8.6 The wave pattern due to the GHC at different Fr

One may also see from Fig.8.7 that in the cases with *Fr* >=1.0, the elevation curves are multi-valued curve. Near the middle ship section (right end of these curves), each specific location may have three different elevations. This is due to the occurrence of breaking waves, which are confirmed by the experiments.

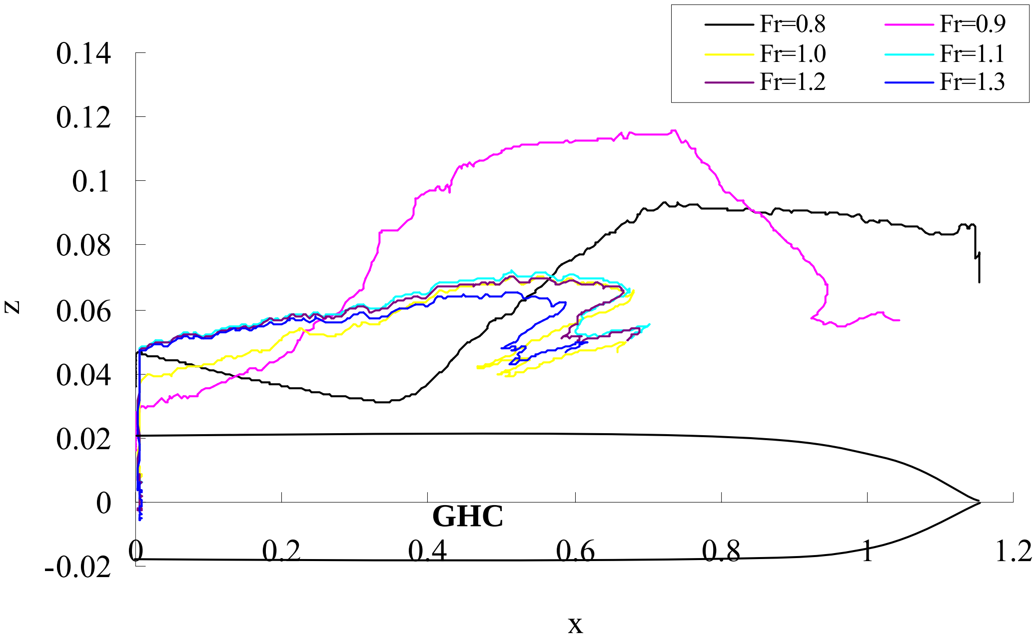

Fig.8.7 Wave elevation along the hull of GHC at different Froude number

From Fig. 8.6 and Fig8.7, it can also be observed that a wave trough occurs near the stern of the GHC. This spreads downstream with a decreasing spreading angle as *Fr* increases for the cases with *Fr*<=0.9. When *Fr*>0.9, there are no visual spreading of the wave trough observed in Fig. 8.6, instead, the trough is only shown in a relatively small area behind the stern with the minimum wave elevation increasing as *Fr* increases. Furthermore, one may find that the maximum wave elevations in the cases with *Fr*>=1.0 does not occur near the hull surface but in a region further downstream. The crest in such area spreads with decreasing spreading angle as F_r increases.

8.2.3 Pressure distribution around the hydrofoil

The pressure distribution on the hull surface as well as on the hydrofoil is essential for the design and analysis of the gliding-hydrofoil craft. Fig.8.7 shows the pressure coefficient distribution on the bottom of the central longitudinal plane for 7 navigation speeds, i.e. V_s=2.38, 2.72, 3.06, 3.4, 3.74, 4.08 and 4.39 m/s (or Fr=0.7, 0.8, 0.9, 1.0, 1.1, 1.2 and 1.3). x is the position relative to the stern of the hull and L is the length of the GHC. The pressure coefficient is defined by using Eq.(8.1)

$$C_P = \frac{P}{\frac{1}{2}\rho U^2} \tag{8.1}$$

where, P is the absolute pressure including both hydrodynamics and hydrostatics pressur es terms, U is the navigation speed

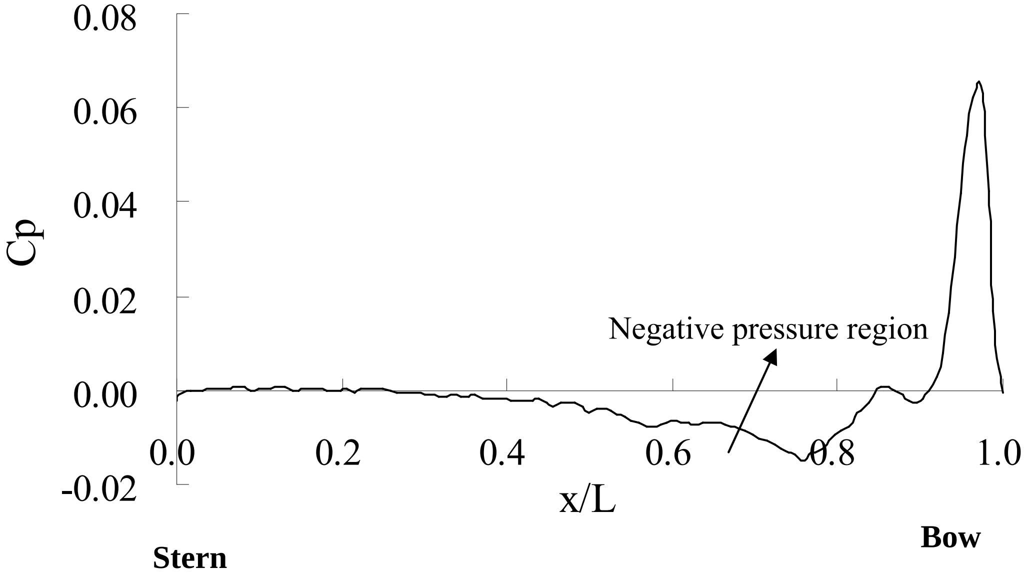

(a) U=2.38 m/s and Fr=0.7

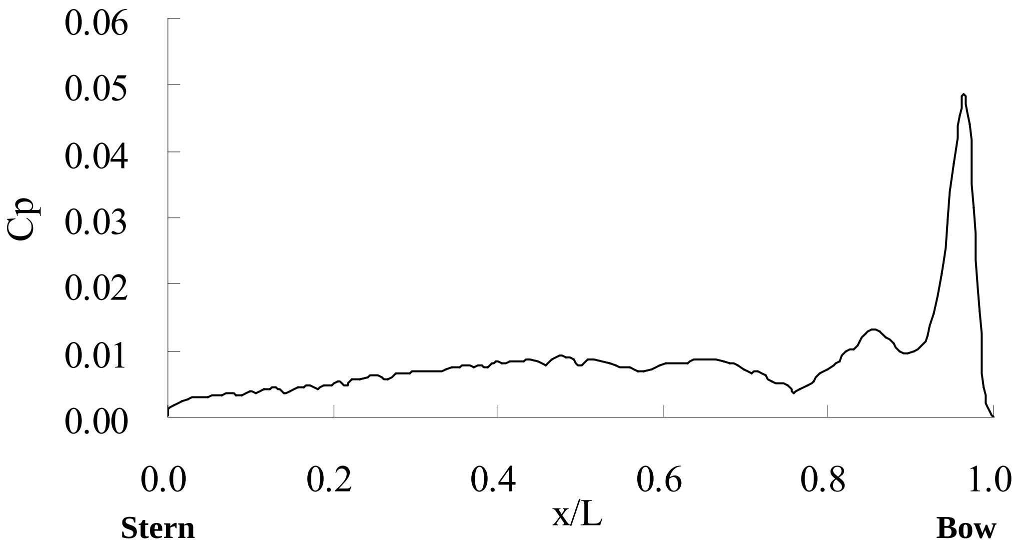

(b) U=2.72 m/s and Fr=0.8

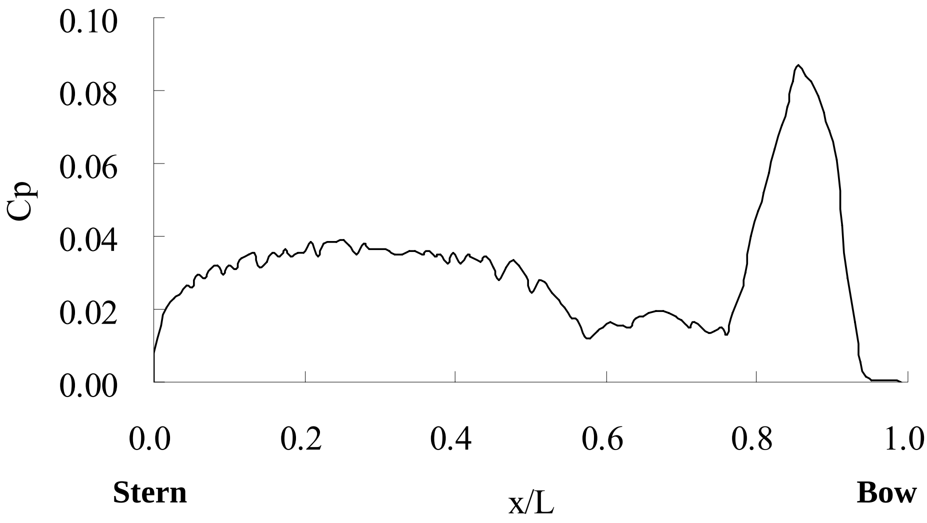

(c) U=3.06m/s and Fr=0.9

(d) U=3.4m/s and Fr=1.0

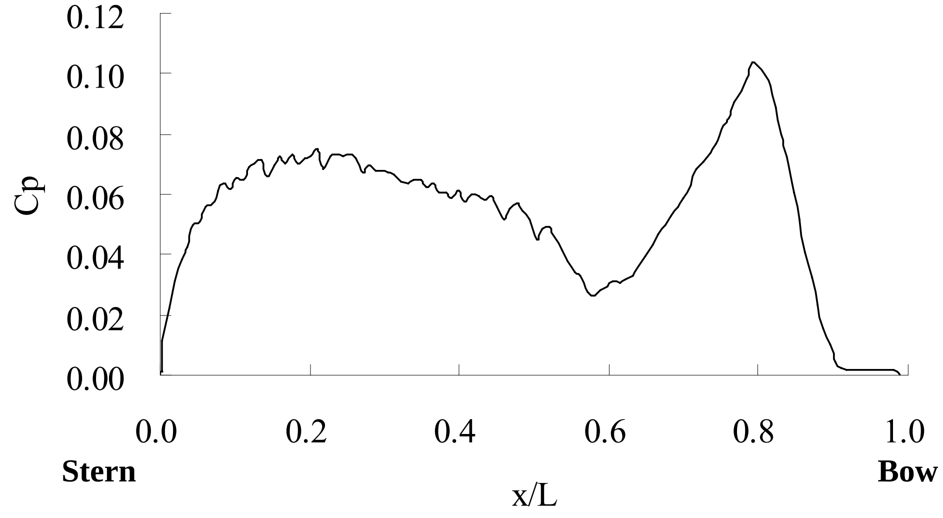

(e) U=3.74m/s and Fr=1.1

(f) *U*=4.08m/s and *Fr*=1.2

(g) *U*=4.39m/s and *Fr*=1.3

Fig.8.8 Distribution of pressure coefficient of the bottom of the hull at various *U*

Fig.8.8 shows that high pressure mostly occur in the bow part and low pressures in the stern part. Negative pressure is observed in a region near the location of the hydrofoil, i.e. 0.6*L* from the stern in case with low navigation speed (Fig.8.7a). That implies that the vertical load on the GHC may be downward and as a result the GHC may sink. This can also explain the phenomenon observed in the model test presented in Chapter 4, i.e., when the towing speed is lower than 2.72 the GHC model sinks in the water.

In Fig 8.8 (b) to (g) show that with the increase of U the pressure coefficient near stern increases. Near the position of x/L equal about 0.6 where the hydrofoil is installed, the pressure coefficient is lower than that in other positions. To further look at the details of the flow around the hydrofoil and the hull surface, the dynamic pressure distribution in such case is shown in Fig. 8.9. As expected, the dynamic pressure term, $\frac{1}{2}\rho|\bar{v}|^2$, is significantly high between the hydrofoil and the boundary layer on the bottom of the hull. This implies that the velocity is bigger at this area due to the presence of the hydrofoil. The increase of velocity leads to the decrease of the pressure at that position.

(a) $Fr = 0.7$

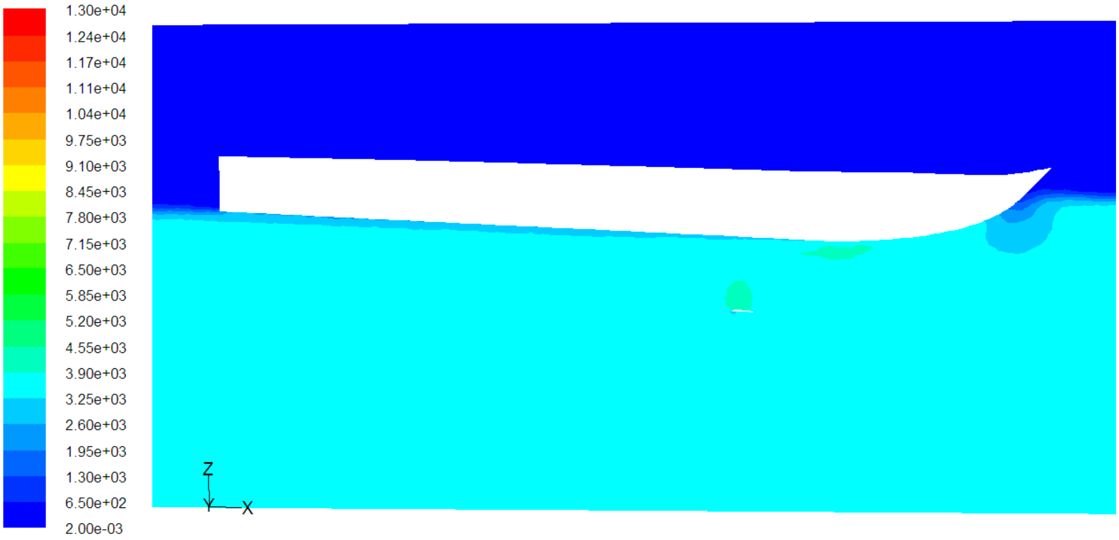

(b) Fr=0.8

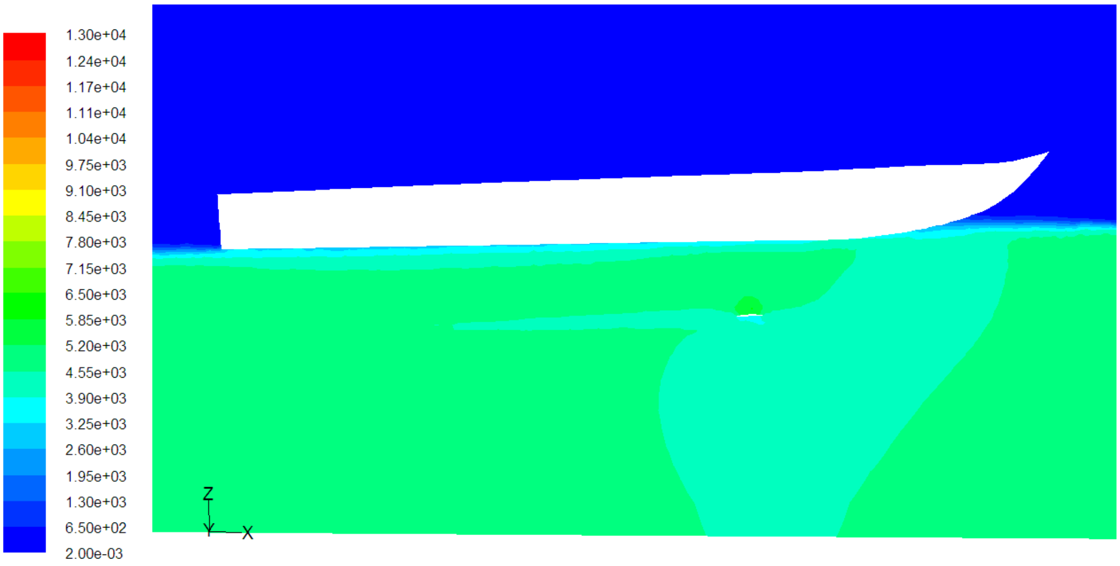

(c) *Fr*=0.9

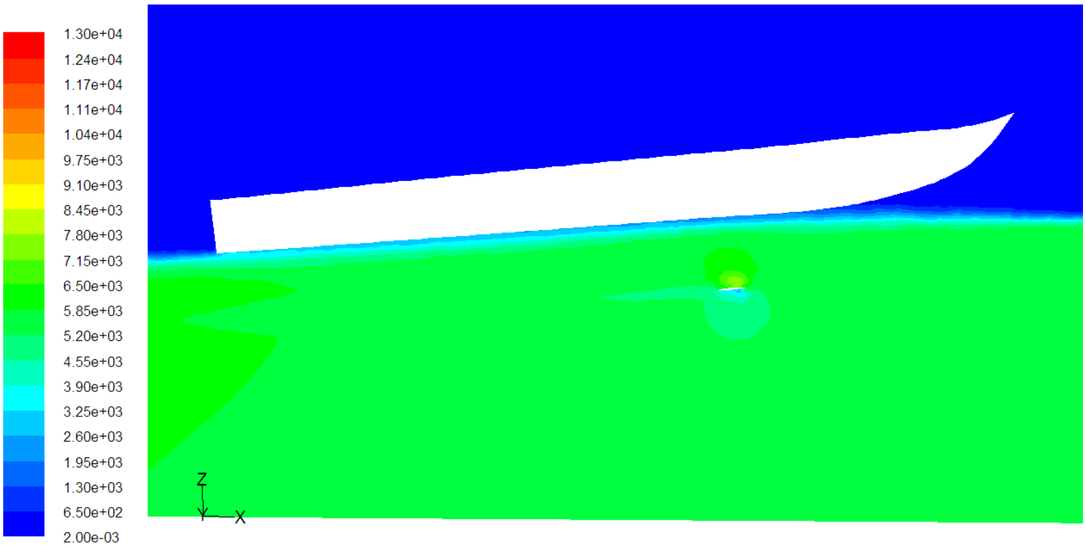

(d) *Fr*=1.0

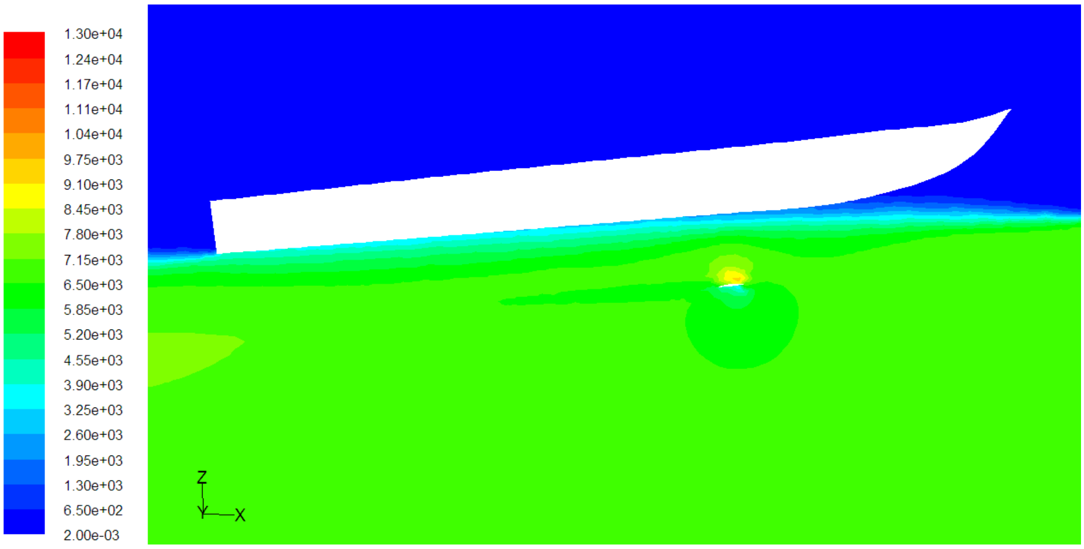

(e) *Fr*=1.1

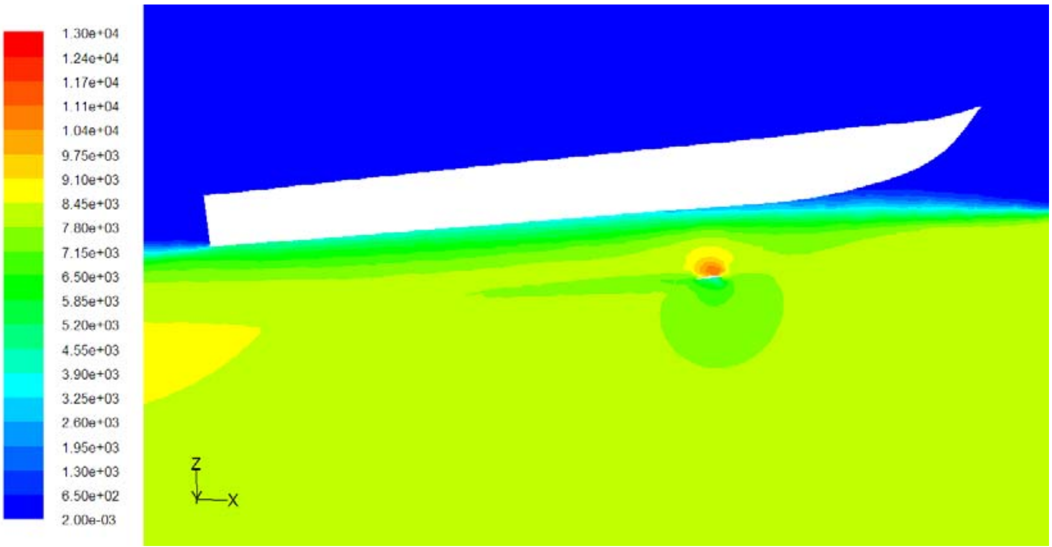

(f) *Fr*=1.2

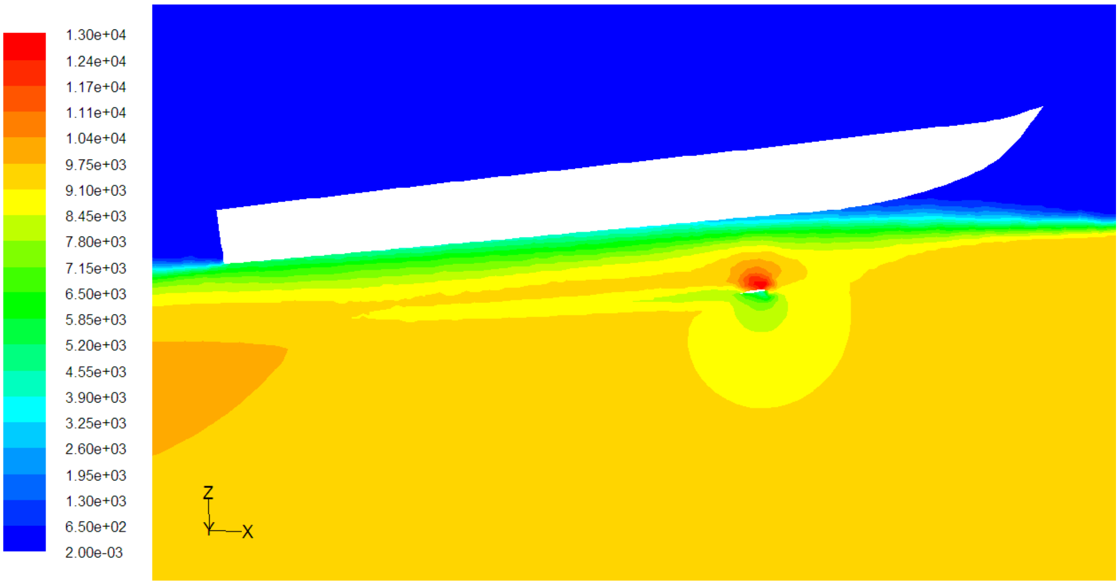

(g) *Fr*=1.3

Fig. 8.9 Dynamic pressure distribution at mid-ship section of the hull

8.3 Further investigation on hydrodynamic characteristics of gliding-hydrofoil craft in steady flow

The steady behaviour of a GHC on a straight course in calm water is determined by the trim moment, vertical and longitudinal force on the hull, draft and speed.

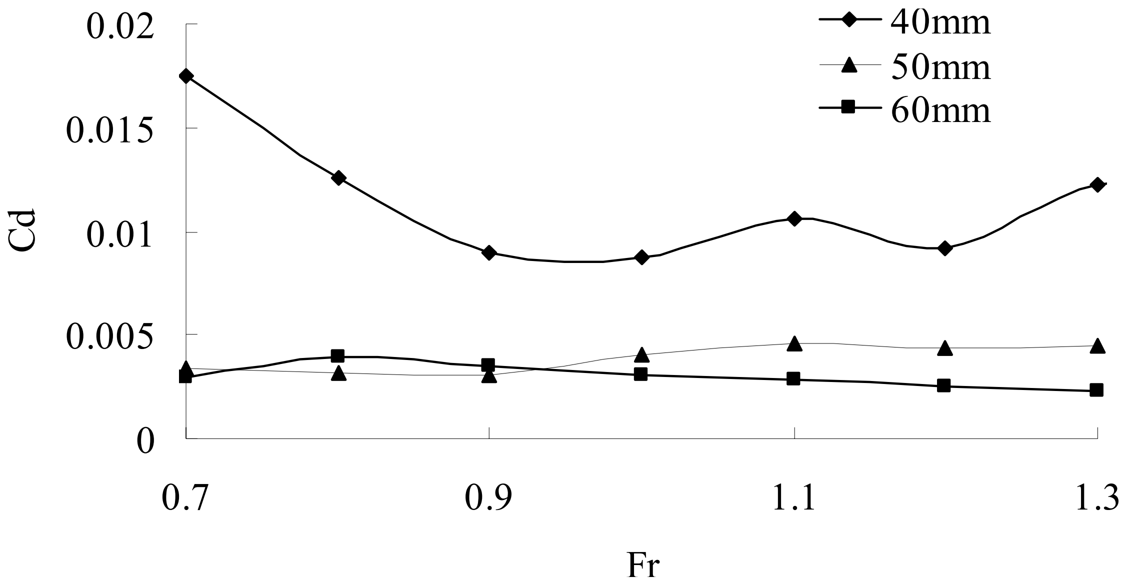

Fig.8.10 The comparison of resistance coefficient for submergences of 40mm, 50mm and 60mm

In the cases considered in this section, the computation grid is the same as that in Fig.8.3. The attack angle of the hydrofoil is kept as 0° and the same boundary condition and turbulence model are adopted to simulate them. The submergences of the hydrofoil range from 40mm to 60mm. The comparison of resistance coefficient for submergences of 40mm, 50mm and 60mm is given in Fig.8.10. From Fig.8.10 we can see that the resistance coefficient for submergence of 40mm is the biggest. And the resistance coefficients for submergence of 50mm and 60mm are very close.

9. HIGH-SPEED GLIDING-HYDROFOIL CRAFT IN UNSTEADY FLOW

In reality, the ship travelling in sea is general in unsteady state. Ship berthing, ship leaving the harbor, ship manoeuvrability and ship seakeeping, together with the unsteady free surface due to random wave, are all source of unsteady. This drives the importance of the research of hydrodynamic performance of GHC in unsteady flow. The numerical investigation of hydrodynamics characteristics of a gliding-hydrofoil craft under specific unsteady conditions will be studied in this section. Up until now, the relative research on the unsteady performance of GHC using experiments was not yet done. Only the CFD numerical simulation has been used to study the GHC unsteady performance. Three cases were considered. They are the transient procedure of ship berthing, ship leaving harbor and ship maneuvering with continuous change of incoming flow angles.

9.1 Craft motion model from $v=v_s$ to $v=0$

During berthing, the GHC usually moves laterally at a low but varying speed. Due to unsteady berthing motion of the ship, the hydrodynamic performance is quite different from that in steady state. To gain a clear insight into the hydrodynamic performance of a GHC during berthing, it is necessary to investigate the flow field around the berthing ship and the hydrodynamic forces acting on the hull. The outcome benefits the guidance to of ship berthing operation. For this purpose, the simulations are carried out with craft speed ranging from an initial speed of v_s to 0.

9.1.1 Computational domain

In this investigation, a Cartesian coordinate system fixed on the ship hull, as shown in Fig.9.1, is used. The plane yoz lies in the mid-ship section, the z -axis is pointing in the opposite direction of ship motion, the x-axis in the ship length direction and y-axis is pointing vertically downward. U is the velocity of water. The water depth is taking as 13 times draft of the craft. Tests indicate that the effect from the seabed can be ignored under such configuration. The details will not be given here.

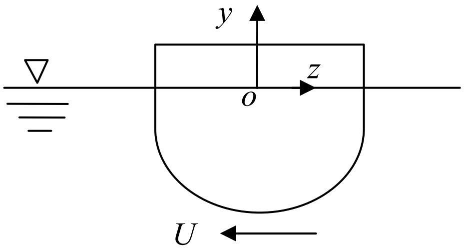

Fig.9.1 Coordinate system

In the harbor area, the incoming water waves are very small. Considering the fact that the velocity of the GHC is low and thus the radiation waves may also be ignored. Therefore, the free surface elevation under such conditions may be neglected and the free surface can be assumed to be undisturbed. Under this assumption, the air flow above the free surface does not need to be included in the simulation and thus single phase flow can be applied to reduce the computational cost. In the investigation, a rectangular computational domain is chosen, as sketched in Fig.9.2. The domain is bounded by the body surface on the GHC, the undisturbed free surface (Top surface) and the artificial boundaries including the both surface and 4 vertical walls. All these artificial boundaries are located sufficiently far away from the GHC to depress unexpected reflections from these boundaries. Necessary numerical tests have been carried out and suggested the size of the computational domain as given below. The details will not be presented here.

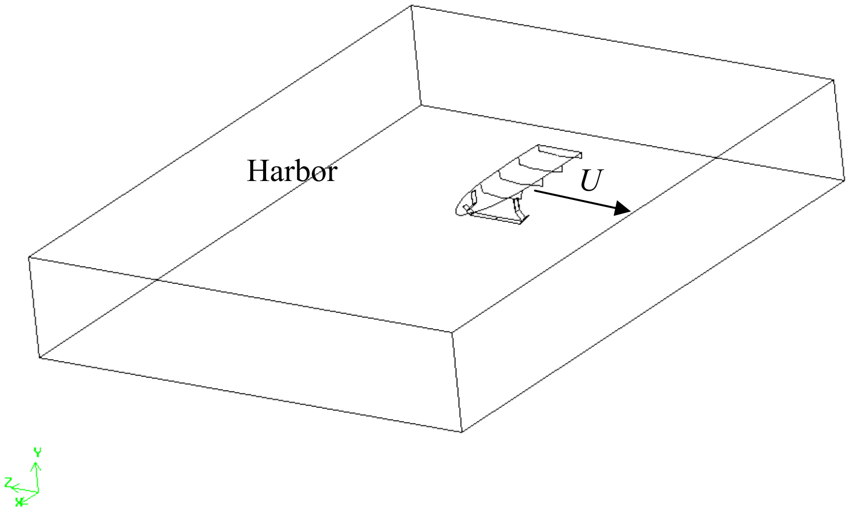

Fig.9.2 Computational domain

Table 9.1 Computational domain

	Scale
Length (Longitudinal direction x)	$-1.5 \le x/L \le 1.5$
Width (z)	$-3 \le z/B \le 7$
Depth (Vertical direction y)	$-9 \le y/D \le 0$

where L is the ship length, B is the ship breadth and D is the draft of the ship. The harbor is located in negative z direction with a distance to the center of gravity of the GHC of $3B$.

9.1.2 Boundary conditions and solution settings

The boundaries of the computational domain are categorized into inlet, outlet, fixed wall and symmetrical plane. In the numerical simulation, the body surface is treated as a fixed wall, the horizontal plane below the ship, the vertical planes in front of and behind the ship are treated as fixed wall; the vertical planes on the port side of the ship is treated as inlet surface. The vertical plane on the starboard side of the ship is as outlet. It should be noted under such configuration of inlet/outlet, the effect of the harbor wall is ignored.

As mentioned before, the free surface is assumed to be undisturbed and, therefore, the double-model theory is suitable to linearise the free surface. In the double-model theory, the free surface is suppressed by a mirror image source in order to make the free surface undisturbed. This is achieved by imposing a symmetrical boundary condition on the undisturbed free surface, It is worth noting that, for undisturbed free surface, the symmetrical boundary satisfies the kinematic free surface condition, i.e. normal velocity equals to zero, but violates the dynamic boundary condition at the water surface. For the problem involving a surface-piercing structure such as GHC in this paper, the double-model approach gives a spanwise bound vortex distribution that is symmetrical with respect to the undisturbed free surface implying that there will be no concentrated vortex at the symmetry plane. This also gives a right representation of the reality that no concentrated vortex is generated at the free surface since the pressure must be zero (dynamic boundary condition). This reality excludes the use of wall boundary condition which does not limit the concentrated vortex on it though the normal velocity on such wall is also zero. The double-model approach is widely used in CFD practices e.g. (Xie N, Vassalos D, 2006; Carl-Erik Janson; Office of Naval Research, 2000) to approximate the actual flow in cases that the waves are small to reduce the computational cost. It should also be noted that a pressure condition specifying atmospheric pressure (kinematic free surface boundary) is not suitable since it allows mass exchanging and therefore disobey dynamic free surface condition.

The grid generator GAMBIT is used to generate the computational grid. Figures 9.3 and 9.4 illustrate the partial view of the grids in the *yoz* plane and the *xoz* plane, respectively.

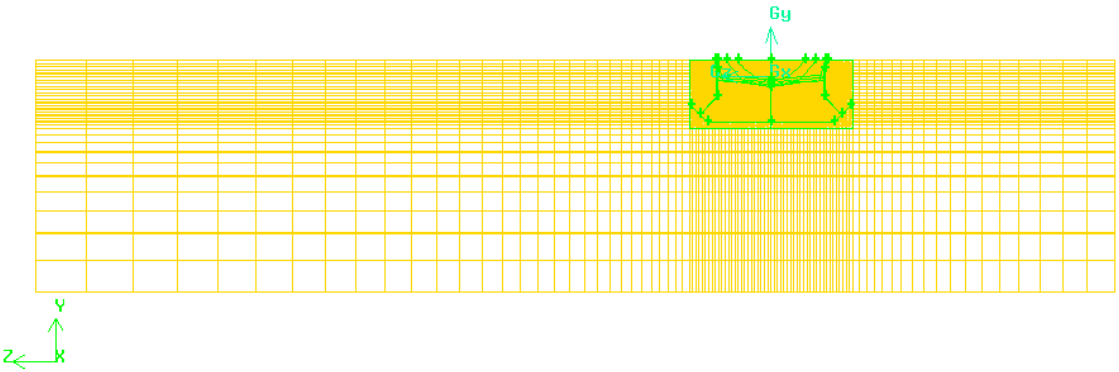

Fig.9.3 Partial view of grids in the *zoy* plane

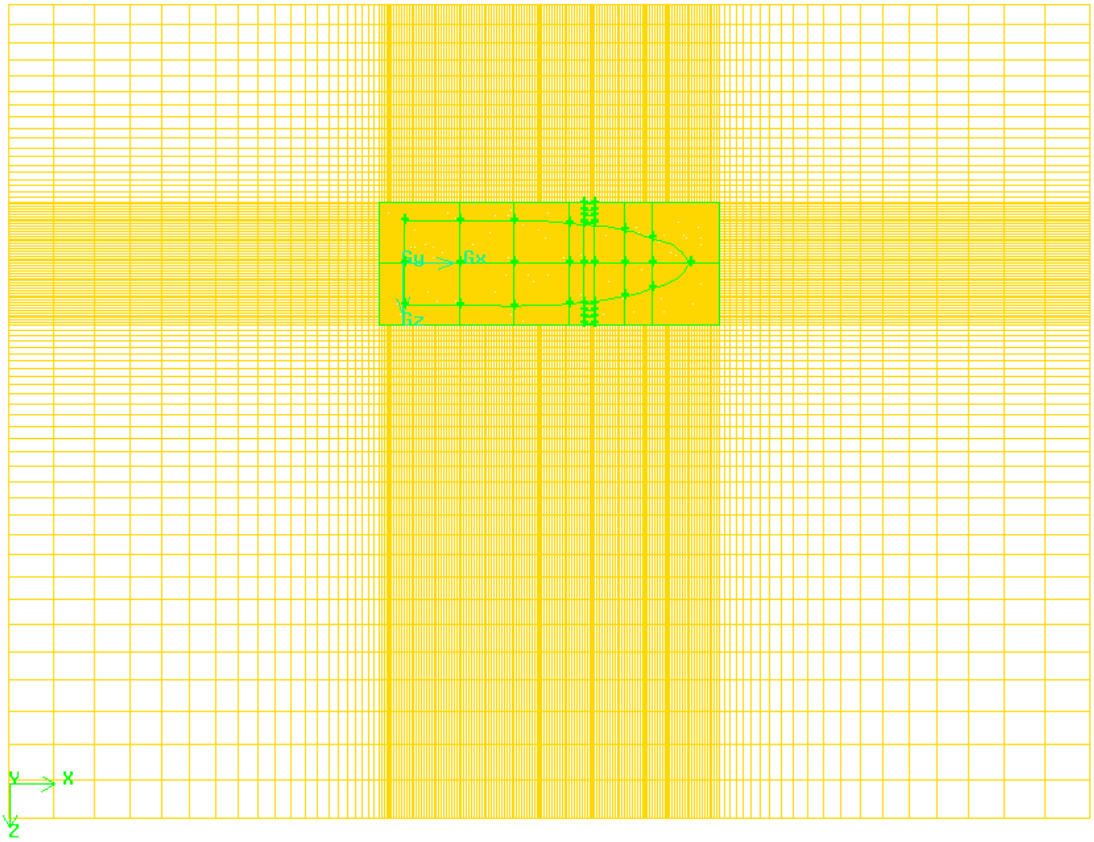

Fig.9.4 Partial view of grids in the *xoz* plane

The variation of ship speed against time is prescribed in Fig.9.5, where *U* is the hull speed, and *T* is time.

Since the coordinate system in the FLENT simulation is defined to follow the motion of the GHC, the change of the ship velocity is reflected by the change of the inlet velocity in the numerical simulation, which is achieved by using a user defined function (UDF).

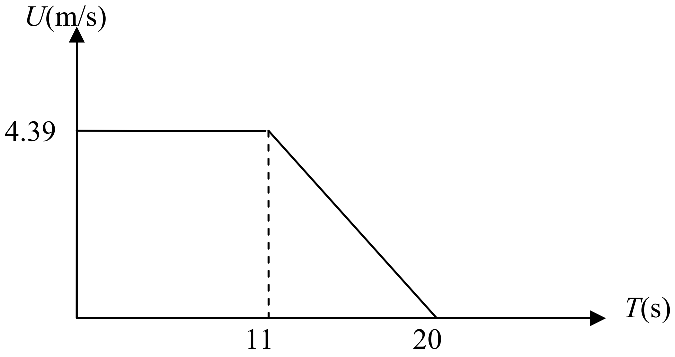

Fig.9.5 Ship speed changing with time

The unsteady formulation is discretized by the first-order implicit scheme, the SIMPLE algorithm is used for pressure-velocity coupling, momentum, turbulent kinetic energy and turbulent dissipation rate or specific dissipation rate equations are discretized by a second-order upwind differencing scheme. SST $k-\omega$ model is used to model the turbulence, similar to the investigations in previous chapters. The non-dimensional time interval per step is ΔT=0.005s, and iteration is performed 20 times at each time level.

9.1.3 Numerical results

The lateral resistance acting on the GHC model hull undergoing unsteady berthing in deep water are evaluated. The time histories of the resistance are shown in Fig.9.6 in dimensionless form (C_d) as defined by:

$$C_d = \frac{R_t}{\frac{1}{2}\rho U_0^2 S} \tag{9.1}$$

where U_0 is the initial velocity and R_t is the resistance. The same symbol as in the previous chapters is used here; the physical meaning is also same.

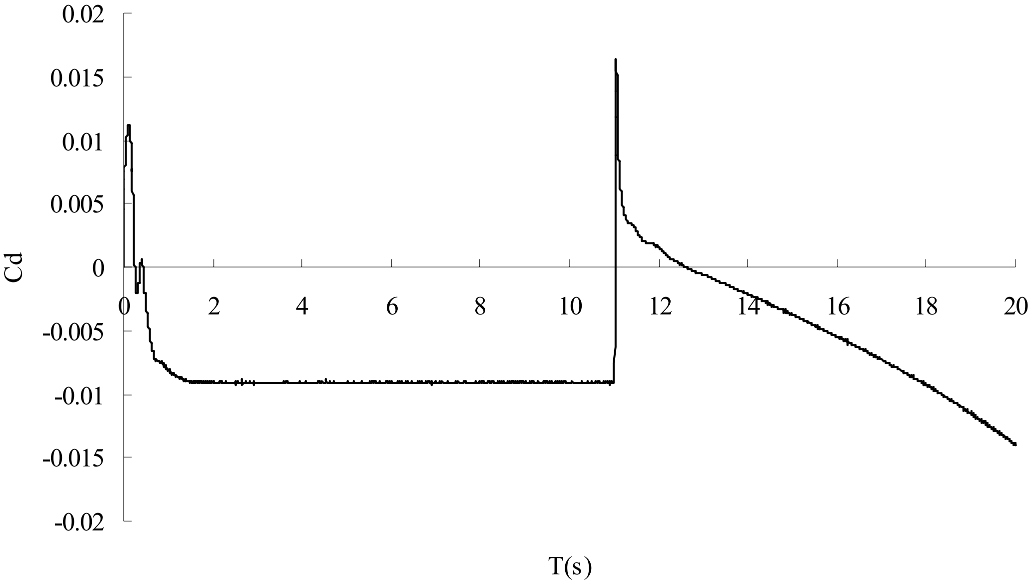

Fig.9.6 The time history of lateral hydrodynamic forces

Similar to the steady cases shown in previous chapters, a significant resistance coefficient with C_d larger than 0.01 is observed in the beginning and rapidly decreases to a steady value after T>2s. The change of the C_d in the beginning is due to the transient effect as discussed before. The steady C_d at T ranging from 2s to 11s reflects the resistance corresponding to a constant hull velocity before T = 11s.

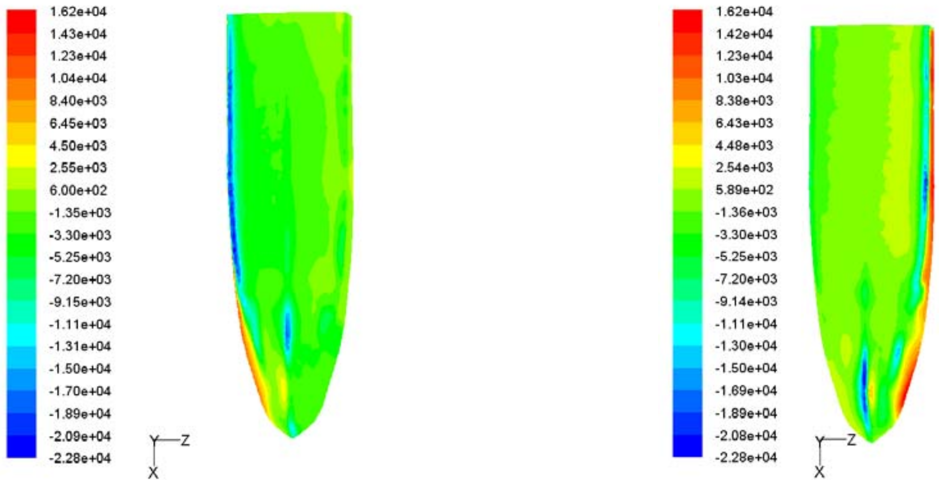

(a) Static pressure at T=10s

(b) Static pressure at T≈11s

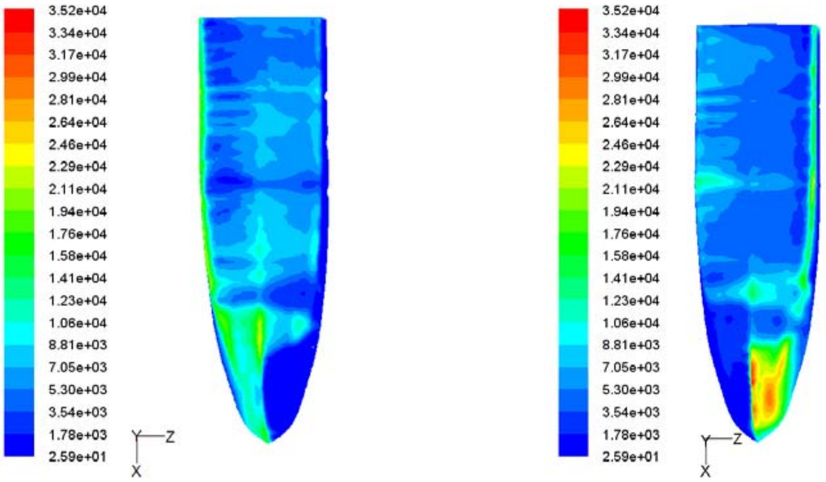

(c) Dynamic pressure at *T*=10s (d) Dynamic pressure at *T*≈11s

Fig. 9.7 Pressure distribution on the hull at different instants of the berthing

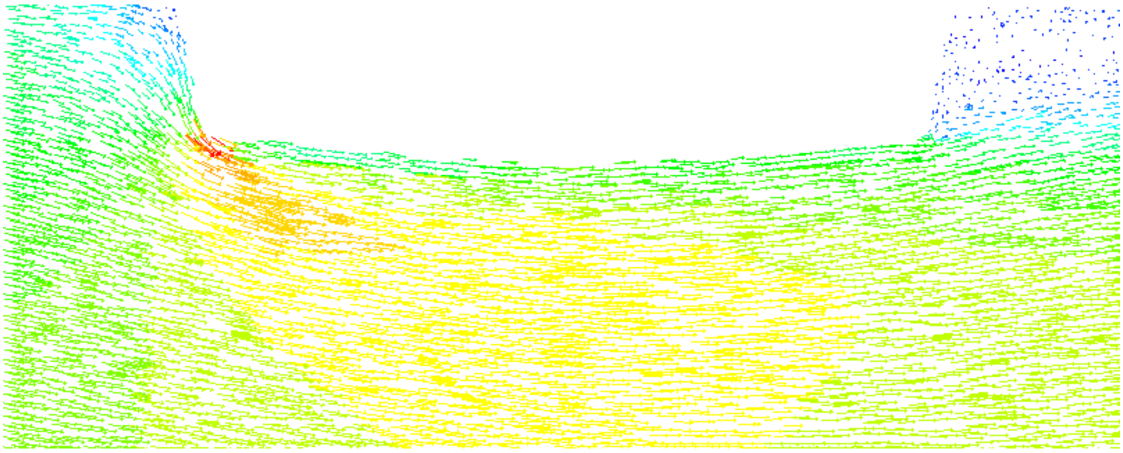

(a) *T*=10s

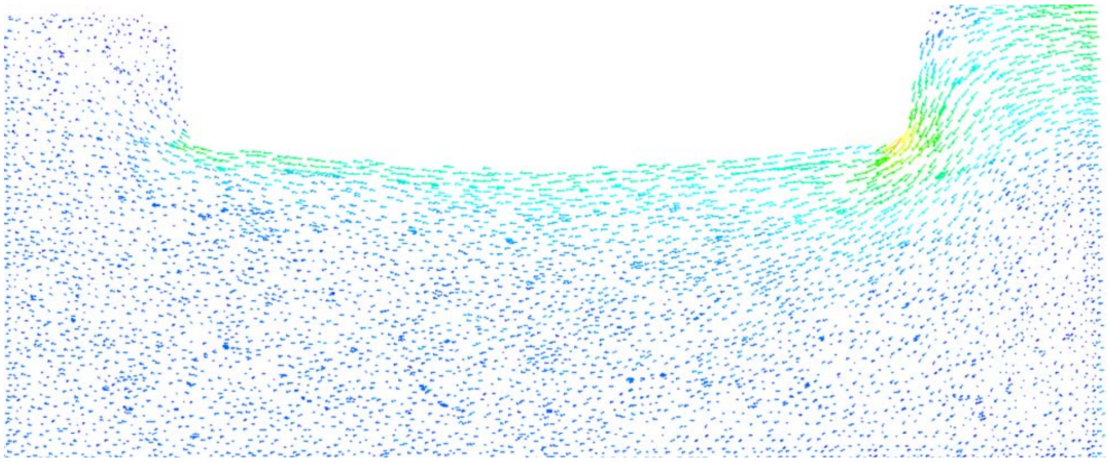

(b) *T*≈11s

Fig. 9.8 Velocity field near the mid-ship section of the hull at different instants of the berthing

From $T = 11$s, the hull velocity starts decreasing with a constant acceleration, -0.488m/s^2. The sudden increase in the hydrodynamic force includes both the transient effects as well as occurrence of a non-zero added mass term. It is also found that the hydrodynamic forces in the beginning of the berthing follow the direction of the motion (the value is positive) implying a resistance to the reduction of the hull speed. The corresponding pressure distributions and the velocity field near the hull at such instants are shown in Fig. 9.7 and Fig. 9.8 respectively. From Fig. 9.7, it is found that at the beginning of the berthing, i.e. $T = 11$s, both the dynamic pressure and the static pressure show a different pattern from those at a quasi-steady state before $T = 11$s (e.g. Fig. 9.7(a) and (c)). Particularly, at $T = 11$s, a significantly high pressure area occurs near the wind side (right side) of the hull; whereas it occurs near the left bow area at $T = 10$s. The analysis of the velocity field near the hull (Fig. 9.8) indicates that the velocity direction changes at the beginning of the berthing (Fig. 9.8b), leading to a change at the direction of the momentum. As a result, a significant force impulse occurs at $T = 11$s (Fig. 9.6).

After $T = 11$s, the transient effect is expected to disappear in short time but the force related to added mass sustains from 11-20. The term related to added mass and other dynamic effects related significantly increase the resistance. For example, at T=16s, the hull velocity is 2.44 m/s, the resistance coefficient at steady state is around 0.008 from the numerical simulation, corresponding to 0.025 for the dimensionless force using Eq.(9.1), but in this case, the dimensionless force at $T = 16$s is 0.005. This implies that for the hull with unsteady speed, the resistance are significantly affected by the acceleration procedure and therefore cannot be evaluated by using the resistance coefficients from the steady studies. The acceleration procedure of the hull also differs from the feature of the pressure distribution and velocity fields during berthing procedure from that in the steady state. Some examples are illustrated in Fig.9.9. As can be observed, during the berthing the feature of the pressure distribution on the hull and the velocity field near the hull are similar to those at the beginning of the berthing but different from those at the steady state, i.e. $T < 11$s. It should be noted that though a significant high pressure area locates on the right side, the hydrodynamic force, which is obtained by integrating pressure over the entire hull, points from left to right, the same as that at the steady state, i.e. $T < 11$s.

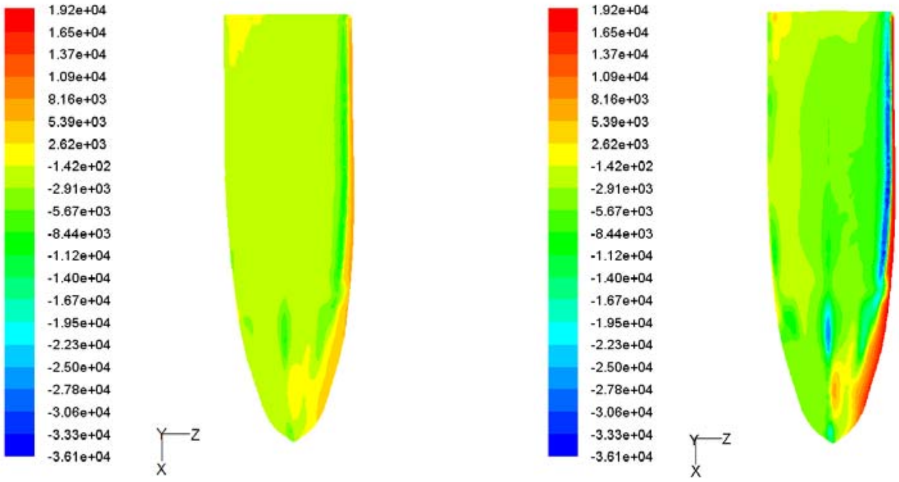

(a) Static pressure at *T*=15s (b) Static pressure at *T*=20s

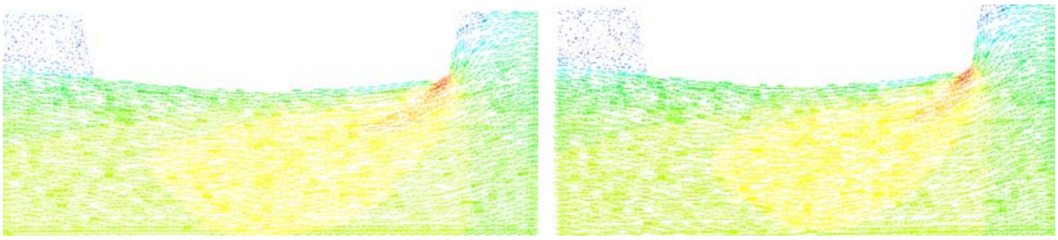

(c) Velocity field at *T*=15s (d) Velocity field at *T*=20s

Fig. 9.9 Pressure distribution on the hull and Velocity field near the mid-ship section of the hull at different instants of the berthing

The added mass term and other unsteady effect also explain that at T = 20s when U =0, there is still significant hydrodynamic forces. The numerical simulation continues after T=20, a continuous drop of dimensionless force is observed before it becomes zero eventually. Again, this may be explained by the transient effects due to which the fluid field remains unsteady before it is settled at rest.

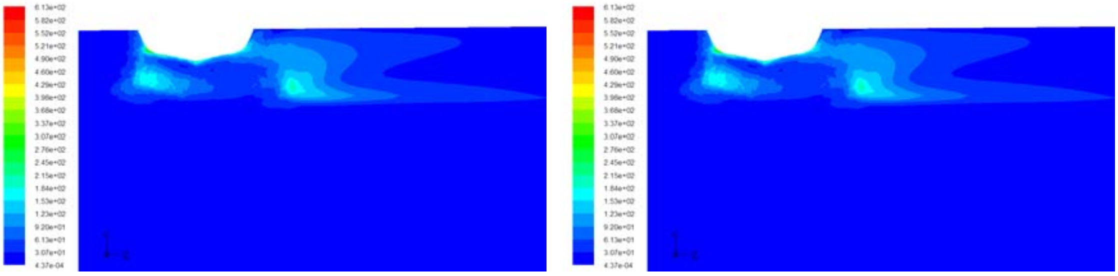

(a) *T*=10s (b) *T*≈11s

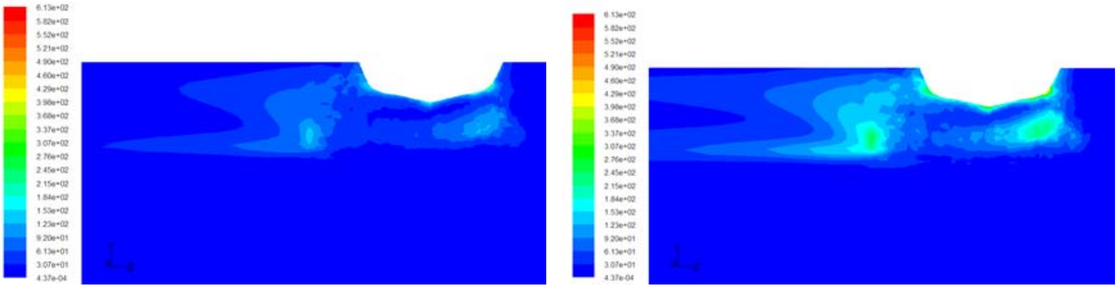

(c) T=15s (d) T=20s

Fig.9.10 The vorticity distribution in the *yoz* plane (x=0.8)

The vorticity distributions in the *yoz* plane are displayed in Fig.9.10. From these two figures, it can be clearly observed that the vortices at the sides and the keel are generated and grow up as the ship moving. The vortices move obviously due to the change of acceleration around T=11s from the steady state before T=10s. From short transient period, when T=15 to T=18, the area centred by positive vorticity transfer from left side to right size and the strength is enhanced. Again, significant difference in the feature of the vorticity distribution at the berthing procedure from that at the steady state before T=10s are observed. These confirm the necessity of the studies on unsteady cases.

9.2 Craft motion model from U=0 to v=v_s

In order to simulate the procedure that the craft leaves the harbor as sketched in Fig.9.11, a similar configuration of the case shown in previous sub-section is presented here. Similar to the ship berthing, the velocity of the hull in such a case is also very small and, therefore, the wave effects can be ignored. The computational domain, the boundary condition and the approach to deal with free surface boundary are the same as above. The only differences are (1) the direction of the hull velocity is reversed as illustrated in Fig.9.12 and that the speed of the hull now increases from U=0 to U= v_s. For simplification, a constant acceleration is given and the velocity can be described by Fig.9.13.

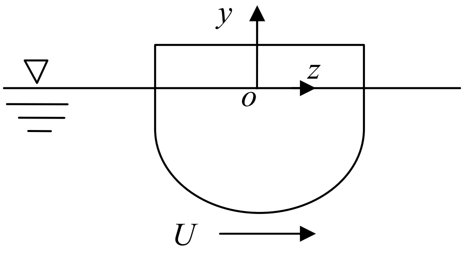

Fig.9.11 Coordinate system

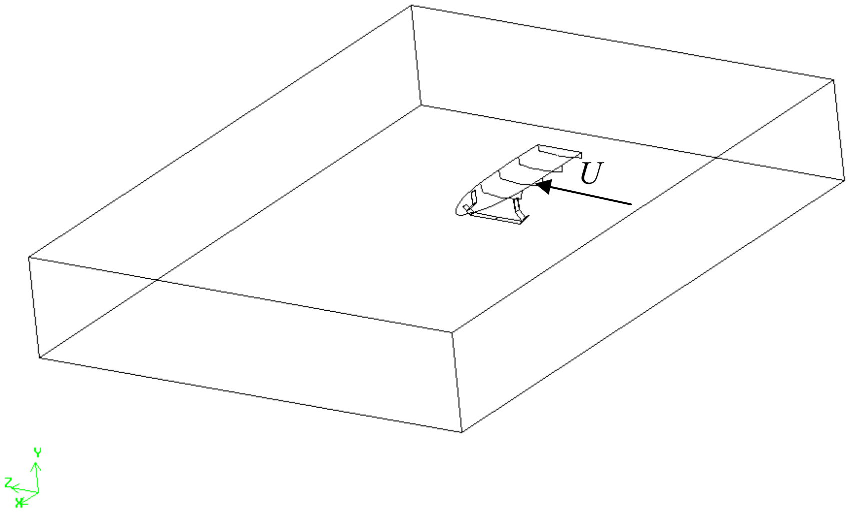

Fig.9.12 Computational domain of ship leaving harbour

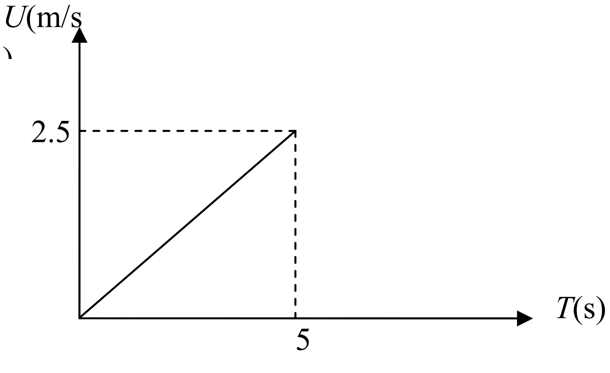

Fig.9.13 Ship speed changing with time

The dimensionless hydrodynamic forces acting on the GHC model hull undergoing unsteady leaving harbor in deep water are evaluated and the time histories are shown in Fig.9.14. It should be noted that the results shown Fig. 9.14 are negative if the direction of the force follows the direction of the shop motion but negative otherwise. A significant difference between this case and the case with ship berthing is that a sudden change of the dimensionless force is not found in Fig. 9.14. From this figure, one may also find that in the beginning of the acceleration procedure, the hydrodynamic force is in the opposite direction of the ship motion, it reaches maximum at $T \approx 1.75$s. The hydrodynamic decreases and changes its direction at $T \approx 2.75$s. After that, it increases up to $T = 5$s. (which happens after T=5s). This implies that at the later portion of the acceleration, the hydrodynamic force imposes an effect which trends to accelerate the hull.

Fig.9.14 The time history of lateral hydrodynamic forces

The pressure distribution on the hull surface and the velocity field of the flow around the hull are displayed at the characteristic time (T=1, 3, 5). Fig.9.15 shows the pressure distributions on the hull surface. It can be seen clearly that the pressure on the wind side of the hull at T=1 is larger than that on the lee side, leading to a force in the opposite direction of the ship motion. However, for T = 3s and T=5s, the pressure is distributed in a reversed pattern, leading to a hydrodynamic force follows the motion of the hull. Figure 9.16 shows the velocity fields at mid-ship plane and the corresponding vorticity distributions are shown in Fig. 9.17. These figures show that as the hull speed increases the vorticity on the left side of the hull becomes stronger and that on the right side remains at a similar strength. The wake area behind the hull also show a similar pattern after $T = 3$s.

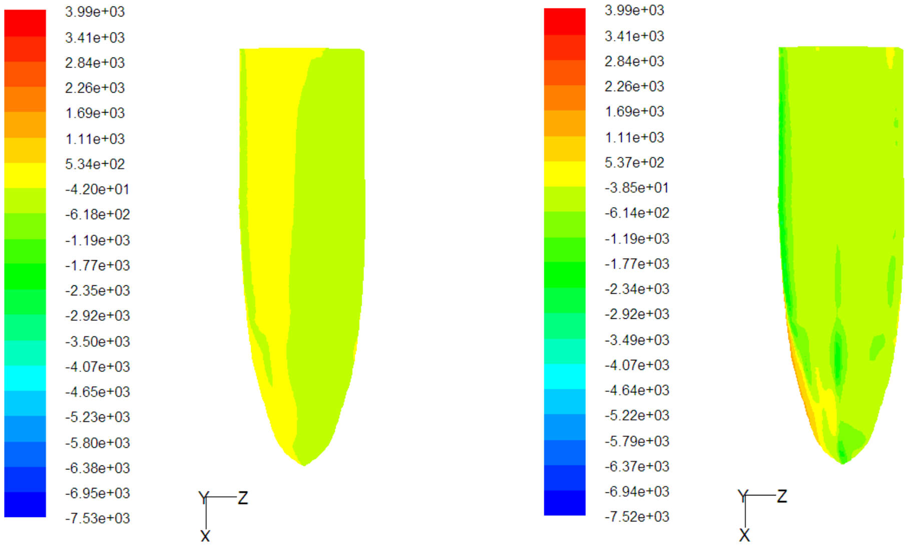

(a) T=1s (b) T=3s

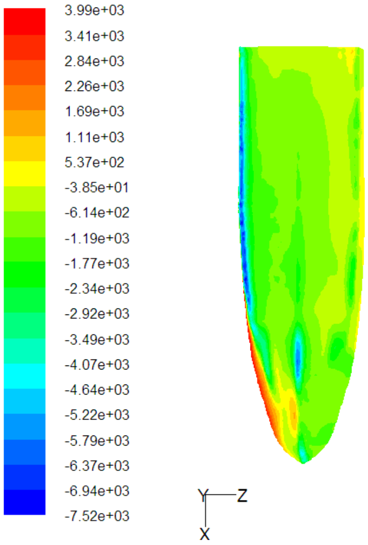

(c) T=5s

Fig.9.15 Pressure distribution on the hull surface

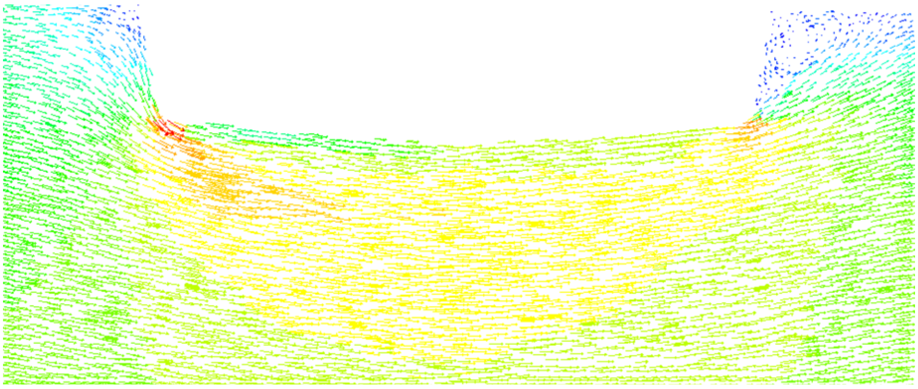

(a) *T*=1s

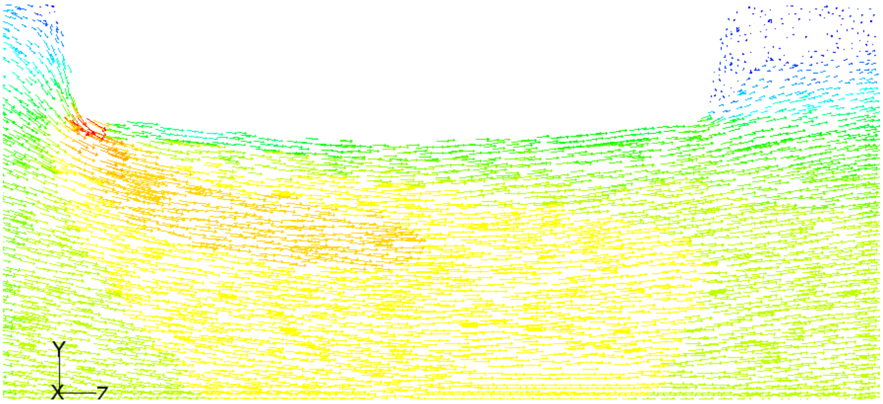

(b) *T*=3s

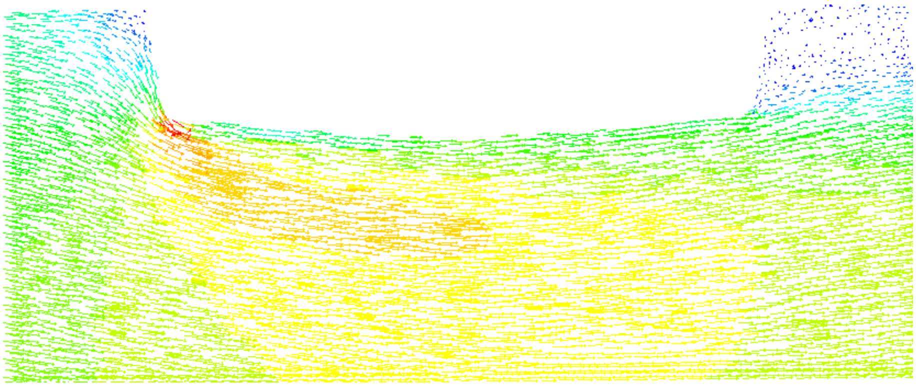

(c) *T*=5s

Fig.9.16 Instantaneous streamlines in the *z*=0.5 plane

(a) *T*=1s

(b) *T*=3s

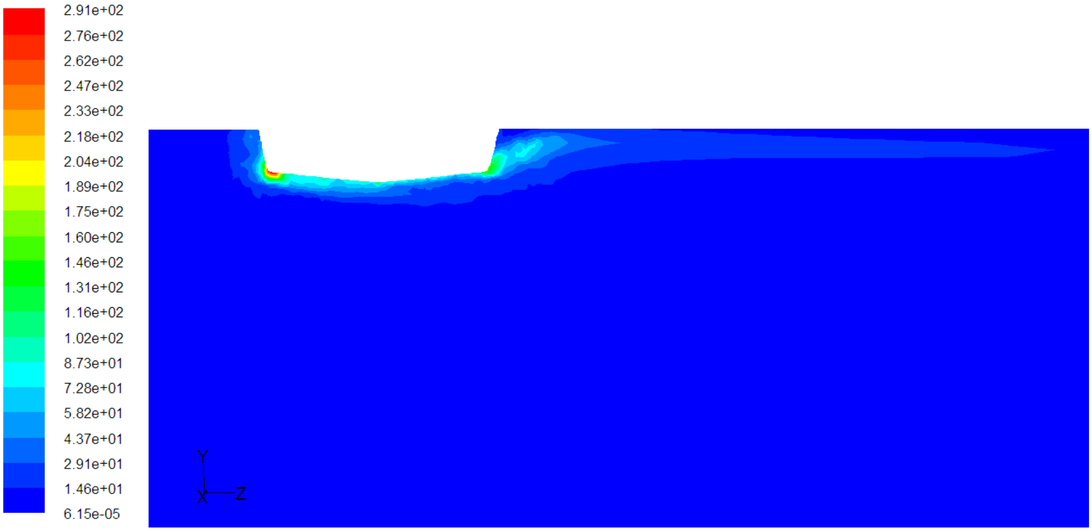

(c) *T*=5s

Fig.9.17 The vorticity distribution in the *yoz* plane(*x*=0.6)

9.3 Gliding-hydrofoil craft with continuous change of incoming flow angle

GHC, similar to all other crafts, does not always maintain a straight line in real navigation. There is a high possibility for the hull to change the direction and rotate itself. Due to the high speed of GHC, the flow field around the hull and the wet surface of the hull change as the direction changes. All of these will affect the hydrodynamic performance of GHC.

Obviously, the results from this case, particularly the hydrodynamic force, is opposite to the results with steady state simulation, which always leads to a resistance in the opposite direction of the ship motion. The pressure distribution, velocity and vorticity fields also indicate the dynamic effects. It clearly demonstrates the importance of the dynamic effects on the ship dynamics and therefore calls for more detailed unsteady simulations.

9.3.1 Calculation model and domain

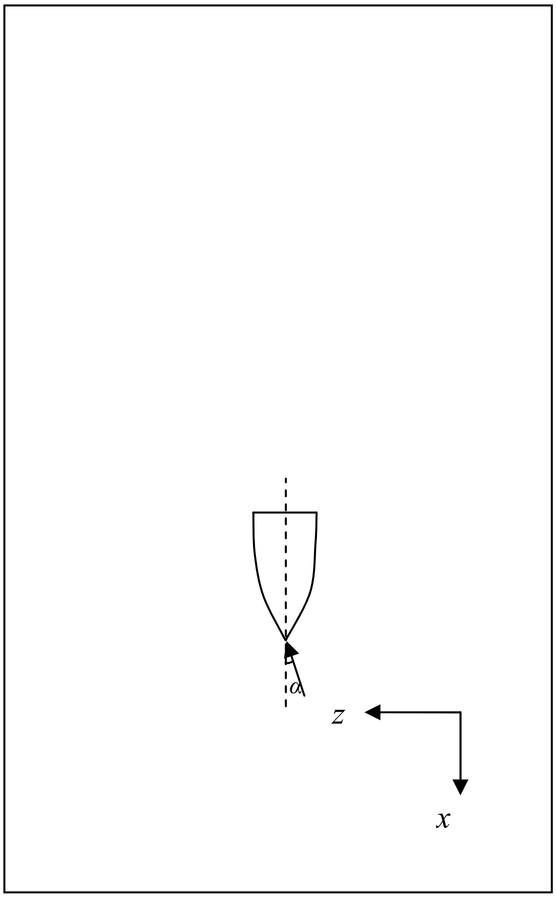

Fig.9.18 The direction of the incoming flow

In this section the angle of incoming flow is changed to analyse the procedure for a GHC turning its navigation direction, using the same body fixed coordinate system as in Section 9.1 and Fig. 9.2. The direction of the incoming flow is shown in Fig.9.18, α is the angle of the incoming flow, which changes up to 15^{o}. The boundary conditions and solution settings are the same as the section 9.1. The Froude number is 1.0, typical value for the GHC in take-off status. The range of the computational domain in the x direction, see Fig.9.17, is given by $-7 \le x/L \le 1$. The range of domain in the z direction is given by $-3.5 \le z/B \le 3.5$ .The range of domain in y direction $-10 \le y/D \le 10$ is chosen for computation.

9.3.2 Numerical results

It should be noted that for such a case, the wave pattern is important and therefore two-phase flow considering both the water and the air is used in order to investigate the wave pattern. To model the change of the direction of the inflow, the inlet and outlet of the domain are carefully changed during the simulation using UDF. All other configurations are the same as those in the previous two cases.

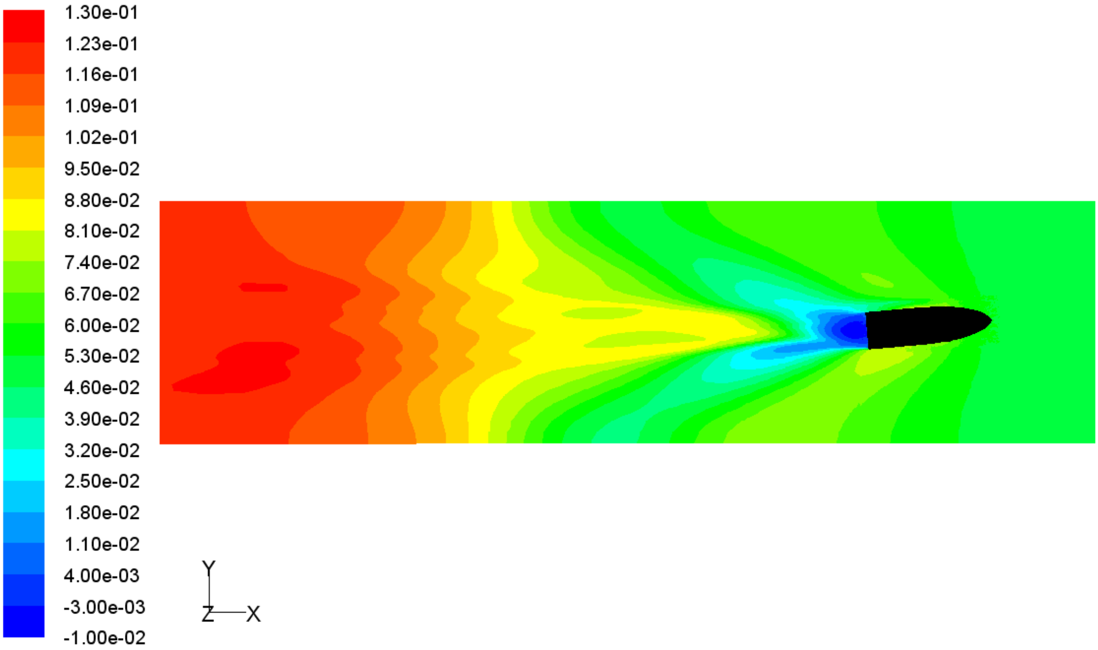

(a) α=5°

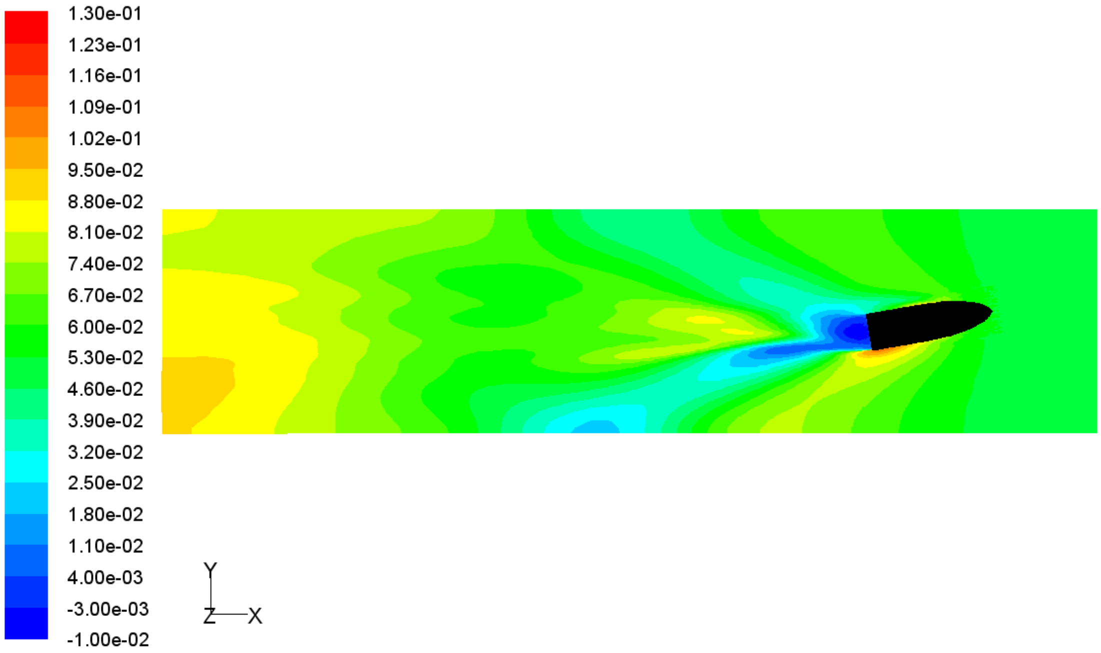

(b) α=10°

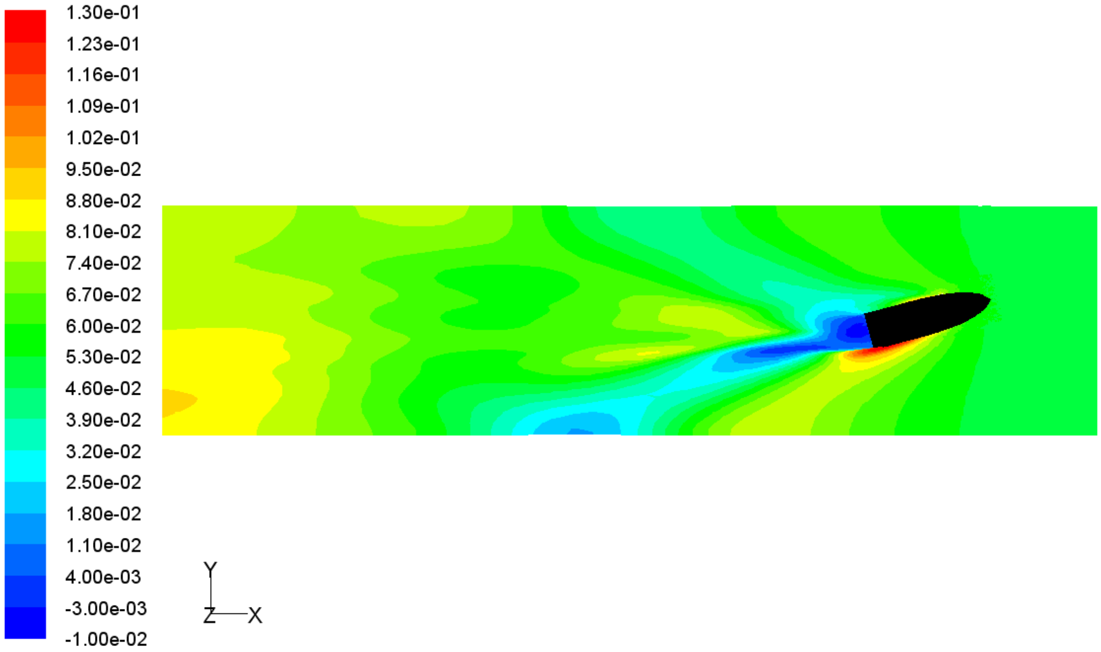

(c) α=15°

Fig. 9.19 Wave pattern of GHC at different drift angles

Gliding-hydrofoil craft with continuous change of incoming flow angle are evaluated Fig.9.19 is the wave pattern of GHC at drift angles 5°, 10° and 15°. As expected, the wave pattern becomes symmetrical about the longitudinal axis of the hull due to the change of the drift angles. Again, such phenomena cannot be observed in steady simulation, at port of GHC, a significant high wave elevation is observed in Fig. 9.19(b) and (c). It reflects the reality in which a splash is always observed in the outer surface of the rotation (port side in a case shown above).

Overall, from the above three preliminary investigations, one may draw a conclusion that the dynamic procedures, which are commonly seen in reality, cannot be predicted using the hydrodynamic performances of the GHC in steady state. The dynamic effects are significant. Considering that the main purpose of this work is on the experimental and numerical studies of the GHC hulls, the hull performance and related hydrodynamic features in steady state are the main focus. The studies presented in this chapter are to demonstrate the importance of the dynamic effects and initiate the research interest in studying the hydrodynamic feature for unsteady procedures. A detailed investigation is not presented here.

10. CONCLUSIONS AND RECOMMENDATIONS

In this thesis, the hydrodynamic features of a new high-speed ship, Gliding-Hydrofoil Craft(GHC), has been studied by both model tests (experiments) and numerical simulation. The work developed the main conclusions and recommendations for future studies are summarized in this chapter.

10.1 Summary and conclusions

Model tests are carried out in a towing tank, and the total resistance, trim angle and wetted area of the high-speed crafts are studied. For the purpose of comparison, the model tests start with a craft without the hydrofoil (a planing hull) in order to identify the effects of the hydrofoil in improving the performance. The experiments on the planning hull demonstrate the change of the wetted surface and R_e in cases with different Froude numbers. It is found that the resistance coefficient for the planing hull reaches minimum value at the design speed, i.e. Fr=1.3, but the trim angle follows a reversed trend to the resistance coefficient. The comparison between the experimental results and the empirical equation (Savitsky, 1964), which are most commonly used formula, shows a significant difference both in the resistance coefficient (~50% at low and high Froude number) and the trim angle (~90% at low Froude number, ~50% at the design speed). This implies that the empirical equations may not provide reasonable approximation to high-speed craft. A more detailed experimental investigation on the hydrodynamic feature of the GHC has been carried out for GHC in steady state with different Froude numbers ranging from 0.7 to 1.4. In this investigation, different submerged depth (model scale varies from 40mm to 60mm) and different initial attach angles (0 and -2^o) of hydrofoil are considered in order to optimize the design. Both the trim angle and the resistance coefficient have been measured. The current experimental data suggest that both the local viscous resistance and the effects from the wave generated by the moving hulls contribute to the resistance force. When the difference between the trim angles is smaller than 2^o, the wave effects may be the majority and thus the resistance coefficient decreases or increases following the increase of Hs; otherwise, it is necessary to consider both the wave effects and the viscous resistance. It also clearly demonstrates that both the submerged depth and the initial attack angle of the hydrofoil can significant influence the resistance force and thus the performance of the GHC. The comparison between the GHC and the planing hull indicates that hydrofoil of the GHC increases the resistance when the ship is smaller but decreases the resistance at the design speed, corresponding to $F_r > 1.3$; it also stabilize the hull at high speed, through the analysis of the trim angle at different Froude numbers, i.e. the trim angle of the GHC becomes quasi constant when F_r >1.0, but such phenomena is not observed in the experiments for a planing hull. Such comparison confirms the superiority of the GHC over a planing at design speed. Nevertheless, it is worth noting that in order to achieve good performance of a GHC, the submerged depth and the initial attack angle of the hydrofoil should be carefully selected.

Considering the fact that the model tests cannot provide detailed pressure\velocity fields around the hulls, a numerical investigation is also carried out to support the observations. In this work, the FLUENT software has been chosen for numerically investigating the hydrodynamics associated with the GHC. However, because it has never been applied to this kind of craft before, the convergence properties in terms of mesh, the turbulence models and the accuracy are carefully investigated before being applied to GHC. For this purpose, 2D investigations on the hydrodynamic feature of a NACA4412 hydrofoil beneath the free surface and 3D investigations on a Wigley Hull travelling in sea are carried out. The result indicates that if sufficient small mesh size (e.g. $\Delta l = 0.008$) is used, the pressure distribution and water lines around the structure, wave pattern and the resistance coefficients can be evaluated by using the software with acceptable accuracy. It also justifies that the SST $k-\omega$ turbulent model is the best choice for the problems addressed in this thesis

Further investigation on the accuracy of the Fluent is also carried out by using the cases measured in the model tests, including those with planing hull and GHC. For a planing hull in steady state with different navigation speeds, the resistance coefficients are compared with the experimental data and an acceptable agreement has been achieved. In addition, the green water occurrence observed in the experiments is also reproduced by using the FLUENT. These confirm the suitability and the sufficient accuracy of the FLUENT. Because the high-speed craft is travelling in open sea with deeper water depth that the towing tank used in the experiments and the numerical investigations, the effects of the tank size on the hydrodynamic feature of the hull is also investigated preliminarily. The results demonstrated the reflection waves from the side walls and their effects on the wave pattern around the hull. This calls for further numerical investigations on the high speed hulls in a tank with larger sizes to avoid the reflection from the side wall in order to approximate the real navigation situation. Numerical investigation on the GHC travelling with steady velocity is also carried out. Again, the comparison with the experimental data demonstrates the accuracy of the FLUENT is acceptable considering the complex flow field, e.g. local wave breaking. For a supplement of the experimental studies, the pressure distributions around the hull and the hydrofoil and the wave pattern around the hull are detailed examined. Based on the experimental data and computational results, a semi (why semi)-empirical formula of hydrodynamic coefficients of this kind of craft is developed. In this formula, the interaction between the hydrofoil and the hull surface is considered. Comparison with numerical results shows that this formula can give a reasonable estimation of resistance and may be used for conceptual design of the GHC when the better results are not known.

Finally, preliminary studies of unsteady behaviour of GHC are carried out. Three cases representing ship berthing, leaving the harbor and turning around during navigation, are considered. The results reveal a significant difference between the unsteady results and the steady results, in some state the hydrodynamic force may follows the motion of the GHC which is in contrary with the outcome of the steady studies. This implies that the unsteady effects, such as the hydrodynamic force related to the acceleration of the GHC, are very important and calls for a detailed investigation on the unsteady procedure of the GHC.

10.2 Suggestions for further work

Detailed studies of the hydrodynamic feature of the GHC at steady state and a preliminary study of that in unsteady flow have been presented in this thesis. Further work may be required as discussed in this section.

(1) The CFD commercial software used in the numerical investigation is very time-consuming and requires great knowledge of computational fluid dynamics. The time consumed by each single case may be a week or longer in a single processor computer. This makes it practically impossible to be used during design state which may require an investigation of hundreds cases. To improve the accuracy, new robust numerical methods may be necessary. One solution might

be a combination of different numerical approach. For example, near the hull, a VOF based method is applied but in the area far from the hull a potential theory may be applied.

(2) GHC is a kind of high-speed craft. Due to their high speed, the motion of GHC is complex. However, in the numerical investigation an Eulerian method is currently applied. Under Eulerian view, the computational grid is fixed. This disables the users to consider the motion of the hulls and the free surface together. Model tests or empirical formulas are needed to obtain the running attitude of the GHC before calculation. As demonstrated in the experiments, the running attitude (trim, heel and heave) is always changing with the speed changes. In future numerical simulations, the motion of the hull should be considered. For example, the hydrodynamic performance and running attitude of the GHC are numerically by a new CFD method. The numerical method is based on Reynolds-Averaged Navier-Stokes (RANS) equations. The volume of fluid (VOF) method and the six-degrees-of-freedom equation are applied. An effective process is introduced to solve the numerical divergence problem in numerical simulation.

(3) In the numerical investigation, the side walls in the numerical simulation are considered as a fixed wall, from which wave reflection occurs. In order to preciously approximate the reality that the GHC travelling in open sea, further numerical investigations on a tank where the effects from the side wall can be ignored.

(4) The preliminary studies on unsteady procedure related to GHC demonstrate the importance and the necessity of using unsteady simulations. Further work on numerical investigation will be done.

(5) In the numerical investigation, all the cases considered were in calm water. The seakeeping of GHC is quite significant so that the effect of wave on the hydrodynamic performance should be taken into account in future work.

(6) The uncertainty in the analysis for existing numerical methods and the model tests cannot be ignored. A quantitative assessment of the effect of the relevant elements of the numerical calculation on the accuracy of the results, may promote the practical development of both CFD and model tests.

REFERENCE

Abramson N., 1974, Structural dynamics of advanced marine vehicles, *International Symposium: Dynamics of Marine Vehicles and Structures in Waves*, University College London, 344-357.

Ahamad R. K., Hassan G., 2010, A numerical modeling of hydrodynamic characteristics of various planing hull forms, *Ocean Eng.,* 37: 498-510.

AIAA, 1999, Assessment of experimental uncertainty with application to wind tunnel testing (S-071A-1999), *AIAA Standard Series*.

AIAA, 2003, AIAA Guide to assessing experimental uncertainty-supplement to S-071A-1999 (G-04502003e) , *AIAA Standard Series*.

Akkerman I., Dunaway J., Kvandal J., 2012, Toward free-surface modeling of planing vessels: simulation of the Fridsma hull using ALE-VMS, *Comput. Mech.,* 50: 719-727.

ASME, 1998, Test Uncertainty, *ASME Standard PTC 19.1-1998*.

Atsavapranee P., Forlini T., Furey D., Hamilton J., Percival S., Sung C.H., 2004, Experimental measurement for CFD validation of the flow about a submarine(ONR-Body 1), *Proc, 25th Symposium on Naval Hydrodynamics*, St. John's, Newfoundland & Labrador, Canada.

Azcueta R, 2003a, Steady and unsteady RANSE simulations for planing crafts, *7th Conference on Fast Sea Transportation, FAST'03*, Abano Terme, Italy.

Azcueta R., Caponnetto M., Soding H., 2003, Motion simulations for planing boats in waves, *Ship Technol. Res.,* 4: 182-198.

Bai K. J., Han J. H., 1994, A localized finite-element method for the nonlinear steady waves due to a two-dimensional hydrofoil, *J. Ship Res.,* 38: 42-51.

Baik S., Vlachogiannis M., Hanratty T. J., 2005, Use of particle image velocimetry to study heterogeneous drag reduction, *Exp. Fluids,* 39: 637–650.

Bandyopadhyay P. R., Henoch C., Hrubes J. D., Semenov B. N., Amirov A. I., Kulik V. M., Malyuga A. G., Choi K. S., Escudier M. P., 2005, Experiments on the effects of aging on compliant coating drag reduction, *Phys. Fluids,* 17: 085104.

Battistin D., Iafrati, A., 2003, A numerical model for hydrodynamic of planing surfaces, *Proc.7th Int. Conf. Fast Sea ransportation FAST2003*, Nanjing, 33-38.

Berendt A., Podliski J., Mizeraczyk J., 2010, DBD actuators with saw-like electrode, *Proc. of the European Drag Reduction and Flow Control Meeting,* Kiev, Ukraine, 9-10.

Besch P. K., Liu Y. N., 1972, Bending flutter and torsional flutter of flexible hydrofoil structs, *Proceeding of the 9th Symposium on Naval Hydrodynamics*, 1: 343-400.

Bouvy A., Henn R., Hensse J., 2009, Acoustic wave height measurements in a towing facility, *Proc. of the 1st International Conference on Advanced Model Measurement Technology for the EU Maritime Industry,* Turkey, 310-324.

Breslin J. P., 2000, Chines-dry planing of slender hulls: A general theory applied to prismatic surfaces, *J. Ship Res.,* 45: 59-72.

Brown D. K., Catchpole J. P., Chem M. I., Shand A. M. J., 1984, An evaluation of the hydrofoil HMS speedy, *Trans. R. Inst. Naval Archit.*, 126: 1-16.

Cai W. H., Li F. C., Zhang H. N., Li X. B., Yu B., Wei J. J., Kawaguchi Y., Hishida K., 2009, Study on the characteristics of turbulent drag-reducing channel flow by particle image velocimetry combining with proper Orthogonal decomposition analysis, *Phys. Fluids,* 21:

115103.

Çalişal S. M., Şireli M. E., Tan J., 2009, A direct measurement of wave resistance by the measurement of wave height on a surface patch, *J. Ship Res.*, 53: 170–177.

Cao H., 2008, The computation and research on resistance of planing craft based on the software FLUENT, *Master Thesis*, Harbin Engineering University, Harbin, 44-53.

Caponnetto M., 2001, Practical CFD simulations for planing hulls, *Proc. of 2nd International Euro Conference on High Performance Marine Vehicles*, Hamburg, 128-138.

Janson C.-E., 1996, Numerical computation of the flow around surface-piercing wings and hydofoils close to a free-surface, *The 11th International Workshop on Water Waves and Floating Bodies*, Hamburg, German, Paper No.15.

Cea L., Puertas J., Pena L., 2007, Velocity measurements on highly turbulent free surface flow using ADV, *Exp. Fluids*, 42: 333–348.

Ceccio S. L., Perlin M., Elbing, B. R., 2010a, A cost-benefit analysis for air layer drag reduction, *Proc. of the International Conference on Ship Drag Reduction,* Istanbul, Turkey, Paper No. 4.

Ceccio S. L., 2010b, Friction Drag reduction of external flows with bubble and gas injection, *Annu. Rev. Fluid Mech.,* 42: 183-203.

Chen C.K., Liu H., 2005. A submerged vortex lattice method for calculation of the flow around three-dimensional hydrofoil, *J. Ship Mech.,* 9: 41-45.

Chen J. H. Chang C. C., 2006, A moving PIV system for ship model test in a towing tank, *Ocean Eng.,* 33: 2025–2046.

Chen S. L., Ma Q. W., Yang S. L., 2008, Preliminary study on hydrodynamics of gliding hydrofoil craft, *Advanced Maritime Engineering Conference*, Chiba, Japan, 639-644.

Chen S.L., Ma Q.W., Yang S.L., 2011, An experimental study on hydrodynamic characteristics of gliding-hydrofoil craft, *J. Mar. Sci. Technol.,* 19: 89-96.

Chen S.L., Ma Q.W., Yang, S.L., 2010, Numerical investigation on hydrodynamic characteristics of a planing Hull, *Proc. of ISOPE 2010,* 3: 710-714.

Chen Z. M., 2012, A vortex based panel method for potential flow simulation around a hydrofoil, *J. Fluids Struct.*, 28: 378-391.

Chung M. H., 2008, Numerical study of rowing hydrofoil performance at low Reynolds numbers, *J. Fluids Struct.*, 24: 313-335.

Clement E. P., Blount D. L., 1963, Resistance tests of systematic series of planing hull forms, *SNAME Trans.,* 71: 491-579.

Cobelli P. J., Maurel A., Pagneux V., Petitjeans. P., 2009, Global measurement of water waves by Fourier transform profilometry, *Exp. Fluids,* 46: 1037-1047.

Cointe R., 1989, Two-dimensional water-solid impact. *6th International Offshore Mechanics and Arctic Engineering Symposium*, 111: 109-114.

Cointe R., 1991, Free-surface flows close to a surface-piercing body. *Mathematical Approaches in Hydrodynamics*, Society for Industrial and Applied Mathematics, 319-334.

Coleman H.W., Steele W. G., 1999, *Experimentation and uncertainty analysis for engineers*, John Wiley & Sons, New York.

Cowen E.A., Chang K.A. Liao Q., 2001, A single-camera coupled PTV-LIF technique, *Exp. Fluids,* 31: 63-73.

Daniello R. J., Waterhouse N. E., Rothstein J. P., 2009, Drag reduction in turbulent flows over super hydrophobic surfaces, *Phys. Fluids,* 21: 085103.

de Jong J., Cao L., Woodward S. H., Salazar J. P. L. C., Collins L. R., Meng H., 2009, Dissipation rate estimation from PIV in zero-mean isotropic turbulence, *Exp. Fluids,* 46: 517-526.

Deutsch S., Fontaine A. A., Moeny M. J., Petrie H. L., 2006, Combined polymer and microbubble drag reduction on a large flat plate, *J. Fluid Mech.,* 556: 309-327.

Drazen A., Fullerton A., Fu T., Beale K., Shea T., Brucker K., Dommermuth D., Wyatt D., Bhusha S., Carrica P., Stern F., 2010, A comparison of model-scale experimental measurements and computational predictions for a large transom-stern wave, *Proc. 28th Symposium on Naval Hydrodynamics*, Pasadena, USA.

Faltinsen O. M., 2005, *Hydrodynamics of High-Speed Marine Vehicles*, Cambridge University Press, New York.

Ferrante A., Elghobashi S., 2005, Reynolds number effect on drag reduction in a microbubble-Laden spatially developing turbulent boundary layer, *J. Fluid Mech.,* 543: 93–106 .

Foeth E. J., van Doorne C.W.H., van Terwisga T., Wieneke B., 2006, Time resolved PIV and flow visualization of 3D sheet cavitation, *Exp. Fluids,* 40: 503–513.

Fontaine E., Tulin MP., 1998, On the prediction of nonlinear free surface flows past slender hulls using 2D+T theory: the evolution of an idea, *RTO AVT symposium on fluid dynamic problems of vehicles operating near or in the air-sea interface*, Amsterdam, Netherlands.

Forbes L. K., 1985, A numerical method for non-linear flow about a submerged hydrofoil, *J. Eng. Math.*, 19: 329–339.

Forliti D. J., Strykowski P. J., Debatin K., 2000, Bias and precision errors of digital particle image velocimetry, *Exp. Fluid*, 28: 436-447.

Fréchou D., Mèès L, Lebrun D., Friedhoff B., Lammers G., Bugalski T., Di Felice F., Romano G., Verhulst M., Hallander J., Muthanna C., Ireland N., Borleteau J. P., Ollivier M., Delfos R., 2009, PIV operation in hydrodynamic facilities, P*roc. of the 1st International Conference on Advanced Model Measurement Technology for the EU Maritime Industry*, Turkey, 295-309.

Fu T.C., Fullerton A.M., Terrill E., Lada G., 2006, Measurements of the wave field around the R/V athena I, *Proc. 26th Symposium on Naval Hydrodynamic*s, Rome, Italy.

Fu T. C., Fullerton, A. M., 2009, Tow tank measurements of 3-D eave gields, *Proc. of the 1st International Conference on Advanced Model Measurement Technology for the EU Maritime Industry,* Turkey, 325-339.

Furuya O., 1975, Three-dimensional theory on supercavitating hydrofoils near a free surface, *J. Fluid Mech.*, 71: 339-359.

Giesing J. P., Smith A. M. O., 1967, Potential flow about two-dimensional hydrofoils, *J. Fluid Mech.*, 28: 113–129.

Gui L., Longo J., Metcalf B., Shao J. H., Stern F., 2001, Forces, moment and wave pattern for surface combatant in regular head waves Part I. Measurement systems and uncertainty assessment, *Exp. Fluids,* 31: 674-680.

Hassan G., Su Y. M., 2008a, Determining the hydrodynamic forces on a planing hull in steady motion, *J. Mar. Sci. Appl.*, 7:147-156.

Hassan G., Mahmoud G., 2008b, A combined method for the hydrodynamic characteristics of planing crafts, *Ocean Eng.*, 35: 310-322.

Hassan G., 2009, Hydrodynamics characteristics of the surface-piercing propellers for the planing craft, *J. Marine Sci. Appl.*, 8: 267-274.

Hajime K., 2006, A computing method for the flow analysis around a prismatic planing-hull, *7th international conference on high performance marine vehicles*, Yokosuka, Australian, 262-272.

Henry C. J., Dugundji J., Ashley H., 1959, Aeroelastic stability of lifting surface in high-density fluids, *J. Ship Res.*, 2: 10-21.

Herai N., Ishii T., Ando H., Kakuta R., 2010, A study on service performance analysis of energy saving appendage, *Conference Proceedings, the Japan Society of Naval Architects and Ocean Engineers,* 10: 419-422.

Hinatsu M., Kodama Y., Hori T., Kawashima H., Takeshi H., Makino M., Ohnawa M., Sanada Y., Murai Y., Ohta S., 2008, A full-scale air lubrication experiment using a large cement carrier for energy saving, *Conference Proceedings, the Japan Society of Naval Architects and Ocean Engineers*, 6: 161-162.

Hough G.R., Moran S.P., 1969, Froude number effects on two-dimensional hydrofoils, *J. Ship Res.*, 13: 53–60.

Hoyer K., Holzner M., Luthi B., Guala M., Liberzon A., Kinzelbach W., 2005, 3D scanning particle tracking velocimetry, *Exp. Fluids*, 39: 923–934.

Hui S., Faltinsen O. M., 2007, The influence of gravity on the performance of planing vessels in calm water, *J. Eng. Math.*, 58: 91–107.

Hui S., Faltinsen O. M., 2010, Numerical study of planing vessels in waves, *9th International Conference on Hydrodynamics*, Shanghai, 451-458.

Hui S., Faltisen O. M., 2011, Dynamic motions of planing vessels in head seas, *J. Mar. Sci. Technol.*, 16: 168-180.

Imamura H., Saito Y., Asao M., 1990, Automatic control system for jetfoil, *Kawasaki Tech. Rev.*, 107: 1-9.

Inukai Y., Horiuchi K., Kinoshita T., Kanou H., Itakura H., 2001, Development of a single-handed hydrofoil sailing catamaran, *J. Mar. Sci. Technol.*, 6: 31-41.

Jin W., 2009, The analysis and valuation of turbulence models used in naval architecture and ocean engineering, *Master Thesis,* School of Naval Architecture, Ocean and Civil Engineering, Shanghai Jiao Tong University, China.

Joslin R.D., Thomas R.H., Choudhari M.M., 2005, Synergism of flow and noise control technologies, *Prog. Aerosp. Sci.,* 41: 363-417.

Jovanovic J., Pashtrapanska M., Frohnapfel B., Durst F., Koskinen J., Koskinen K., 2006, On the mechanism responsible for turbulent drag reduction by dilute addition of high polymers: theory, experiments, simulations, and predictions, *ASME J. Fluids Eng.,* 128: 118-130.

Kalezayev B. A., 1985, *The manual for hydrofoil craft and hover craft design,* National Defense Industry Press.

Kano T., Takano S., Matsuura K., Kobayashi M., 2010, On the measured wave spectra by coastal vessels and estimated added resistance in wave based on the wave spectra, *Conference Proceedings, the Japan Society of Naval Architects and Ocean Engineers,* 11: 375-378.

Kawakita, C., 2010, Prediction accuracy of full scale wake distribution required by propeller design, *Conference Proceedings, the Japan Society of Naval Architects and Ocean Engineers,* 10: 423-424.

Kawanami Y., Hinatsu M., 2010, Bubble flow visualization around a domestic cement carrier equipped with air lubrication system, *Conference Proceedings, the Japan Society of Naval Architects and Ocean Engineers,*10: 449-450.

Kennell C., Plotkin A., 1984, A second order theory for the potential flow about thin hydrofoils, *J. Ship Res.*, 28: 55–64.

Kerwin J.E., Kinnas, S.A., Lee J.T., Shih W.Z., 1987, A surface panel method for the hydrodynamic analysis of ducted propellers, *SNAME Trans.* 95: 93–122.

Kim D. J., Vorus W., Troesch A., Gollwitzer R., 1997, Coupled hydrodynamic impact and elastic response, *21st Symposium on Naval Hydrodnamics,* Trondheim, Norway.

Kim S. H., Yamato H., 2004a, An experimental study of the longitudinal motion control of a fully submerged hydrofoil model in following seas, *Ocean Eng.*, 31: 523-537 .

Kim S.H., Yamato H., 2004b, On the design of a longitudinal motion control system of a fully-submerged hydrofoil craft based on the optimal preview servo system, *Ocean Eng.*, 31: 1637-1653.

Kim S.H., Yamato H., 2005, The estimation of wave elevation and wave disturbance caused by the wave orbital motion of a fully submerged hydrofoil craft, *Mar. Sci. Technol.*, 10: 22-31.

Kim Y. G., Lee C. S., Suh J. C., 1994, Surface panel method for prediction of flow around a 3-d steady or unsteady cavitation hydrofoil, *2nd international Symposium on Cavitation*, Tokyo, 113-120.

Kinnas S., Fine N., 1993, A numerical nonlinear analysis of the flow around two- and three-dimensional partially cavitation hydrofoils, *J. Fluid Mech.*, 254: 151-181.

Kitagawa A., Hishida K., Kodama Y., 2005, Flow structure of microbubble-laden turbulent channel flow measured by PIV combined with the shadow image technique, *Exp. Flui*ds, 38: 466-475.

Kochevsky A. N., 2004, Computation of internal fluid flows in channels using the CFD software tool flow vision, *Bull. Sumy State Uni.,* 61: 25-36.

Kodama Y., Takahashi T., Makino M., Ueda T., 2004a, Conditions for microbubbles as a practical drag reduction device for ships, *Proc. 5th International Conference on Multiphase Flow*, Yokohama, Japan, Paper No. 535.

Kodama Y., Takahashi T., Hori T., Makino M., Ueda T., 2004b, Characteristics of microbubble drag reduction on a 50m long flat plate, *Proc. 3rd International Symposium on Two-Phase Flow Modelling and Experimentation,* Pisa, Italy.

Kodama Y., Murai Y., Kawamura T., Sugiyama K., Yamamoto F., 2006, Direct comparison of experimental and numerical simulation on microbubble flows for skin friction reduction, *Proc. 26th Symposium on Naval Hydrodynamics,* Rome, Italy.

Kodama Y., Hinatsu M., Hori T., Kawashima H., Takeshi H., Makino M., Ohnawa M., Sanada Y., Murai Y., Ohta S., 2008, A full-scale air lubrication experiment using a large cement carrier for energy saving: result and analysis, *Conference Proceedings, the Japan Society of Naval Architects and Ocean Engineers,* 6: 163-166.

Kouh J.S., Lin T.J., Chau S.W., 2002, Performance analysis of two dimensional hydrofoil under free surface, *J. Natl. Taiwan Uni.*, 86: 113-123.

Kulik V. M., Boiko A. V., Chun H. H., Lee I., 2010, Verification of drag reduction capabilities of stiff compliant coatings in air at moderate speeds, *Proc. of the 15th European Drag Reduction and Flow Control Meeting*, Kiev, Ukraine, 45-46.

Kunz R.F., Gibeling H.J., Maxey M.R., Tryggvason G., Fontaine A.A., Petrie H.L., Ceccio S.L., 2007, Validation of two-fluid Eulerian CFD modeling for microbubble drag reduction across a wide range of reynolds numbers, *J. Fluids Eng.,* 129: 66-79.

Lai C., Troesch A. W., 1995, Modeling issues related to the Hydrodynamics of three dimensional steady planing, *J. Ship Res.,* 39: 1-24.

Lai C., Troesch A. W., 1996, A vortex lattice method of high speed planing, *Int. J. Numer. Method Fluids*, 22: 495-513.

Lang N., Limberg, W., 1999, Construction of three-dimensional flow structure out of two-dimensional steady flow field velocity measurement, *Exp. Fluids,* 27: 351-358.

Larsson L., Janson C.E., 1999, Potential flow calculations for sailing Yachts, *CFD for Ship and Offshore Design, 31st WEGMENT School*, Hamburg.

Lee C. S., Kim Y. G., Lee J. T., 1992, A potential-based panel method for the analysis of a two-dimensional super- or partially-cavitating hydrofoil, *J. Ship Res.,* 36:168-181.

Lee S.J., Joo Y.R., 1996, Calculation of wave making resistance of high speed catamaran using a panel method, *Proc. of 3rd Korea-Japan Joint Workshop on Ship and Marine Hydrodynamics,* Taejon, Korea, 117-124.

Lee S.J., Paik B.G., Lee C.M., 2005, Phase-averaged particle tracking velocimetry measurements of propeller wake, *J. Ship Res.,* 49: 43–54.

Lee J. Y., Paik B.G., Lee S. J., 2009, PIV measurements of hull wake behind a container ship model with varying loading condition, *Ocean Eng.,* 36: 377-385.

Lee I., Choi K. S., Chun H. H., 2010, Drag reduction capabilities and mechanism of outer-layer vertical blades array, P*roc. of the European Drag Reduction and Flow Control Meeting,* Kiev, Ukraine, 47-48.

Lewis S. G., Hudson D. A., Turnock S. R., Blake J. I. R., Shenoi R. A., 2006, Predicting motions of high speed RIBs: a comparison of non-linear strip theory with experiments, *Proceedings of the 5th International Conference on High Performance Marine Vehicles*, Launceston, Australia, 210-224.

Li D. Q, Grekula M., Lindell P., 2010, Towards numerical prediction of unsteady sheet cavitation on hydrofoils, *J. Hydrodyn.,* 22: 741-746.

Li Z. R., Pourquie M., Tom J.C., Terwisga V., 2010, A numerical study of steady and unsteady cavitation of a 2d hydrofoil, *J. Hydrodyn.,* 22: 770-777.

Liu D. C., Hong F. W., Lu F., 2010, The numerical and experimental research on unsteady cloud cavitating flow of 3D elliptical hydrofoil, *J. Hydrodyn.,* 22: 759-763.

Ma S., 2005, 2.5D computational method for ship motions and wave loads of high speed ships, *PhD thesis*, Harbin Engineering University, Harbin, 16-62.

Makino M., Kodama Y., Hori T., Hinatsu M., Kawashima H., Goto H., Tsukada K., 2008, Effect of surface curvature on skin friction reduction by air bubbles, *Conference Proceedings, the Japan Society of Naval Architects and Ocean Engineers,* 6: 157-160.

Md. M. K., Mohammad S. A., 2012, Numerical study of periodic cavitating flow around NACA0012 hydrofoil, *Ocean Eng.,* 55: 81-87.

Meng J., 2005, Sea water drag reduction & world peace, *Presentation at the 2nd International Symposium on Seawater Drag Reduction,* Busan, Korea.

Millward A., Brown G. L., 2005, The capacitance method of measuring the wetted surface area of a ship model, *Int. Shipbuilding Prog.,* 52: 231-244.

Minoura M., Naito, S., Matsuda, K., 2008a, Statistical prediction of ship speed loss using onboard measurement data, *Conference Proceedings, the Japan Society of Naval Architects and Ocean Engineers,* 6: 5-8.

Minoura M., 2008b, Performance estimation by independent component analysis of onboard measurement data, *Conference Proceedings, the Japan Society of Naval Architects and Ocean Engineers,* 7: 27-30.

Moore K.J., Moore C.M, Stern M.A., Deutsch S., 2006, Design and test of a polymer drag reduction system on sea flyer, *Proc. 26th Symposium on Naval Hydrodynamics,* Rome, Italy.

Murai Y., Fukuda H., Shi Y., Kodama Y., Yamamoto F., 2007, Skin friction reduction by large air bubbles in a horizontal channel flow, *Int. J. Multiphase Flow,* 33: 147-163.

Murakami A., Kawamura T., Hinatsu M., 2008, Numerical simulation of flow around a full scale ship equipped with bubble generators, *Conference Proceedings, the Japan Society of Naval Architects and Ocean Engineers,* 6: 153-156.

Nakatake K., Ando, J., Kormura A., Kataoka K., 1990, On the flow field and the hydrodynamic forces of an obliquing ship (in Japanese), *Transactions of the West-Japan Society of Naval Architects*, No. 80: 1-12.

Nishiyama T., 1970, Lifting line theory of supercavitating hydrofoil of finite span, *J. Appl. Math. Mech.*, 50: 645-653.

Nguyen C. V., Nguyen T. D., Wells J. C., Nakayama A., 2010, Interfacial PIV to resolve flows in the vicinity of curved surfaces, *Exp. Fluids,* 48: 577-587.

Office of Naval Research, Naval Surface Warfare Center, Carderock Division, Naval Studies Board, National Research Council, 1999, *22nd Symposium on Naval Hydrodynamics*, National Academies Press, Washington, D.C..

Olivieri A., Pistani F., Di Mascio A., 2003, Breaking wave at the bow of a fast displacement ship model, *J. Mar. Sci. Technol.,* 8: 68-75.

Osher S., Sethian J. A., 1988, Fronts propagating with curvature-dependent speed: Algorithms based on Hamilton-Jacobi formulations, *J. Comput. Phys.,* 79: 12–49.

Petrovic D.V., Vukoslavcevic P.V., Wallace J.M., 2003, The accuracy of turbulent velocity component measurements by multi-sensor hot-wire probes: a new approach to an old problem, *Exp. Fluids,* 34: 130-139.

Plotkin A., 1975, Thin-hydrofoil thickness problem including leading-edge corrections, *J. Ship Res.,* 19: 122–129.

Qiu W., Yang Q. Y., Peng H., 2008, Slamming force on a planing hull: Comparison between 3D and 2D solutions, *Proceedings of the 18th International Offshore and Polar Engineering Conference*, Vancouver, Canada.

Reis M. L. C. C., Mello O. A. F., Uyeno S., 2003, Calibration uncertainty of an external six-component wind tunnel balance, *AIAA 2003-3884*.

Royce R.A., Vorus W.S., 1998, Pressure measurement on a planing craft and comparisons with calculation, *25th ATTC,* Iwoa City, IA.

Royce R. A., 2001, 2-D theory extended to planing craft with experimental comparison, *PhD Thesis*, Department of Naval Architecture and Marine Engineering, The University of Michigan.

Run X., Song X., Yamamoto F., 2001, Direct measurement of the vorticity field in digital particle images, *Exp. Fluids,* 30: 696-704.

Ryu Y., Chang K.A., Lim H.J., 2005, Use of bubble image velocimetry for measurement of plunging wave impinging on structure and associated greenwater, *Meas. Sci. Technol.,* 16: 1945–1953.

Saito Y., Ikebuchi T., 1990, Fully submerged hydrofoil craft: prediction of sea keeping qualities of high-speed craft, *Proc. of the 7th Marine Dynamics Symposium*, 107-141.

Saito Y., Kuroi A., 1989, Active control system of hydrofoils. Control of Marine Vehicles, *Proc. of the 6th Marine Dynamics Symposium*, 75-94.

Sakir B., 1999, A potential based panel method for 2-D hydrofoils, *Ocean Eng.,* 26: 343-361.

Salvasen N., 1969, On higher-order wave theory for submerged two-dimensional bodies, *J. Fluid Mech.*, 38: 415-432.

Savitsky D., 1964, Hydrodynamic design of planing hulls, *J. Mar. Technol.*, 1: 71-95.

Sanada Y., Nagaya S., 2010a, Recent rrogress of image measurement techniques in marine hydrodynamics, *JSPC Symposium on Present Status and Perspective of Tank Testing Technique, Japan Society of Naval Architects and Ocean Engineers,* Kobe, Japan, 95–123.

Sanada Y., Takayama A., Hara E., Toda Y., 2010b, Development of 3-D iterative reconstruction technique for RLD method, *Conference Proceedings, the Japan Society of Naval Architects and Ocean Engineers,*10: 459-462.

Sanders W.C., Winkel E.S., Dowling D. R., Perlin M., Ceccio S. L., 2006, Bubble friction drag reduction in a high-Reynolds number flat-plate turbulent boundary layer, *J. Fluid Mech.,* 552: 353-380.

Sasaki N., Matsubara T., Yoshida, T., 2008, Analysis of speed drop of large container ships operating in sea way, *Conference Proceedings, the Japan Society of Naval Architects and Ocean Engineers,* 6: 9-12.

Savander B. R., 1997, Planing hull steady hydrodynamics, *PhD Thesis*, Department of Naval Architecture and Marine Engineering, The University of Michigan.

Savitsky D., DeLorme M. F., Raju D., 2007, Inclusion of whisker spray resistance in performance prediction method for high-speed planing hulls, *J. Mar. Technol.*, 44: 35-56.

Shen J. H., Zhang C. B., Chai Y. Y., Zou J., 2011, Prediction of planing craft motion based on grey system theory, *J. Mar. Sci. Appl.*, 10: 240-245.

Shen X.C., Ceccio S.L., Perlin M., 2006, Influence of bubble size on micro-bubble drag reduction, *Exp. Fluids,* 41: 415-424.

Shoji R., Adachi H., Ohtsu K., 2008, Development of analysis technique for ship performance in actual seas using abstract logbook, *Conference Proceedings, the Japan Society of Naval Architects and Ocean Engineers,* 7: 21-22.

Somandepalli V. S. R., Hou Y. X., Mungal M. G., 2010, Concentration flux measurements in a polymer drag-reduced turbulent boundary layer, *J. Fluid Mech.,* 644: 281-319.

Song Y.Y., Kim M.C., Chun H. H., 2007, A study on resistance test of icebreaker with synthetic ice, *J. Soc. Nav. Arch. Korea,* 44: 389-397.

Starke A.R., Windt J., Raven H.C., 2006, Validation of viscous flow and wake Field predictions for ships at full scale, *Proc. 26th Symposium on Naval Hydrodynamics,* Rome, Italy, 17-22.

Su B., Li M., Lu Q., 2009, Toward understanding whether super hydrophobic surfaces can really decrease fluidic friction drag, *Langmuir*, 26, 6048-6052.

Su Y. M., Chen Q. T., Shen H. L., Lu W., 2012, Numerical simulation of a planing vessel at high speed, *J. Mar. Sci. Appl.*, 11:178-183.

Sur T.W., Chevalier K., 2004, Field measurement of bow spray droplets, *Proc. 25th Symposium* *on Naval Hydrodynamics,* St. John's, Newfoundland and Labrador, Canada.

Sverchkov A. V., 2010, Application of air cavities on high speed ships in Russia, *Proc. of the International Conference on Ship Drag Reduction*, Istanbul, Turkey, Paper No. 11.

Takano S., Kawakita C., Kodan Y., Mizokami S., Higasa S., 2010, Development of air lubrication system and verification by the full scale ship test, *Conference Proceedings, the Japan Society of Naval Architects and Ocean Engineers,* 11: 443-446.

Takano S., Kawakita C., Kodan Y., Mizokami S., 2010, Experimental verification of the behavior of injected air on the ship bottom and its influence on propeller, *Conference Proceedings, the Japan Society of Naval Architects and Ocean Engineers,* 10: 455-458.

Takayama A., Sanada Y., Toda Y., Hamachi S., 2008, On ship generated waves measured by the reflected light image : development of a new algorithm of tracking for color information, *Conference Proceedings, the Japan Society of Naval Architects and Ocean Engineers,* 7: 103-104.

Tanimoto K., Sanada Y., Toda Y., 2010, A study of error factor in wave field measurement using RLD method, *Conference Proceedings, the Japan Society of Naval Architects and Ocean Engineers,*11: 455-458.

Taylor L. K., Arabshahi A., Whitield D. L., 1995, Unsteady three-dimensional incompressible Navier-Stokes computations for a 6:1 prolate spheroid undergoing time-dependent maneuvers, *AIAA,* paper no. 95-0313.

Terrill E.J., Taylor G.L., 2007, Measuring waves at sea for the validation of wave generation and seakeeping Codes, *Proc. 9th International Conference on Numerical Ship Hydrodynamics,* Ann Arbor, Michigan, USA.

Th. Von Karman, 1929, The impact of seaplane floats during landing, *NACA TN 321*, Washington, D.C., USA.

Thill C., 2010, A long road mapping drag reduction, *Proc. of the International Conference on Ship Drag Reduction*, Istanbul, Turkey, Paper No.1.

Troy C.D., Koseff J.R., 2005, The generation and quantitative visualization of breaking internal waves, *Exp. Fluids,* 38: 549–562.

Tulin M. P., 1957, The theory of slender surfaces planing at high speeds, *Schiffstechnik* ,21: 125-133.

Uhlman J., 1978, A partially cavitated hydrofoil of finite span, *J. Fluids Eng.,* 100: 353-354.

Van Houten R., 1982, The numerical prediction of unsteady sheet cavitation on high aspect ratio hydrofoils, *14th Symposium on Naval Hydrodynamics,* Ann Arbor.

Vorus W. S., 1996, A flat cylinder theory for vessel impact and steady planing resistance, *J. Ship Res.,* 40: 89-106.

Vorus W. S., Royce R. A., 2000, Shock reduction of planing boats, *Ship Structure Symposium 2000*, Washington D. C., USA.

Wang R. j., Zhang K., Wang G., 2007, *Fluent Techniques and Application*, Tsinghua University Press, Beijing.

Wang Z. L., Niu J. L.，Qin Z. B., Pang Y. J., 2009, The computation resistance of planing craft based on the CFD techniques, *14th Conference on China Ocean Engineering*, Hohhot, 309-315.

Wangner H., 1932, Über stock-und gleitvorgänge an der oberfläche von flüssigkeiten, *ZAMM12,* 193-215.

Weist W. R., Mitchell W. I., 1976, The automatic control system for the Boeing commercial JETFOIL, *IEEE National Aerospace and Electronics Conference,* Dayton, Ohio, 366-375.

Whally R., Choi, K. S., 2010, Changes in turbulent boundary layer structures by spanwise travelling waves created by DBD plasma actuators, *Proc. of the European Drag Reduction and Flow Control Meeting*, Kiev, Ukraine, 77-79.

Xie N., Vassalos D., 2007, Performance analysis of 3D hydrofoil under free surface, *Ocean Eng.,* 34: 1257-1264.

Xu L., Troesch A. M., Vorus W. S., 1998, Asymmetric vessel impact and planing hydrodynamics, *J. Ship Res.,* 42: 187-198.

Yamamoto N., Matsumoto T., Miyake R., Toyoda K., 2010, Analysis of full scale measurement data of large container ships on the effect of the hydroelastic response, *Conference Proceedings, the Japan Society of Naval Architects and Ocean Engineers,* 11: 135-136.

Yang J., Rhee S. H., Kim H., 2009, Propulsive performance of a tanker hull form in damaged conditions, *Ocean Eng.,* 36: 133-144.

Yang B., Shu X.W., 2012, Hydrofoil optimization and experimental validation in helical vertical axis turbine for power generation from marine current, *Ocean Eng.*, 42: 35-46.

Yang S. L., Chen S. L., 2008, Experiment and numerical study on gliding-hydrofoil craft rapidity, *Proc. of International Offshore and Polar Engineering Conference,* Vancouver, Canada, 375-380.

Yang S. L., Gao L., 2006, Resistance study on full-scale gliding-hydrofoil craft with V-shape planing bottom and TV-shape hydrofoil, *J. Jiangsu Uni. Sci. Technol.: Natural Science Edition*, 4: 16-23.

Yang S. L., Ma, Q. L., Chen S. L., Gao, L., Wu, A, 2008, Experimental research on resistance performance of gliding-hydrofoil craft with a T-formed hydrofoil and shallow V-shaped bottom, *Online Journal of International Conference on Computational & Experimental Engineering and Sciences*, 5: 7-14.

Yeung R.W., Bouger Y.C., 1979, A hybrid-integral equation method for steady two-dimensional ship waves, *J. Numer. Method Eng.*, 14: 317–336.

Zhang M., Shen G., Wei R., 2002, Error analysis of stereoscopic particle image velocimetry, *Optical Tech. and Image Processing for Fluids and Solids Diagnostics,* Beijing, China.

Zhao R., Faltinsen O., 1993, Water entry of two-dimensional bodies, *J. Fluid Mech.,* 246: 593-612.

Zhao R., Faltinsen O., 1996, Water entry of arbitrary two-dimensional sections with and without flow separation, *21st Symposium on Naval Hydrodynamics,* Trondheim, Norway.

Zhao R., Faltinsen O.M., Haslum H.A.,1997, A simplified nonlinear analysis of a high-speed planing craft in calm water, *Proceedings of 4th international conference on fast sea transportation,* Sydney, Australia, 431–438.

Zhou Z. Q., 2003, A theory and analysis of planing catamarans in calm and rough water, *PhD Thesis,* School of Naval Architecture and Marine Engineering, University of New Orleans, Louisiana, US.

Zou Z., Soding H., 1994, A panel method for lifting potential flows around three-dimensional surface-piercing bodies, *Proceedings of 20th Symposium on Naval Hydrodynamics*, Santa Barbara, CA.

APPENDIX A: PUBLICATION LIST

The following papers have been published, which are based on the research of this study.

[1] Chen, S.L., Ma, Q.W. and Yang, S.L., "An Experimental Study on Hydrodynamic Characteristics of Gliding-Hydrofoil Craft", *Journal of Marine Science and Technology (JMST)*, Vol.19, No.1, pp.89-96, 2011.

[2] Chen, S.L., Ma, Q.W. and Yang, S.L., 2010, "Numerical Investigation on Hydrodynamic Characteristics of a Planing Hull", *Proceedings of ISOPE 2010,* ISBN 978-1-880653-77-7, Vol.3, pp. 710-714.